

March 2020

Performance Enhancement Techniques for Next-Generation Multi-Service Communication and Medical Cyber-Physical Systems

Ali Fatih Demir
University of South Florida

Follow this and additional works at: <https://digitalcommons.usf.edu/etd>



Part of the [Electrical and Computer Engineering Commons](#)

Scholar Commons Citation

Demir, Ali Fatih, "Performance Enhancement Techniques for Next-Generation Multi-Service Communication and Medical Cyber-Physical Systems" (2020). *USF Tampa Graduate Theses and Dissertations*.

<https://digitalcommons.usf.edu/etd/8183>

This Dissertation is brought to you for free and open access by the USF Graduate Theses and Dissertations at Digital Commons @ University of South Florida. It has been accepted for inclusion in USF Tampa Graduate Theses and Dissertations by an authorized administrator of Digital Commons @ University of South Florida. For more information, please contact digitalcommons@usf.edu.

Performance Enhancement Techniques for Next-Generation
Multi-Service Communication and Medical Cyber-Physical Systems

by

Ali Fatih Demir

A dissertation submitted in partial fulfillment
of the requirements for the degree of
Doctor of Philosophy
Department of Electrical Engineering
College of Engineering
University of South Florida

Major Professor: Hüseyin Arslan, Ph.D.
Ismail Uysal, Ph.D.
Nasir Ghani, Ph.D.
Dmitry Goldgof, Ph.D.
Qammer H. Abbasi, Ph.D.

Date of Approval:
April 01, 2020

Keywords: 5G, brain-computer interfaces, channel modeling, interference management,
scheduling, waveform design, wireless body area network

Copyright © 2020, Ali Fatih Demir

Dedication

To my family

Acknowledgments

It was a long and challenging but rewarding journey. First and foremost, praises to Allah for giving me the blessing, chance, and endurance to complete this study.

Special thanks to my advisor, Dr. Hüseyin Arslan, for providing me the opportunity and the means to achieve this level, and having the patience to allow me to develop my skills. His guidance, encouragement, and also efforts in pushing my limits further made this dissertation possible. I am really grateful not only for his exceptional endeavor in cultivating my professional skills but also for his hospitality in Tampa and being a family for us while we are thousands of kilometers away from our home. It is an honor for me to be a student of him.

I would also like to thank Dr. Ercüment Arvas, Dr. Richard D. Gitlin, Dr. Ismail Uysal, Dr. Qammer Abbasi, Dr. Nasir Ghani, Dr. Dmitry Goldgof, and Dr. Selcuk Kose for their support and guidance throughout my graduate studies. Their broad experience enriched my background significantly, and invaluable encouragement has led to completion of this dissertation. Without a doubt, I am fortunate to meet and collaborate with them.

My sincere appreciation goes to every teacher and professor who spent their valuable time to teach me something new and inspired me to be a scientist. Their efforts throughout my life fructified and formed this dissertation.

It has been a great privilege to be a member of the Wireless Communications and Signal Processing (WCSP) group. I owe a lot to my colleagues and dear friends in this group. I would like to thank Dr. Ali Görçin, Dr. Sadia Ahmed, Dr. Alphan Sahin, Dr. Bahadir Celebi, Dr. Anas Tom, Dr. M. Harun Yilmaz, Dr. Ertugrul Güvenkaya, and Dr. Esat Ankarali. They carried out the research legacy from previous WCSP alumni and shed light on new members. Special thanks to my officemates, Dr. Mohammad Hafez and Berker Pekoz, for their valuable brotherhood and fruitful

discussions throughout my studies. I also would like to thank Murat Karabacak, Sinasi Cetinkaya, and Mert Sahin. I wish all of them the best in their future lives.

Warm greetings to all my friends, who shared the Ph.D. experience with me. I would like to thank Dr. Mustafa Ozmen, Dr. Koray Ozcan, Dr. Ahmad Gheethan, Dr. Mohamed H. Elkourdi, Dr. Asim Mazin, Dr. Adrian Jaesim, Dr. Emre Seyyal, Dr. Aras Uzun, Ismail Ulutürk, Merve Kacar, Mostafa Ibrahim, and Habib Kaya. I will be forever indebted to them for their motivation and invaluable support.

A desired respect and thanks for my parents, Dr. Ahmet Demir and Hülya Demir, for supporting me since the beginning and providing their best to raise me in an excellent environment. None of this would have been possible without their unconditional love and support throughout my life. I also would like to express my gratitude to my dear brother, Dr. Murat Emre Demir, for always feeling his back no matter wherever he is.

My deepest gratitude goes to my wife, Semra Demir, for all of her sacrifice, support, and patience during my study. I could have never completed this dissertation without her. I hope our dear sons, Ahmet Selim Demir and Hasan Alp Demir, always appreciate their mother and will achieve better accomplishments in their life.

Table of Contents

List of Tables	iii
List of Figures	vi
Abstract	vii
Chapter 1: Introduction	1
1.1 Foundations of Multi-Numerology OFDM Systems for 5G Mobile Network	1
1.1.1 Waveform Definition	3
1.1.2 Wireless Communications in the Presence of Multipath Channel	4
1.1.3 CP-OFDM and Multi-Numerology Systems	6
1.2 Foundations of <i>In Vivo</i> Channel Modeling for Wireless Body Area Networks	11
1.2.1 Human Body Models and Propagation Through Tissues	12
1.2.2 Frequency of Operation and Antenna Design Considerations . .	14
1.2.3 EM Wave Propagation Models for <i>In Vivo</i> Communications . . .	19
1.3 Foundations of SSVEP based Brain-computer Interfaces	22
1.3.1 Brain-computer Interfaces	22
1.3.2 Steady-state Visual Evoked Potentials	23
Chapter 2: Inter-numerology Interference Management with Adaptive Guards	27
2.1 Introduction	27
2.2 System Model	30
2.3 Optimization of the Adaptive Guards	34
2.4 Inter-numerology Interference (INI)-based Scheduling	39
2.5 Conclusions	42
Chapter 3: Anatomical Region-Specific <i>In Vivo</i> Channel Characterization	44
3.1 Introduction	44
3.2 Simulation and Measurement Settings	47
3.2.1 Simulation Setup	47
3.2.2 Experimental Setup	50
3.3 <i>In Vivo</i> Channel Characterization	52
3.3.1 Path Loss and Shadowing	52
3.3.2 Multipath Characteristics	57
3.4 Conclusions	62

Chapter 4: Bio-inspired Filter Banks for Frequency Recognition of SSVEP-based Brain-computer Interfaces	64
4.1 Introduction	64
4.2 Methods and Materials	67
4.2.1 Evaluation Metric	67
4.2.2 Datasets and Pre-processing	68
4.2.3 Proposed Method	69
4.2.4 Comparison Methods	74
4.2.4.1 UF	74
4.2.4.2 PSDA	74
4.2.4.3 CCA	75
4.3 Results and Discussion	76
4.4 Conclusions	79
Chapter 5: Concluding Remarks	81
References	82
Appendix A: Copyright Permissions	99
About the Author	End Page

List of Tables

Table 1.1: Frequency bands and bandwidths for the three different propagation methods in IEEE 802.15.6.	16
Table 1.2: A review of selected studied path loss models for various scenarios.	20
Table 2.1: Simulation parameters.	33
Table 2.2: Optimal guard duration (GD) and guard band (GB) pairs for selected θ	39
Table 2.3: Key parameters of randomly scheduled numerologies for adaptive guard allocation.	40
Table 2.4: Key parameters of INI-based scheduled numerologies for adaptive guard allocation.	40
Table 2.5: Spectral efficiency comparison for various guard allocation and scheduling strategies.	42
Table 3.1: Variance of shadowing term (S) in dB for each <i>in vivo</i> depth.	54
Table 3.2: Statistical PL model parameters for anatomical regions.	56
Table 3.3: Statistical PL model parameters for anatomical directions.	56
Table 3.4: Experimental PL values for selected <i>in vivo</i> locations.	57
Table 3.5: Comparison of the statistical PL model parameters.	57
Table 3.6: <i>In vivo</i> multipath propagation statistics at 915 MHz.	61
Table 4.1: Overview of the SSVEP datasets.	69
Table 4.2: Performance evaluation of SSVEP recognition algorithms on Dataset-A.	76
Table 4.3: Performance evaluation of SSVEP recognition algorithms on Dataset-B.	76
Table 4.4: Statistical analysis of ITR difference between BIFB and comparison methods by using paired t-test.	77
Table 4.5: SSVEP recognition accuracy performance for 28 Hz stimulus in Dataset-A.	77

List of Figures

Figure 1.1: The research domains and main concepts that are studied in the dissertation.	2
Figure 1.2: 5G use cases: (a) Enhanced mobile broadband, (b) ultra-reliable low-latency communications, and (c) massive machine type communications.	3
Figure 1.3: Wireless communications in the presence of a multipath propagation.	4
Figure 1.4: Time and frequency dispersive multipath channel.	5
Figure 1.5: Illustration of a CP-OFDM symbol formation at the transmitter.	7
Figure 1.6: CP-OFDM block diagram: (a) Transmitter, (b) receiver.	8
Figure 1.7: Multi-user OFDM spectrum: (a) Single numerology system, (b) multi-numerology system.	9
Figure 1.8: Heterogeneous human body models: (a) HFSS [®] model, (b) physical phantom [33].	13
Figure 1.9: Multi-layer human tissue model at 403 MHz (ϵ_r : Permittivity, σ : Conductivity, P_T : Power transmission factor).	15
Figure 1.10: EM propagation through tissue interface.	17
Figure 1.11: Selected <i>in vivo</i> antenna samples: a) A dual-band implantable antenna [49], b) A miniaturized implantable broadband stacked planar inverted-F antenna (PIFA) [50], c) A miniature scalp-implantable [30], d) A wideband spiral antenna for WCE [35], e) An implantable folded slot dipole antenna [51].	18
Figure 1.12: Functional model of an SSVEP-based BCI.	22
Figure 1.13: The number of articles on BCI research over years (The data is obtained from PubMed on March 21, 2020).	23
Figure 1.14: A comparison of various BCI modalities with respect to their training time and information transfer rate [69].	24
Figure 1.15: SSVEP response to frequency-coded stimuli at the occipital region of the brain.	25

Figure 2.1:	Transmitter windowing operation and guard duration allocation.	31
Figure 2.2:	Guard band allocation between two numerologies considering the allowed interference level (θ) in the adjacent band.	31
Figure 2.3:	(a) Asymmetric interference scenario in a mixed numerology network; (b) Block diagram of the multi-window operation.	33
Figure 2.4:	Frequency domain multiplexed numerologies.	34
Figure 2.5:	PSD of W-OFDM: (a) The effect of Δf (α is fixed to 0.03); (b) The effect of α (Δf is fixed to 15 kHz).	36
Figure 2.6:	Required GB and GD pairs to achieve selected θ levels for a W-OFDM signal with $\Delta f = 15 \text{ kHz}$	37
Figure 2.7:	Spectral efficiency (η) of the GB and GD pairs that achieves selected $\theta_{\Delta f=15 \text{ kHz}}$ (Please note that each α corresponds to a GB-GD pair).	38
Figure 2.8:	INI-based scheduled numerologies with various use cases.	41
Figure 3.1:	<i>In vivo</i> -WBAN devices for various applications.	45
Figure 3.2:	(a) Investigated anatomical regions; (b) <i>In vivo</i> and <i>ex vivo</i> antenna locations in simulations.	49
Figure 3.3:	Experiment setup for <i>the in vivo</i> channel: 1) Vector network analyzer (VNA), 2) human male cadaver, 3) coaxial cables, 4) a novel tapered slot CPW-fed antenna (<i>in vivo</i>), 5) insulated dipole antenna (<i>ex vivo</i>).	51
Figure 3.4:	Measurement locations on the human cadaver, where odd and even numbers represent top and bottom of the corresponding organs respectively.	51
Figure 3.5:	Average path loss for four anatomical regions in the simulation environment at 2.4 GHz.	52
Figure 3.6:	Average path loss on torso in the simulation environment at 915 MHz and 2.4 GHz.	53
Figure 3.7:	Scatter plots of path loss vs <i>in vivo</i> depth in the simulation environment at: (a) 915 MHz; (b) 2.4 GHz.	55
Figure 3.8:	Path loss versus <i>in vivo</i> depth from the body surface at 915 MHz.	58
Figure 3.9:	Simulation setup for the <i>in vivo</i> polarization investigation.	59
Figure 3.10:	Received power for various polarization mismatch angles in the simulation environment at 915 MHz.	59

Figure 3.11: Simulation setup for the <i>in vivo</i> delay spread investigation.	61
Figure 3.12: Power delay profiles for each anatomical direction in the simulation environment at 915 MHz.	62
Figure 4.1: SSVEP response to frequency-coded stimuli at the occipital region of the brain.	65
Figure 4.2: The PSD of EEG signal when a visual stimulus at 28 Hz is presented to a participant.	67
Figure 4.3: SSVEP response to pattern reversal stimuli ranging in frequency from 5.1 Hz to 84 Hz [71].	70
Figure 4.4: A bio-inspired filter design to capture SSVEP response at \tilde{f}_k	71
Figure 4.5: (a) A sample BIFB design that mainly deals with low SNR at the high-frequency band (Dataset-A); (b) A sample BIFB design that mainly deals with frequency selectivity (Dataset-B).	72
Figure 4.6: Flowchart of the signal processing stages of an SSVEP-based BCI using the proposed BIFBs.	73
Figure 4.7: The mean recognition accuracy and ITR performance of the SSVEP recognition methods.	78

Abstract

Advances in science and technology have significantly improved our quality of life over the past decades. For example, wireless communication systems have evolved from basic voice services to delivering high-definition video for entertainment or business conferences at an accelerating pace. Furthermore, progress in cyber-physical systems has led to the development of brain-computer interfaces and wireless body area networks with the vision of advanced pervasive healthcare, anytime and anywhere. The primary motivation of this dissertation is to improve the performance of the next-generation multi-service communication and medical cyber-physical systems.

The research has been concentrated in physical (PHY)/medium access control (MAC) layer aspects (such as channel modeling, waveform design, scheduling, and interference management) of wireless communication systems and signal processing algorithms for medical cyber-physical system. More specifically, the dissertation addresses the following topics:

Inter-Numerology Interference Management for 5G Mobile Network: The next-generation communication technologies are evolving towards increased flexibility in various aspects. Although orthogonal frequency division multiplexing (OFDM) remains as the waveform of the upcoming fifth-generation (5G) standard, the new radio provides flexibility in waveform parametrization (a.k.a. numerology) to address diverse requirements. However, managing the peaceful coexistence of mixed numerologies is challenging due to inter-numerology interference (INI). The utilization of adaptive guards in both time and frequency domains is proposed as a solution along with a multi-window operation in the PHY layer. Since the allowed interference level depends on the numerologies operating in the adjacent bands, the potential of adaptive guards is further increased and exploited with a MAC layer scheduling technique as well in this study.

In Vivo Channel Modeling for Wireless Body Area Networks: *In vivo* wireless body area networks (WBANs) and their associated technologies are shaping the future of healthcare by providing continuous health monitoring and noninvasive surgical capabilities, in addition to remote diagnostic and treatment of diseases. To fully exploit the potential of such devices, it is necessary to characterize the communication channel which will help to build reliable and high-performance communication systems. An *in vivo* wireless communication channel characterization for male torso both numerically and experimentally (on a human cadaver) is presented considering various organs. A statistical path loss model is introduced, and the anatomical region-specific parameters are provided. Multipath propagation characteristics are also investigated to facilitate proper waveform designs in the future wireless healthcare systems.

Frequency Recognition for SSVEP-based Brain-computer Interfaces: Brain-computer interfaces (BCIs) and their associated technologies have the potential to shape future forms of communication, control, and security. Specifically, the steady-state visual evoked potential (SSVEP) based BCIs have the advantages of better recognition accuracy, and higher information transfer rate (ITR) compared to other BCI modalities. To fully exploit the capabilities of such devices, it is necessary to understand the underlying biological features of SSVEPs and design the system considering their inherent characteristics. Bio-inspired filter banks (BIFBs) are introduced for improved SSVEP frequency recognition. SSVEPs are frequency selective, subject-specific, and their power gets weaker as the frequency of the visual stimuli increases. Therefore, the gain and bandwidth of the filters are designed and tuned based on these characteristics while also incorporating harmonic SSVEP responses in this study.

Chapter 1: Introduction

Advances in science and technology have significantly improved our quality of life over the past decades. For example, wireless communication systems have evolved from basic voice services to delivering high-definition video for entertainment or business conferences at an accelerating pace [1–3]. Furthermore, progress in medical cyber-physical systems has led to the development of brain-computer interfaces and wireless body area networks with the vision of advanced pervasive healthcare, anytime and anywhere [4–7]. The ongoing fifth-generation (5G) mobile network standardization activities, the recent proposal calls from governmental organizations for wireless body area networks research, and Silicon Valley’s great interest in brain-computer interfaces show that this remarkable momentum will continue exponentially in the years ahead.

The primary motivation of this dissertation is to improve the performance of the next-generation multi-service communication and medical cyber-physical systems. Fig. 1.1 illustrates the research domains and principal concepts that are studied in this dissertation. The essential background and the main contributions of this research are detailed in the following sections ¹.

1.1 Foundations of Multi-Numerology OFDM Systems for 5G Mobile Network

The standardization activities of wireless mobile telecommunications were initiated with analog standards that were implemented in the 1980s, and a new generation is being developed almost every ten years to meet the exponentially growing market demand [9]. The transition from analog to digital started in second-generation (2G) systems, along with the use of mobile data services. The third-generation (3G) digital evolution allowed video calls and global positioning system (GPS) services on mobile devices. The fourth-generation (4G) systems pushed the limits of

¹Part of this chapter was published in [6, 8–11]. Permission is included in Appendix A.

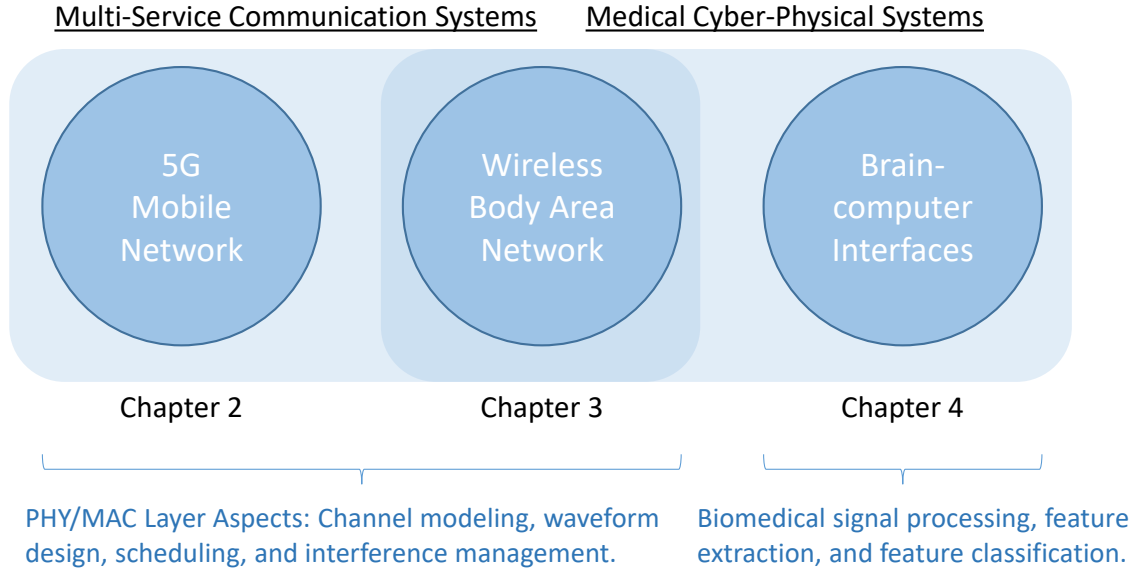


Figure 1.1: The research domains and main concepts that are studied in the dissertation.

data services further by better exploiting the time-frequency resources using orthogonal frequency-division multiple access (OFDMA) as an air interface. Currently, the study of 5G has almost been completed with harmony between academia, industry, and standardization entities [12], and the 5G test networks have been launched in several cities around the globe.

The next-generation wireless communication technologies are envisioned to support a diverse service variety under the same network. As a recent example, the International Telecommunications Union (ITU) [13] has defined the main use cases that are going to be supported in the 5G mobile network as enhanced mobile broadband (eMBB), massive machine-type communications (mMTC), and ultra-reliable low-latency communications (URLLC) as shown in Fig. 1.2. The applications which demand high data rate and better spectral efficiency fall into the eMBB category, whereas the ones which require ultra-high connection density and low power consumption falls into the mMTC category. Commonly, the industrial sensors or medical implants [6] should operate for many years without a maintenance need, and accordingly, high energy efficiency and low device complexity are essential for these mMTC services. Moreover, the mission-critical applications such as remote surgery [8] or self-driving vehicles [14] are categorized in URLLC. A flexible air interface is needed to meet these demanding service requirements under various channel conditions

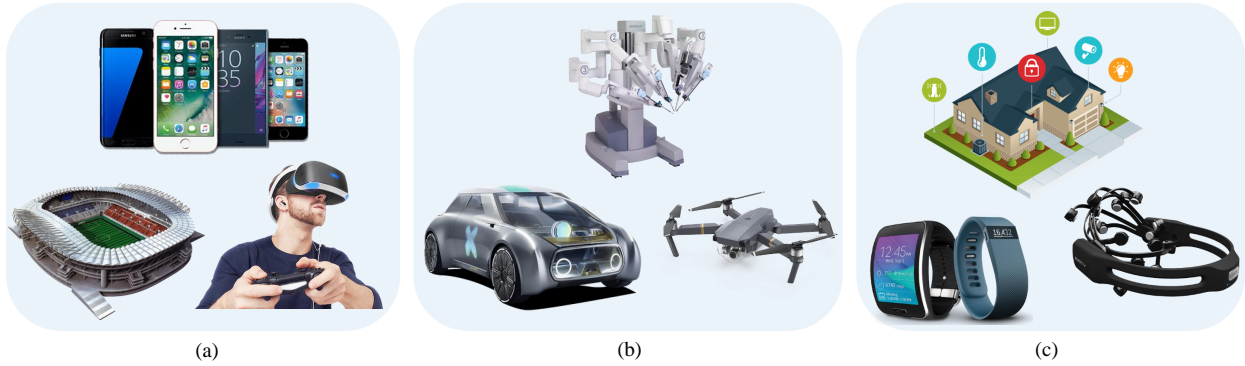


Figure 1.2: 5G use cases: (a) Enhanced mobile broadband, (b) ultra-reliable low-latency communications, and (c) massive machine type communications.

and system scenarios. Hence, the waveform, which is the main component of any air interface, must be designed precisely to facilitate such flexibility.

1.1.1 Waveform Definition

The waveform defines the physical shape of the signal that carries the modulated information through a channel. The information is mapped from the message space to the signal space at the transmitter, and a reverse operation is performed at the receiver to recover the message in a communications system. The waveform, which defines the structure and shape of the information in the signal space, can be described by its fundamental elements: symbol, pulse shape, and lattice [15]. The symbols constitute the random part of a waveform whereas the pulse shape and the lattice form the deterministic part.

- *Symbol*: A symbol is a set of complex numbers in the message space that is generated by grouping a number of bits together. The number of bits grouped within one symbol determines the modulation order that has a high impact on the throughput.
- *Pulse Shape*: The form of the symbols in the signal plane is defined by the pulse shaping filters. The shape of the filters determines how the energy is spread over the time and frequency domains and has an important effect on the signal characteristics.

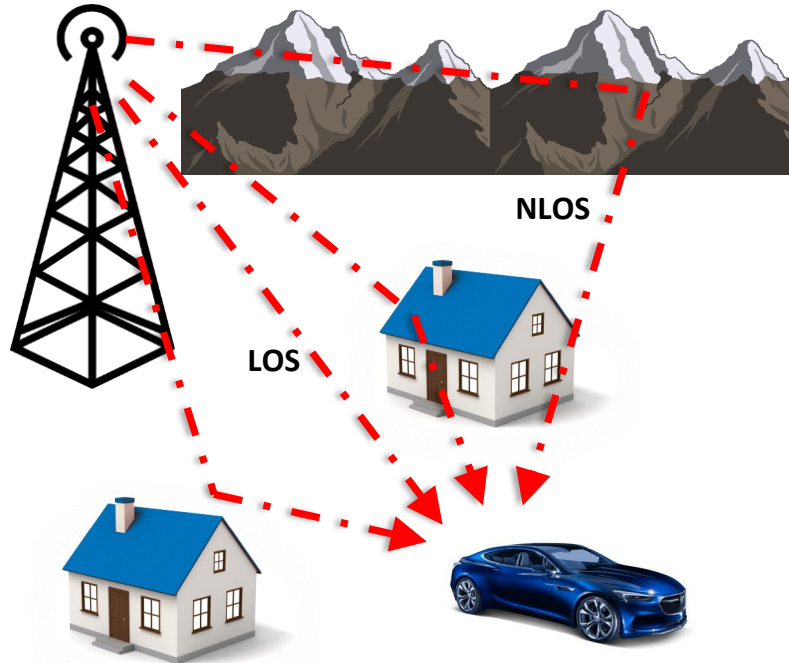


Figure 1.3: Wireless communications in the presence of a multipath propagation.

- *Lattice*: The lattice is generated by sampling the time–frequency plane, and the locations of samples define the coordinates of the filters in the time–frequency grid. The lattice geometry might present different shapes such as rectangular and hexagonal according to the formation and distances between the samples. Furthermore, the lattice can be exploited by including additional dimensions such as space domain.

1.1.2 Wireless Communications in the Presence of Multipath Channel

A transmitted signal may arrive at a receiver either directly (i.e., line-of-sight (LOS)) or after being reflected from various objects in the environment (i.e., non-line-of-sight (NLOS)). These reflected signals from different surfaces travel through different paths and accordingly reach the transmitter with different delays and gains. This propagation environment is usually referred to as a multipath channel and illustrated in Fig. 1.3. Multipath propagation creates small-scale (Rayleigh) fading effects on the received signal, as shown in Fig. 1.4.

The multipath channel causes dispersion in the time-domain and produces inter-symbol interference (ISI). The dispersion in the time domain might lead to a frequency selective fading,

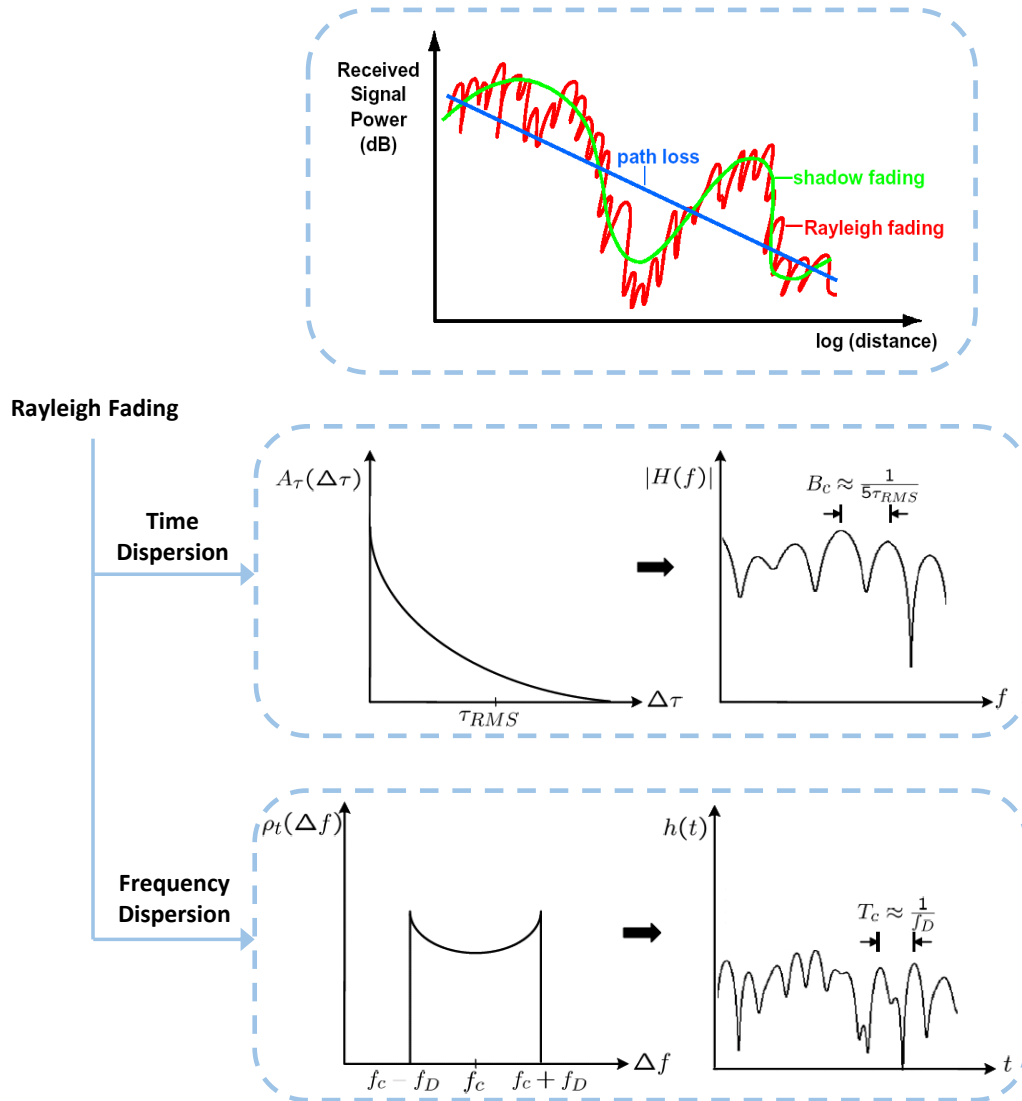


Figure 1.4: Time and frequency dispersive multipath channel.

depending on the transmission bandwidth of the signal. The coherence bandwidth of the channel (B_c) is defined as the bandwidth, in which the channel frequency response can be considered as flat (i.e., highly correlated). It is inversely proportional to the delay spread in the propagation environment. When the transmission bandwidth exceeds the coherence bandwidth of the channel, the signal experiences a frequency selective fading.

The frequency selective fading and ISI result in significant communication performance degradation. Channel equalizers are used to compensate for the ISI effect of the multipath channel. The complexity of these equalizers depends on the number of resolvable channel taps. Single-

carrier systems transceive signals with shorter symbol duration compared to multi-carrier systems, which utilize the same transmission bandwidth, and they resolve more channel taps. As a result, sophisticated equalizers are required for broadband single-carrier systems.

Mobility in free space or LOS multipath propagation environments, where a single dominant multipath component exists, leads to a Doppler shift issue. Handling the Doppler shift is straightforward, and pilot based techniques can be used to estimate and compensate the frequency offset resulting from the Doppler shift effect. However, if the number of multipath components is large, and they arrive at a receiver from different angles, Doppler spread occurs. Doppler spread is a combination of different Doppler shifts, and unlike the Doppler shift issue, it is hard to deal with due to its random nature.

Mobility in a multipath channel causes dispersion in the frequency-domain. The dispersion in the frequency domain might lead to a time selective fading, depending on the symbol duration of the signal. The coherence time of the channel (T_c) is defined as the duration, in which the channel time response can be considered as flat (i.e., highly correlated). It is inversely proportional to the Doppler spread in the propagation environment. When the symbol duration exceeds the coherence time of the channel, the signal experiences a time selective fading.

1.1.3 CP-OFDM and Multi-Numerology Systems

Orthogonal frequency-division multiplexing (OFDM) is the most popular multicarrier modulation scheme that is currently being deployed in many standards such as the downlink of 4G LTE and the IEEE 802.11 family [16]. Its primary advantage over the single-carrier transmission schemes is its ability to cope with frequency selective channels for broadband communications. The transmission bandwidth is divided into several narrow sub-channels, and the data is transmitted in parallel over these sub-channels with a set of narrow subcarriers. If the bandwidth of each subcarrier is set to be less than the coherence bandwidth of the channel, each subcarrier experiences a single-tap flat fading channel. As a result, the complex equalizers that are required for broadband single-carrier communications to combat ISI can be avoided with a proper design. Also, OFDM

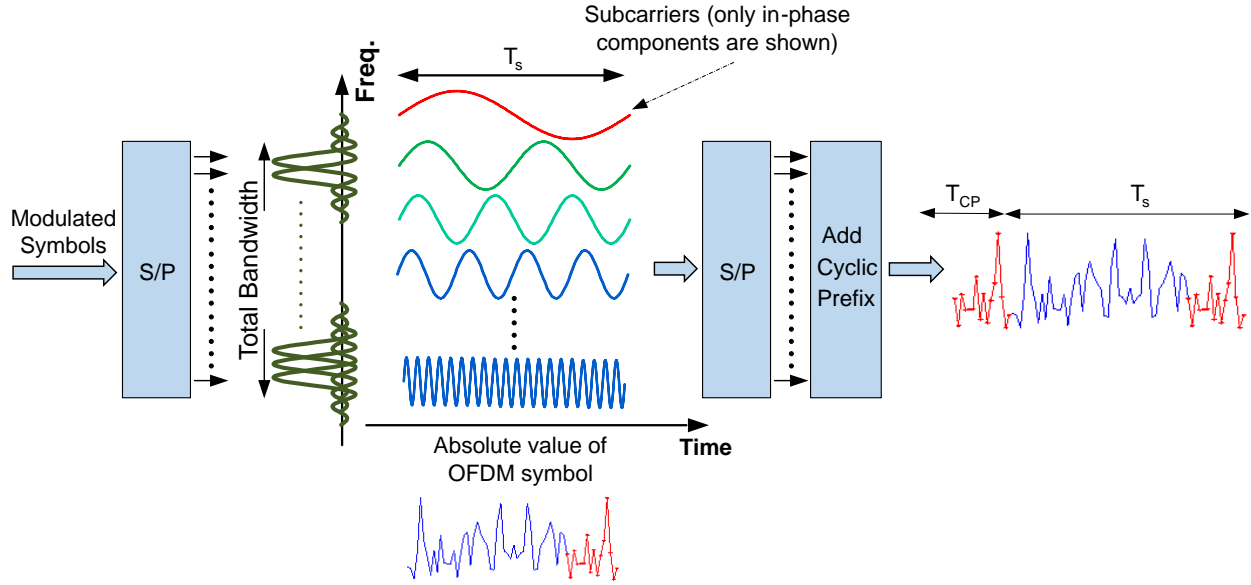


Figure 1.5: Illustration of a CP-OFDM symbol formation at the transmitter.

systems utilize the spectrum in a very efficient manner due to the orthogonally overlapped subcarriers and allow flexible frequency assigning. A discrete OFDM signal on baseband is expressed as follows:

$$s_{OFDM}[n] = \sum_{k=0}^{N-1} d_k e^{j2\pi nk/N} \quad (1.1)$$

where d_k is the complex data symbol at subcarrier k , and N represents the total number of subcarriers. OFDM can easily be implemented by the inverse fast Fourier transform (IFFT) algorithm. Afterward, the cyclic prefix (CP) is added by copying the last part of the IFFT sequence and appending it to the beginning as a guard interval. Its length is determined based on the maximum excess delay of the channel, which is defined as the delay between the first and last received paths over the channel. The CP-OFDM symbol formation at the transmitter is shown in Fig. 1.5. Also, a block diagram of conventional CP-OFDM transmitter and receiver is shown in Fig. 1.6. The channel between the transmitter and receiver can be considered as a filter, and a transmitted signal arrives at a receiver after convolving with the channel. This convolution operation in the time-domain corresponds to a multiplication operation in the frequency-domain if the channel is circular. The CP

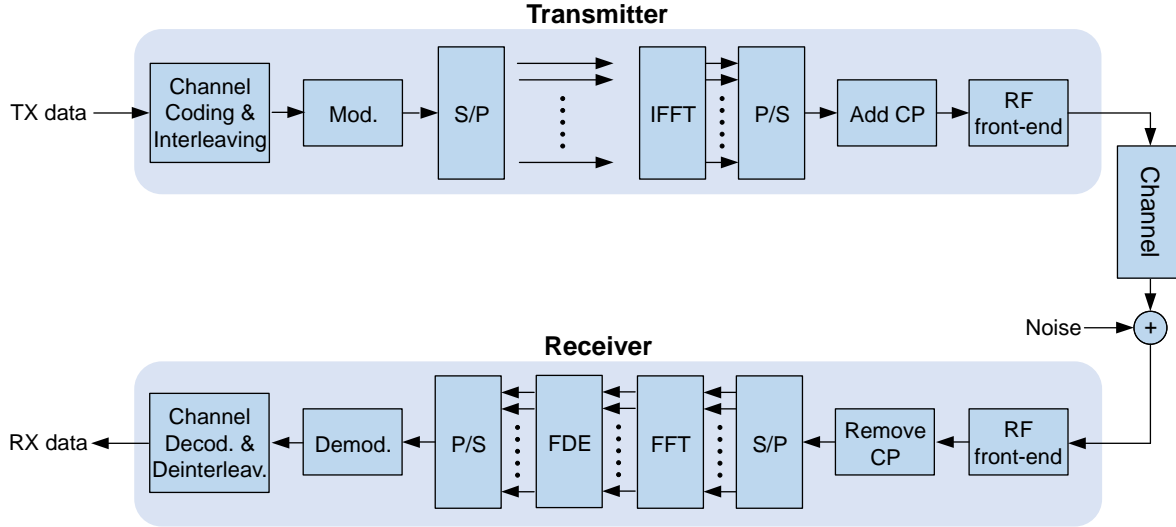


Figure 1.6: CP-OFDM block diagram: (a) Transmitter, (b) receiver.

part of the OFDM signal ensures the circularity of the channel and enables easy frequency-domain equalization (FDE) with a simple multiplication operation.

A major disadvantage of any multicarrier system, including CP-OFDM, is high peak-to-average power ratio (PAPR) due to the random addition of subcarriers in the time domain [17]. For instance, consider addition of sinusoidal signals with different frequencies and phase shifts. The resulting signal envelope presents high peaks when the peak amplitudes of the different signals are aligned at the same time. As a result of such high peaks, the power amplifier at the transmitter operates in the nonlinear region causing a distortion and spectral spreading. In addition, as the number of subcarriers increases, the variance of the output power increases as well.

Another critical issue related to the CP-OFDM systems is its high out of band emissions (OOBE). The OFDM signal is well localized in the time domain with a rectangular pulse shape that results in a sinc shape in the frequency domain. Especially, the sidelobes of the sincs at the edge carriers cause significant interference and should be reduced to avoid adjacent channel interference (ACI). Typically, OOBE is reduced by various windowing/filtering approaches along with the guard band allocation to meet the spectral mask requirements of the various standards. 3GPP LTE standard uses 10% of total bandwidth as guard bands to handle this problem. However, fixed guard allocation decreases the spectral efficiency.

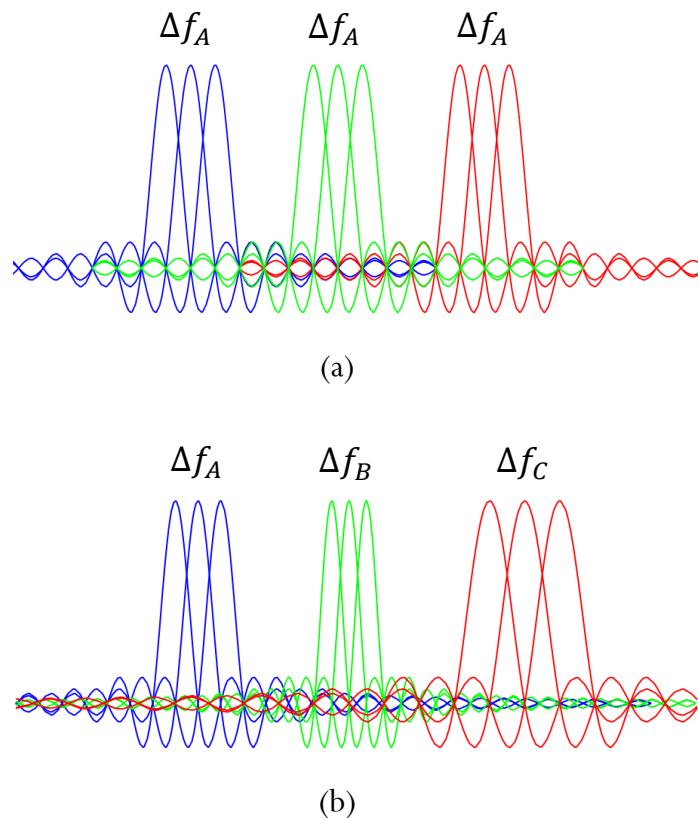


Figure 1.7: Multi-user OFDM spectrum: (a) Single numerology system, (b) multi-numerology system.

Numerous waveforms have been proposed [9, 18–22] considering disadvantages of OFDM, but none of them can address all the requirements of the upcoming 5G standard [23]. Therefore, OFDM remains as the waveform of the new radio [2, 24, 25], and a flexible waveform parametrization, which is also known as numerology [26, 27], is introduced to embrace diverse requirements as shown in Fig. 1.7.

The channel conditions, use cases, and system scenarios are the most critical considerations for the numerology design. For instance, a time-localized pulse shape is preferable for time-dispersive channels (i.e., high delay spread scenario), while a frequency-localized pulse shape is more suitable for frequency-dispersive channels (i.e., high Doppler spread scenario). Particularly, the frequency domain localization is crucial for asynchronous transmissions across adjacent subbands. Another degree of freedom, the subcarrier spacing in OFDM systems, should be kept

large to handle the Doppler spread in a highly mobile environment. On the other hand, a smaller subcarrier spacing provides a longer symbol duration and decreases the relative redundancy that is allocated for time dispersion. The reduced redundancy is especially important for the eMBB services. Furthermore, reliability and latency are vital for mission-critical communications where errors and retransmissions are less tolerable. Thus, a strict frequency localization and a short symbol duration (i.e., large subcarrier spacing) are more practical for the URLLC applications. Also, mMTC operates at a low power level to save energy and might seriously suffer from interference in an asynchronous heterogeneous network. Therefore, a more localized pulse shape in the frequency domain is more suitable in this case.

An efficient numerology design ensures better utilization of spectral resources and will be one of the core technologies to embrace diverse requirements in the new radio. However, managing the coexistence of multiple numerologies in the same network is challenging. Although OFDM numerologies are orthogonal in the time domain, any mismatch in parametrization such as subcarrier spacing leads to inter-numerology interference (INI) in the frequency domain [26, 28] as shown in Fig. 1.7-(b).

Chapter 2 proposes the utilization of adaptive guards in both time and frequency domains as a solution to INI issue along with a multi-window operation in the physical (PHY) layer. The adaptive windowing operation needs a guard duration to reduce the unwanted emissions, and a guard band is required to handle the INI level on the adjacent band. The guards in both domains are jointly optimized with respect to the subcarrier spacing, use case (i.e., service requirement), and power offset between the numerologies. Also, the multi-window approach provides managing each side of the spectrum independently in case of an asymmetric interference scenario. Since the allowed interference level depends on the numerologies operating in the adjacent bands, the potential of adaptive guards is further increased and exploited with a medium access control (MAC) layer scheduling technique. The proposed INI-based scheduling algorithm decreases the need for guards by allocating the numerologies to the available bands, considering their subcarrier spacing, power level, and SIR requirements. Therefore, INI management is performed with a cross-layer (PHY

and MAC) approach in this study. The results show that the precise design that accommodates such flexibility reduces the guards significantly and improves the spectral efficiency of multi-numerology systems.

1.2 Foundations of *In Vivo* Channel Modeling for Wireless Body Area Networks

Technological advances in biomedical engineering have significantly improved the quality of life and increased life expectancy of many people. One component of such advanced technologies is represented by wireless *in vivo* sensors and actuators, such as pacemakers, internal drug delivery devices, nerve stimulators, and wireless capsule endoscopes (WCEs). *In vivo*-wireless body area networks (WBANs) [29] and their associated technologies are the next step in this evolution and offer a cost efficient and scalable solution with the integration of wearable devices. *In vivo*-WBAN devices can provide continuous health monitoring and reduce the invasiveness of surgery. Furthermore, the patient information can be collected over a larger period of time and physicians are able to perform more reliable analysis by exploiting this *big data* rather than relying on the data recorded in short hospital visits [5, 30].

In order to fully exploit and increase further the potential of WBANs for practical applications, it is necessary to enhance our knowledge about the propagation of electromagnetic (EM) waveforms in an *in vivo* communication environment (implant-to-implant and implant-to-external device) and obtain accurate channel models that are necessary to optimize the system parameters and build reliable, efficient, and high-performance communication systems. In particular, creating and accessing such a model is necessary for achieving high data rates, target link budgets, determining optimal operating frequencies, and designing efficient antennas and transceivers including digital baseband transmitter/receiver algorithms. Therefore, investigation of the *in vivo* wireless communication channel is crucial to obtain a better performance for *in vivo*-WBAN devices and systems. Although, on-body wireless communication channel characteristics have been well investigated [5], there are relatively few studies of *in vivo* wireless communication channels [6, 8, 31].

While there exist multiple approaches to *in vivo* communications, EM communications is the focus of the study. Since the EM wave propagates through a very lossy environment inside the body and predominant scatterers are present in the near-field region of the antenna, *in vivo* channel exhibits different characteristics than those of the more familiar wireless cellular and Wi-Fi environments. In this subsection, the foundations of *in vivo* channel characterization is discussed.

1.2.1 Human Body Models and Propagation Through Tissues

In order to investigate the *in vivo* wireless communication channel, accurate body models and knowledge of the electromagnetic properties of the tissues are crucial. Human autopsy materials and animal tissues have been measured over the frequency range from 10 Hz to 20 GHz [32] and the frequency-dependent dielectric properties of the tissues are modeled by four-pole Cole-Cole equation, which is expressed as:

$$\varepsilon(\omega) = \varepsilon_{\infty} + \sum_{m=1}^4 \frac{\Delta\varepsilon_m}{1 + (j\omega\tau_m)^{(1-\alpha_m)}} + \frac{\sigma}{j\omega\varepsilon_0}, \quad (1.2)$$

where ε_{∞} stands for the body material permittivity at terahertz frequency, ε_0 denotes the free-space permittivity, σ represents the ionic conductivity and ε_m , τ_m , α_m are the body material parameters for each anatomical region. The electromagnetic properties such as conductivity, relative permittivity, loss tangent, and penetration depth can be derived using these parameters in Eq. 1.2.

Various physical and numerical phantoms have been designed in order to simulate the dielectric properties of the tissues for experimental and numerical investigation. These can be classified as homogeneous, multi-layered and heterogeneous phantom models. Although, heterogeneous models provide more realistic approximation to the human body, design of physical heterogeneous phantoms is quite difficult and performing numerical experiments on these models is very complex and resource intensive. On the other hand, homogeneous or multi-layer models cannot differentiate the EM wave radiation characteristics for different anatomical regions. Fig. 1.8 shows examples of heterogeneous physical and numerical phantoms.

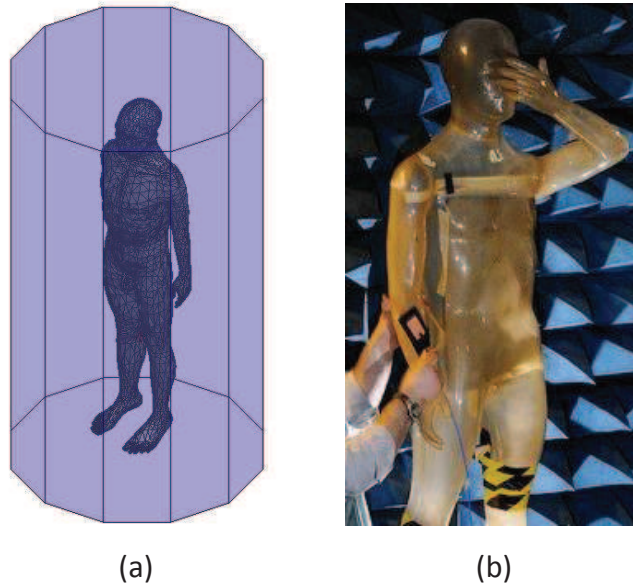


Figure 1.8: Heterogeneous human body models: (a) HFSS[®] model, (b) physical phantom [33].

Analytical methods are generally viewed as infeasible and require extreme simplifications. Therefore, numerical methods are used for characterizing the *in vivo* wireless communication channel. Numerical methods provide less complex and appropriate approximations to Maxwell's equations via various techniques, such as uniform theory of diffraction (UTD), finite integration technique (FIT), method of moments (MoM), finite element method (FEM) and finite-difference time-domain method (FDTD). Each method has its own pros and cons and should be selected based on the simulation model and size, operational frequency, available computational resources and interested characteristics such as power delay profile (PDP), specific absorption rate (SAR), etc. A detailed comparison for these methods is available in [32] and [34].

It may be preferable that numerical experiments should be confirmed with real measurements. However, performing experiments on a living human is carefully regulated. Therefore, anesthetized animals [35, 36] or physical phantoms, allowing repeatability of measurement results, [33, 37] are often used for experimental investigation. In addition, the first study conducted on a human cadaver was reported in [38].

Propagation in a lossy medium, such as human tissues, results in a high absorption of EM energy. The absorption effect varies with the frequency dependent electrical characteristics of the tissues, which mostly consist of water and ionic content [39]. The specific absorption rate (SAR) provides a metric for the absorbed power amount in the tissue and is expressed as follows:

$$SAR = \frac{\sigma |E|^2}{\rho}, \quad (1.3)$$

where σ , E and ρ represent the conductivity of the material, the RMS magnitude of the electric field and the mass density of the material, respectively. The Federal Communications Commission (FCC) recommends the SAR to be less than 1.6 W/kg taken over a volume having 1 gram of tissue [40].

When an EM plane wave propagates through the interface of two media having different electrical properties, its energy is partially reflected and the remaining portion is transmitted through the boundary of these mediums. Superposition of the incident and the reflected wave can cause a standing wave effect that may increase the SAR values [39]. A multi-layer tissue model at 403 MHz, where each layer extends to infinity (much larger than the wavelength of EM waves) is illustrated in Fig. 1.9. The dielectric values and power transmission factors of this model were calculated in [41]. If there is a high contrast in the dielectric values of mediums/tissues, wave reflection at the boundary increases and transmitted power decreases. The limitations on communications performance imposed by the SAR limit have been investigated in [40].

In addition to the absorption and reflection losses, EM waves also suffers from expansion of the wave fronts (which assume an ever-increasing sphere shape from an isotropic source in free space), diffraction and scattering (which depend on the EM wavelength). Section 1.2.3 discusses *in vivo* propagation models by considering these effects in detail.

1.2.2 Frequency of Operation and Antenna Design Considerations

Since EM waves propagate through the frequency dependent materials inside the body, the operating frequency has an important effect on the communication channel. Accordingly, the

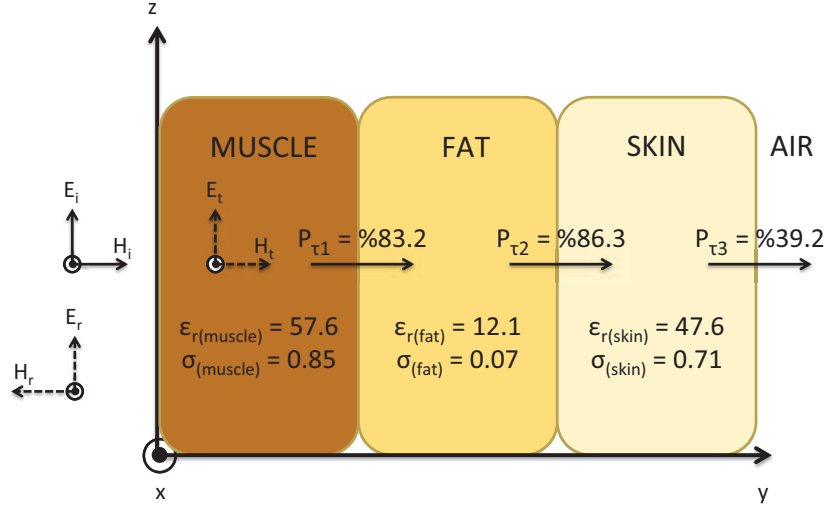


Figure 1.9: Multi-layer human tissue model at 403 MHz (ϵ_r : Permittivity, σ : Conductivity, P_τ : Power transmission factor).

allocated and recommended frequencies including their effects for *the in vivo* wireless communications are summarized in this subsection. Furthermore, unlike free-space communications, *in vivo* antennas are often considered to be an integral part of the channel and they generally require different specifications than the *ex vivo* antennas [32, 42–44]. Hence, their salient differences as compared to *ex vivo* antennas are described as well.

The IEEE 802.15.6 standard [29] was released in 2012 to regulate short-range wireless communications inside or in the vicinity of the human body, and are classified as human-body communications (HBC) [45], narrow band (NB) communications, and ultra-wide band communications (UWB). The frequency bands and channel bandwidths (BW) allocated for these communication methods are summarized in Table 1.1. An IEEE 802.15.6 compliant *in vivo*-WBAN device must operate in at least one of these frequency bands.

NB communications operates at lower frequencies compared to UWB communications and hence suffer less from absorption. This can be appreciated by considering Eq. 1.2 and Eq. 1.3 that describe the absorption as a function of frequency. The medical device radio communications service (MedRadio uses discrete bands within the 401-457 MHz spectrum including international medical implant communication service (MICS) band) and medical body area network (MBAN, 2360-2400 MHz) are allocated by the FCC for medical devices usage. Therefore, co-user inter-

Table 1.1: Frequency bands and bandwidths for the three different propagation methods in IEEE 802.15.6.

Propagation Method	IEEE 802.15.6 Operating Freq. Bands	
	Frequency Band	BW
Narrow Band Communications	402 - 405 MHz	300 kHz
	420 - 450 MHz	300 kHz
	863 - 870 MHz	400 kHz
	902 - 928 MHz	500 kHz
	950 - 956 MHz	400 kHz
	2360 - 2400 MHz	1 MHz
	2400 - 2438.5 MHz	1 MHz
UWB Communications	3.2 - 4.7 GHz	499 MHz
	6.2 - 10.3 GHz	499 MHz
Human - Body Communications	16 MHz	4 MHz
	27 MHz	4 MHz

ference problems are less severe in these frequency bands. However, NB communications are only allocated small bandwidths (1 MHz at most) in the standard as shown in Table 1.1. The IEEE 802.15.6 standard does not define a maximum transmit power and the local regulatory bodies limit it. The maximum power is restricted to $25 \mu\text{W}$ EIRP (Equivalent Isotropic Radiated Power) by FCC, whereas it is set to $25 \mu\text{W}$ ERP (Equivalent Radiated Power) by ETSI (European Telecommunication Standards Institute) for the 402-405 MHz band.

UWB communications is a promising technology to deploy inside the body due to its inherent features including high data rate capability, low power, improved penetration (propagation) abilities through tissues and low probability of intercept. The large bandwidths for UWB (499 MHz) enable high data rate communications and applications. Also, UWB signals are inherently robust against detection and smart jamming attacks because of their extremely low maximum EIRP spectral density, which is -41.3 dBm/MHz [46]. On the other hand, UWB communications inside the body suffer from pulse distortion caused by frequency dependent tissue absorption and the limitations imposed by compact antenna design.

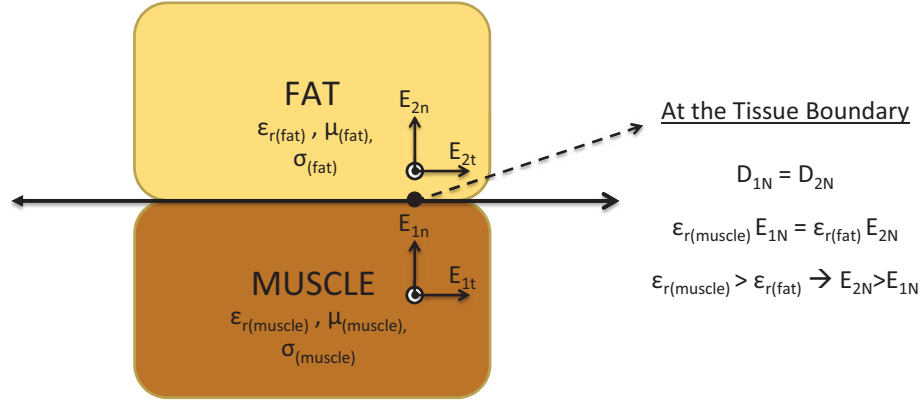


Figure 1.10: EM propagation through tissue interface.

In vivo antennas are subject to strict size constraints and in addition, they need to be biocompatible. Although, copper antennas have better performance, only specific types of materials such as titanium or platinum should be used for *in vivo* communications due to their noncorrosive chemistry [5]. The standard definition of the gain is not valid for *in vivo* antennas since it includes body effects [47]. As noted above, the gain of the *in vivo* antennas cannot be separated from the body effects as the antennas are considered to be an integral part of the channel. Hence, the *in vivo* antennas should be designed and placed carefully. When the antennas are placed inside the human body, their electrical dimensions and gains decrease due to the high dielectric permittivity and high conductivity of the tissues, respectively [48]. For instance, fat has a lower conductivity than skin and muscle. Therefore, *in vivo* antennas are usually placed in a fat (usually subcutaneous fat) layer to increase the antenna gain. This placement also provides less absorption losses due to shorter propagation path. However, the antenna size becomes larger in this case. In order to reduce high losses inside the tissues, a high permittivity, low loss coating layer can be used. As the coating thickness increases, the antenna becomes less sensitive to the surrounding material [48].

Lossy materials covering the *in vivo* antenna change the electrical current distribution in the antenna and radiation pattern. It is reported in [42] that directivity of *in vivo* antennas increases due to curvature of body surface, losses and dielectric loading from the human body. Therefore, this increased directivity should be taken into account as well in order not to harm the tissues in the vicinity of the antenna.

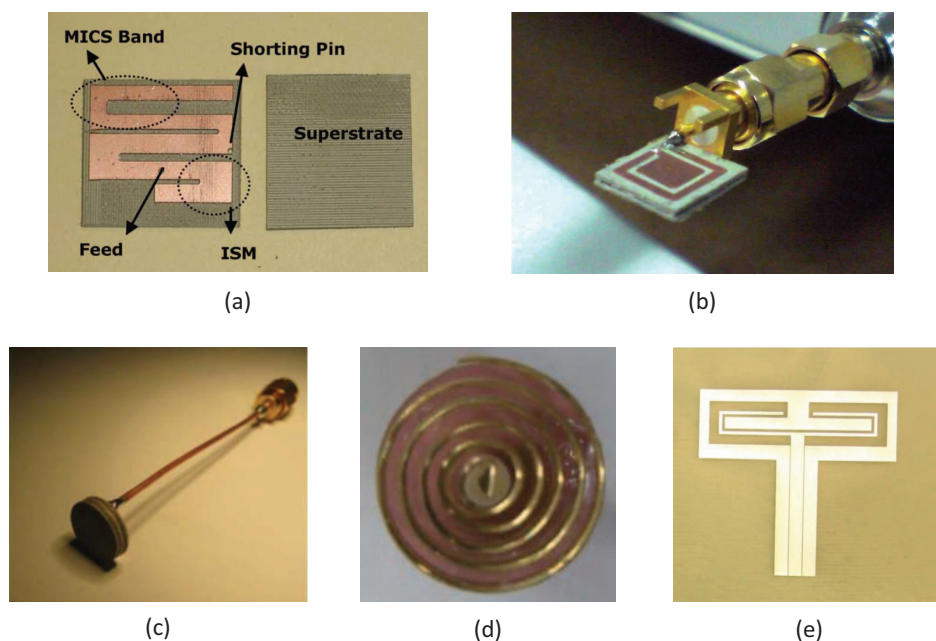


Figure 1.11: Selected *in vivo* antenna samples: a) A dual-band implantable antenna [49], b) A miniaturized implantable broadband stacked planar inverted-F antenna (PIFA) [50], c) A miniature scalp-implantable [30], d) A wideband spiral antenna for WCE [35], e) An implantable folded slot dipole antenna [51].

In vivo antennas can be classified into two main groups as electrical and magnetic antennas. Electrical antennas, e.g., dipole antennas, generate electric fields (E-field) normal to the tissues, while magnetic antennas, e.g., loop antennas produce E-fields tangential to the human tissues [39]. Normal E-field components at the medium interfaces overheat the tissues due to the boundary condition requirements as illustrated in Fig. 1.10. The muscle layer has a larger permittivity value than the fat layer and hence, the E-field increases in the fat layer. Therefore, magnetic antennas allow higher transmission power for *in vivo*-WBAN devices as can be understood from Eq. 1.3. In practice, magnetic loop antennas require large sizes, which is a challenge to fit inside the body. Accordingly, smaller size spiral antennas having a similar current distribution as loop antennas can be used for *in vivo* devices [35]. Representative antennas designed for *in vivo* communications are shown in Fig. 1.11.

1.2.3 EM Wave Propagation Models for *In Vivo* Communications

Up to this point, important factors for *in vivo* wireless communication channel characterization, such as EM modeling of the human body, propagation through the tissues, selection of the operational frequencies, and *in vivo* antenna design considerations have been reviewed. In this subsection, EM wave propagation inside the human body considering the anatomical features of organs and tissues is discussed. Also, the analytical and statistical path loss models are presented. Since the EM wave propagates through a very lossy environment inside the body and predominant scatterers are present in the near-field region of the antenna, *in vivo* channel exhibits different characteristics than those of the more familiar wireless cellular and Wi-Fi environments.

EM wave propagation inside the body is subject-specific and strongly related to the location of antenna as demonstrated in [37, 42, 52] and [53]. Therefore, channel characterization is mostly investigated for a specific part of the human body. For example, the heart area has been studied for implantable cardioverter defibrillator and pacemakers, while the gastrointestinal tract (GI) including esophagus, stomach and intestine has been investigated for WCE applications. The bladder region is studied for wirelessly controlled valves in the urinary tract and the brain is investigated for neural implants [44, 54]. Also, clavicle, arm and hands are specifically studied as they are affected less by the *in vivo* medium.

When the *in vivo* antenna is placed in an anatomically complex region, path loss, a measure of average signal power attenuation, increases [52]. This is the case with the intestine which presents a complex structure with repetitive, curvy-shaped, dissimilar tissue layers, while the stomach has a smoother structure. As a result, the path loss is greater in the intestine than in the stomach even at equal *in vivo* antenna depths.

Various analytical and statistical path loss formulas have been proposed for the *in vivo* channel in the literature as listed in Table 1.2. These formulas have been derived considering different shadowing phenomena for the *in vivo* medium. The initial three models are functions of the Friis transmission equation [32], return loss and absorption in the tissues. These models are

Table 1.2: A review of selected studied path loss models for various scenarios.

Model	Formulation
FSPL	$P_r = P_t G_t G_r \left(\frac{\lambda}{4\pi R}\right)^2$
FSPL with RL	$P_r = P_t G_t (1 - S_{11} ^2) G_r (1 - S_{22} ^2) \left(\frac{\lambda}{4\pi R}\right)^2$
FSPL with RL and Absorption	$P_r = P_t G_t (1 - S_{11} ^2) G_r (1 - S_{22} ^2) \left(\frac{\lambda}{4\pi R}\right)^2 (e^{-\alpha R})^2$
PMBA for near and far field	$P_{rn} = \frac{16\delta(P_t - P_{NF})}{\pi L^2} A_e, P_{rf} = \frac{(P_t - P_{NF} - P_{FF})\lambda^2}{4\pi R^2} G_t G_r$
Statistical Model-A	$PL(d) = PL_0 + n(d/d_0) + S \quad (d_0 \leq d)$
Statistical Model-B	$PL(d) = PL(d_0) + 10n \log_{10}(d/d_0) + S \quad (d_0 \leq d)$

P_r/P_t stands for the received/transmitted power; G_r/G_t denotes the gain of the receiver/transmitter antenna; λ represents the free space wavelength; R is the distance between transmitter and receiver antennas; $|S_{11}|$ and $|S_{22}|$ are the reflection coefficients of receiver/transmitter antennas; α is the attenuation constant; P_{NF}/P_{FF} is the loss in the near/far fields; P_{rn} & P_{rf} represents received power for near and far fields; δ is A_e/A where A_e is the effective aperture and A is the physical aperture of the antenna; L is the largest dimension of the antenna; d is the depth distance from the body surface; d_0 is the reference depth distance; n is the path loss exponent; PL_0 is the intersection term in dB; S denotes the random shadowing term. Abbreviations: FSPL represents free space path loss in the far field, RL is the return loss, PMBA is the propagation loss model.

valid, when either the far field conditions are fulfilled or few scattering objects exist between the transmitter and receiver antennas.

In the first model, free space path loss (FSPL) is expressed by the Friis transmission equation. FSPL mainly depends on gain of antennas, distance and operating frequency. Its dependency on distance is a result of expansion of the wave fronts as explained in Section III. Additionally, FSPL is frequency dependent due to the relationship between the effective area of the receiver antenna and the wavelength. The following two equations in Table III are derived including antenna return loss and absorption in the tissues to the FSPL model. Then, another analytical model, PMBA, calculates the SAR over the entire human body for the far and near fields, and gives the received power using the calculated absorption. Although, these analytical expressions provide intuition about each component of the propagation models, they are not practical for link budget design as similar to the wireless cellular environment.

The free space path loss (FSPL) is expressed by the Friis transmission equation in the first model in Table 1.2. The FSPL mainly depends on gain of antennas, distance, and operating frequency. Its dependency on distance is a result of expansion of the wave fronts as explained in Section III. Additionally, FSPL is frequency dependent due to the relationship between the effective area of the receiver antenna and wavelength. The two equations of the FSPL model in Table 1.2 are derived including the antenna return loss and absorption in the tissues. Another analytical model, PMBA [55], calculates the SAR over the entire human body for the far and near fields, and gives the received power using the calculated absorption. Although, these analytical expressions provide intuition about each component of the propagation models, they are not practical for link budget design as similar to the wireless cellular communication environment.

The channel modeling subgroup (Task Group 15.6), which worked on developing of IEEE 802.15.6 standard, submitted their final report on body area network (BAN) channel models in November 2010. In this report, it is determined that Friis transmission equation can be used for *in vivo* scenarios by adding a random variation term and the path loss was modeled statistically with a log-normal distributed random shadowing S and path loss exponent n [46]. The path loss exponent (n) heavily depends on environment and is obtained by performing extensive simulations and measurements. In addition, the shadowing term (S) depends on the different body materials (e.g. bone, muscle, fat, etc.) and the antenna gain in different directions [43]. The research efforts on assessing the statistical properties of the *in vivo* propagation channel are not finalized, and there are still many open research efforts dedicated to building analytical models for different body parts and operational frequencies [33, 42, 43, 53, 56].

Chapter 3 presents an *in vivo* wireless communication channel characterization for male torso both numerically and experimentally (on a human cadaver) considering various organs at 915 MHz and 2.4 GHz. A statistical PL model is introduced, and the anatomical region-specific parameters are provided. It is found that the mean PL in dB scale exhibits a linear decaying characteristic rather than an exponential decaying profile inside the body, and the power decay rate is approximately twice at 2.4 GHz as compared to 915 MHz. Moreover, the variance of shadowing

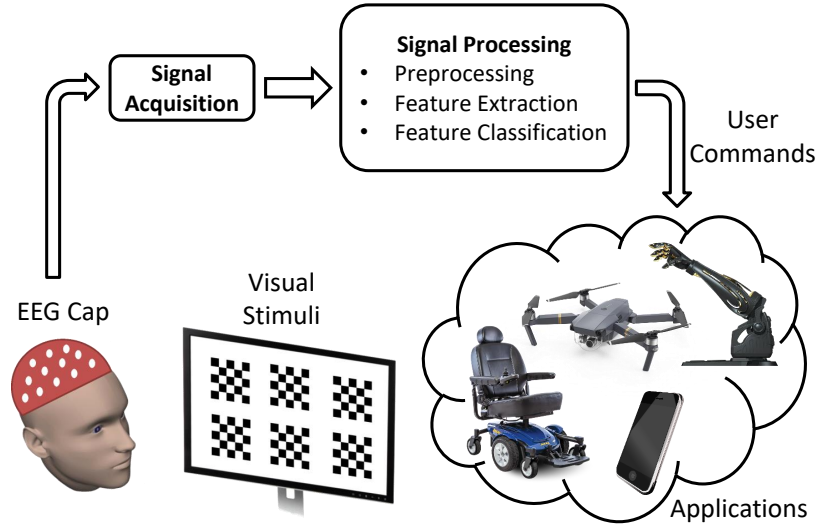


Figure 1.12: Functional model of an SSVEP-based BCI.

increases significantly as the *in vivo* antenna is placed deeper inside the body since the main scatterers are present in the vicinity of the antenna. Multipath propagation characteristics are also investigated to facilitate proper waveform designs in the future wireless healthcare systems. Results show that the *in vivo* channel exhibit different characteristics than the classical communication channels, and location dependency is very critical for accurate, reliable, and energy-efficient link budget calculations.

1.3 Foundations of SSVEP based Brain-computer Interfaces

1.3.1 Brain-computer Interfaces

Scientific advances in neuroscience and biomedical engineering enabled a direct communication channel between the human brain and a computer. The electrical activity in the brain that is produced by neuronal post-synaptic membrane polarity changes can be monitored to detect the user's intentions [57]. A brain-computer interface (BCI) [58] analyzes the brain signals and translates them into commands for external devices such as a speller device, wheelchair, robotic arm, or a drone (Fig. 1.12). Since BCIs utilize the signals generated by the central nervous system, the primary target of this technology is people with severe neuromuscular disorders (e.g., amyotrophic lateral sclerosis, brain-stem stroke, spinal cord injury, and cerebral palsy). However, advanced BCI

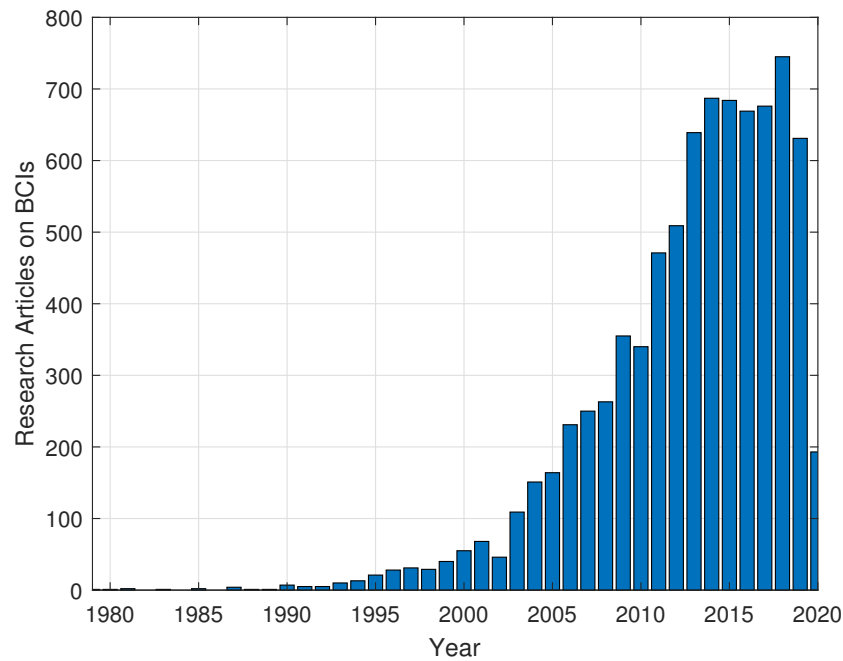


Figure 1.13: The number of articles on BCI research over years (The data is obtained from PubMed on March 21, 2020).

systems serve healthy people as well by providing an alternative way of communication, control, and security [59–61]. Hence, these systems have evolved to be a promising part of the body area network [5, 6, 8, 62, 63]. There is a growing interest in BCI research, and the number of scientific articles on this fascinating research field increases exponentially, as shown in Fig. 1.13.

1.3.2 Steady-state Visual Evoked Potentials

While there exist multiple approaches to measure brain activity (such as magnetoencephalogram (MEG), near-infrared spectroscopy (NIRS), electrocorticogram (ECoG), and functional magnetic resonance imaging (fMRI)), electroencephalography (EEG) is widely used in BCI applications because of its high temporal resolution, which is essential for BCIs to work as real-time systems [64]. In addition, EEG devices are inexpensive and portable. Various EEG signals could serve to drive BCIs. For example, a distinctive oscillation pattern in EEG is observed when a sensory stimulus such as visual or auditory is presented to a human. These oscillations are called as evoked potentials (EPs), and they disappear after a short period. If the stimulus is repeated

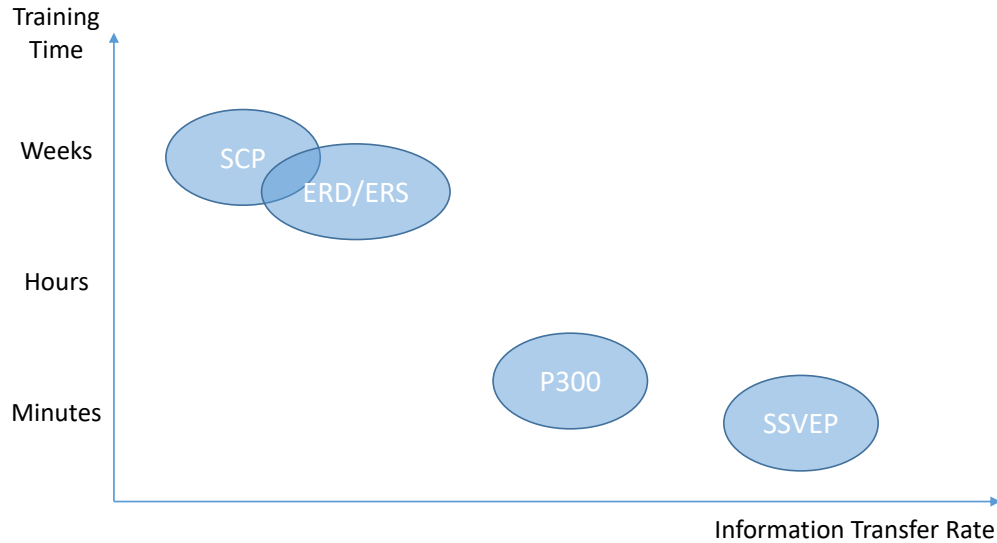


Figure 1.14: A comparison of various BCI modalities with respect to their training time and information transfer rate [69].

at a regular rate, the EPs do not have time to decay, and it causes a periodic response which is called as steady-state evoked potentials [65]. More specifically, a periodic visual stimulus with a repetition rate higher than 6 Hz elicits steady-state visual evoked potentials (SSVEPs) which are more prominent in the occipital region of the brain [4, 66]. The targets that evoke SSVEPs are encoded in various ways [60, 67], and the users make a selection by shifting their attention to the desired target in SSVEP based BCIs. Among other BCI modalities which depend on other EEG signals (e.g., slow cortical potentials, sensorimotor rhythms, and event-related potentials), SSVEP based BCIs have the advantage of high information transfer rate (ITR) and short training duration to operate the device [68] as shown in Fig. 1.14 [69].

SSVEPs are sinusoidal-like waveforms, and they appear at the same fundamental frequency of the driving stimulus and its harmonics (Fig. 1.15) [66]. However, spontaneous oscillations (i.e., background activity), which are not related to the stimulation, exist in the EEG recordings as well and a robust recognition algorithm is required to build a reliable BCI system. Numerous methods have been proposed for SSVEP recognition in the last decade [68, 70–75]. Power spectral density analysis (PSDA) is a typical approach since the distinctive features of SSVEPs are observed in the frequency domain [68]. However, PSDA is susceptible to noise, and long durations are needed to increase

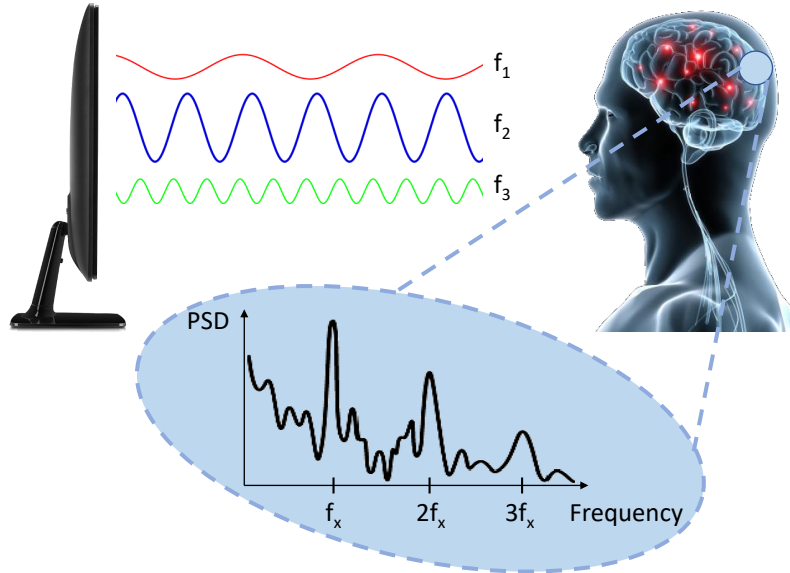


Figure 1.15: SSVEP response to frequency-coded stimuli at the occipital region of the brain.

the signal to noise ratio (SNR). A multivariable statistical method, namely canonical correlation analysis (CCA) [70, 72] exploits the multiple channel covariance information to enhance SNR and provide a better recognition accuracy compared to PSDA. Simple implementation, high robustness, and better ITR performance have made CCA attractive in SSVEP recognition research. On the other hand, CCA is not efficient to extract the discriminative information embedded in the harmonic components of SSVEPs, and filter-bank canonical correlation analysis (FBCCA) [73] is proposed to handle this issue. Although FBCCA captures the distinct spectral properties of multiple harmonic frequencies successfully, it neglects any correlation information between SSVEP responses at different frequencies [74]. Furthermore, this approach disregards the frequency selective nature of SSVEPs due to the utilization of wide-band filters which cover the whole stimuli bandwidth.

Chapter 4 introduces bio-inspired filter banks (BIFBs) for improved SSVEP frequency recognition. To fully exploit the capabilities of such devices, it is necessary to understand the underlying biological features of SSVEPs and design the system considering their inherent characteristics. SSVEPs are frequency selective, subject-specific, and their power gets weaker as the frequency of the visual stimuli increases. Therefore, the gain and bandwidth of the filters are designed and tuned based on these characteristics while also incorporating harmonic SSVEP responses.

The BIFBs are utilized in the feature extraction stage to increase the separability of classes. This method not only improves the recognition accuracy but also increases the total number of available commands in a BCI system by allowing the use of stimuli frequencies that elicit weak SSVEP responses. The BIFBs are promising particularly in the high-frequency band, which causes less visual fatigue. Hence, the proposed approach might enhance user comfort as well. The BIFB method is tested on two online benchmark datasets and outperforms the compared methods. The results show the potential of bio-inspired design, and the findings will be extended by including further SSVEP characteristics for future SSVEP based BCIs.

Chapter 2: Inter-numerology Interference Management with Adaptive Guards

2.1 Introduction

The next generation communication systems including 5G are expected to support high flexibility and a diverse range of services, unlike the previous standards. The IMT-2020 vision defines the use cases into three main categories as enhanced mobile broadband (eMBB), massive machine type communications (mMTC), and ultra-reliable low-latency communications (URLLC) featuring 20 Gb/s peak data rate, $10^6/\text{km}^2$ device density, and less than 1 ms latency, respectively [13]. The applications which demand high data rate and better spectral efficiency fall into the eMBB category, whereas the ones which require ultra-high connection density and low power consumption falls into the mMTC category. Moreover, the mission-critical applications, where errors and retransmissions are less tolerable, are categorized in URLLC. Therefore, a flexible air interface is required to meet these different requirements ².

Orthogonal frequency-division multiplexing (OFDM) is the most popular waveform that is currently being used in various standards such as 4G LTE and the IEEE 802.11 family [16]. It provides several tempting features such as efficient hardware implementation, low-complexity equalization, and easy multiple-input-multiple-output (MIMO) integration. On the other hand, OFDM seriously suffers from its high out-of-band emissions (OOBE), peak-to-average power ratio (PAPR), and strict synchronization requirements. In addition, 4G LTE adopts a uniform OFDM parameter configuration in pursuit of orthogonality and cannot serve different needs efficiently. Numerous waveforms have been proposed [9, 18–22] considering all these disadvantages, but none of them can address all the requirements of the upcoming 5G standard [23]. Therefore, OFDM

²This chapter was published in [11]. Permission is included in Appendix A.

remains as the waveform of the new radio [2, 24, 25], and a flexible waveform parametrization, which is also known as numerology [26, 27], is introduced to embrace diverse requirements.

The channel conditions, use cases, and system scenarios are the most critical considerations for the numerology design. For example, the subcarrier spacing of OFDM should be kept large to handle the Doppler spread in a highly mobile environment. On the other hand, a smaller subcarrier spacing provides a longer symbol duration and decreases the relative redundancy that is allocated for time dispersion. An efficient numerology design ensures better utilization of spectral resources and numerology multiplexing will be one of the core technologies in the new radio [76]. However, managing the coexistence of multiple numerologies in the same network is challenging. Although OFDM numerologies are orthogonal in the time domain, any mismatch in parametrization, such as subcarrier spacing, leads to inter-numerology interference (INI) in the frequency domain [26, 28]. Despite the fact that it is a new interference type, which will be an issue for 5G, extensive research led to in-depth INI analyses and various INI management techniques [26, 28, 77–83]. For instance, windowing [77, 78] and filtering [79, 81] operations are performed at both transmitter and receiver side along with the guard band allocation to mitigate the unwanted emissions from non-orthogonal numerologies. In addition, it is demonstrated that mixed transparent waveform processing can be applied to optimize the complexity-performance trade-off at transmitter and receiver separately [80]. Precoding techniques at the transmitter [82, 84] and interference cancellation algorithms at the receiver [77] are also considered for multi-numerology coexistence. Last but not least, waveform multiplexing [26, 83] is suggested for mixed numerology management as well. Among these physical (PHY) layer techniques, the windowing operation has a relatively less complexity, which is almost at the same level compared to CP-OFDM [80]. Also, the windowing approach preserves the essential structure of the OFDM transceivers and provides backward compatibility for the current OFDM-based systems. The windowing operation requires an extra period, which extends the guard duration between the consecutive OFDM symbols. Also, additional guard bands are still required between adjacent channels to deal with the INI. In other words, better interference mitigation is realized with the cost of reduced spectral efficiency.

Accordingly, the future communication systems have to optimize the guards in both time and frequency domains to improve the spectral efficiency.

This chapter proposes the utilization of adaptive guards along with a multi-window operation in the PHY layer to manage the INI, which is an issue in the mixed numerology systems. The guard band and the window parameters that handle the guard duration are jointly optimized regarding the subcarrier spacing, use case, and power offset between the numerologies. Also, the multi-window technique provides managing each side of the spectrum independently in case of an asymmetric interference scenario. Since the allowed interference level depends on the numerologies operating in the adjacent bands, the potential of adaptive guards is further increased and exploited with a medium access control (MAC) layer scheduling technique. The proposed INI-based scheduling algorithm decreases the need for guards by allocating the numerologies to the available bands, considering the subcarrier spacing, power level, and SIR requirements. Therefore, INI management is performed with a cross-layer (PHY and MAC) approach in this study. The preliminary results without a mixed-numerology guard optimization, a multi-window operation, or an elaborate INI-based scheduling algorithm and its evaluation were presented in [85]. Recently, a U.S. patent [86] is issued for the proposed technique and final research outcomes are published in [11] as well. The main contributions of this chapter are listed as follows:

- The key parameters for guard allocation are identified considering a mixed numerology system.
- The guards in both time and frequency domains are jointly optimized with respect to the subcarrier spacing, use case, and power offset between the numerologies.
- An interference based scheduling algorithm is proposed to decrease the need for guards.

The remaining part of this chapter is structured as follows. Section 2.2 is dedicated to the system model, and it describes the guard design methodology in detail. Section 2.3 presents the guard optimization procedure considering the key parameters of the mixed numerology system.

Section 2.4 introduces the INI-based scheduling algorithm along with the utilization of adaptive guards. Finally, Section 2.5 summarizes the contributions and concludes Chapter 2.

2.2 System Model

Consider the uplink of a multiuser OFDM system, where asynchronous numerologies with different subcarrier spacing, power level, and use case (i.e., service requirements) operate in the same network. Each numerology can serve multiple synchronous user equipments (UEs) and is assigned to a different bandwidth part (BWP) [24]. A transmitter windowing operation is performed to improve the spectral localization of numerologies and manage interference level on the adjacent BWPs. The guard duration that is allocated for the time-dispersive channel (i.e., T_{CP-Ch}) is fixed, and it is adequate to deal with the inter-symbol interference (ISI). Also, an extra guard duration is needed for windowing operation. Various windowing functions have been compared thoroughly [87] with different trade-offs between the main lobe width and the side lobe suppression. The optimal windowing function is outside the scope of this paper, and a raised-cosine (RC) window is utilized due to its low computational complexity and widespread use in the literature [15, 88, 89]. The RC window function [88] is formulated by the following equation:

$$g[n] = \begin{cases} \frac{1}{2} + \frac{1}{2} \cos\left(\pi + \frac{\pi n}{\alpha N_T}\right) & 0 \leq n \leq \alpha N_T \\ 1 & \alpha N_T \leq n \leq N_T \\ \frac{1}{2} + \frac{1}{2} \cos\left(\pi - \frac{\pi n}{\alpha N_T}\right) & N_T \leq n \leq (\alpha + 1) N_T, \end{cases} \quad (2.1)$$

where α is the roll-off factor ($0 \leq \alpha \leq 1$) and N_T denotes the symbol length. The roll-off factor (α) handles the taper duration of the RC window function. As α increases, the INI decreases with the cost of increased redundancy. The transmitter windowing operation is shown in Fig. 2.1. Initially, the guard duration is increased with an additional cyclic prefix (CP) and a newly added cyclic suffix (CS). Afterward, the window function is applied to the extended symbol. The transition parts (i.e., ramp-ups and ramp-downs) of adjacent symbols are overlapped to reduce the time-domain overhead emerging from the windowing operation.

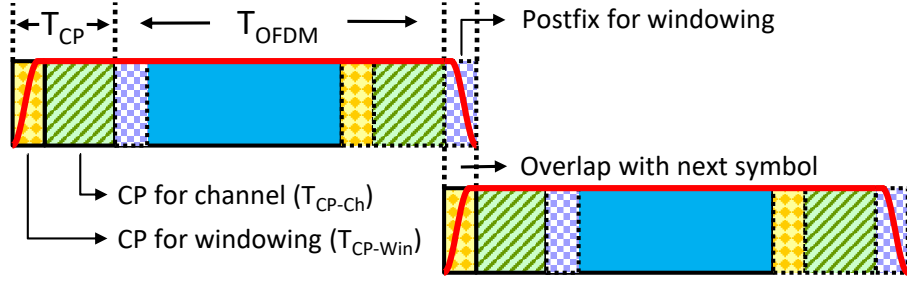


Figure 2.1: Transmitter windowing operation and guard duration allocation.

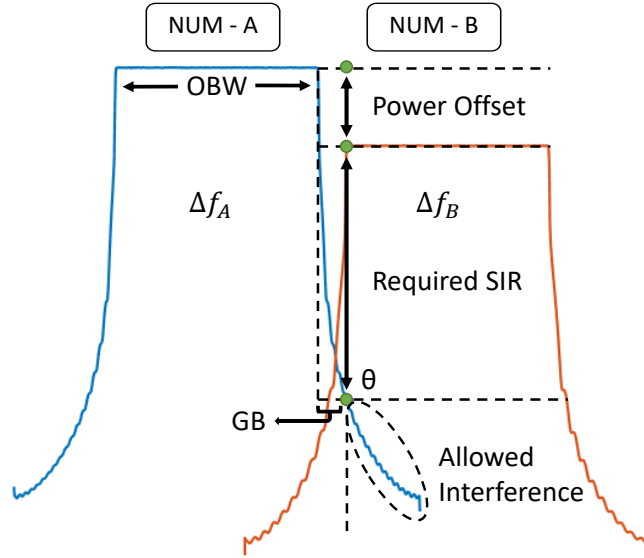


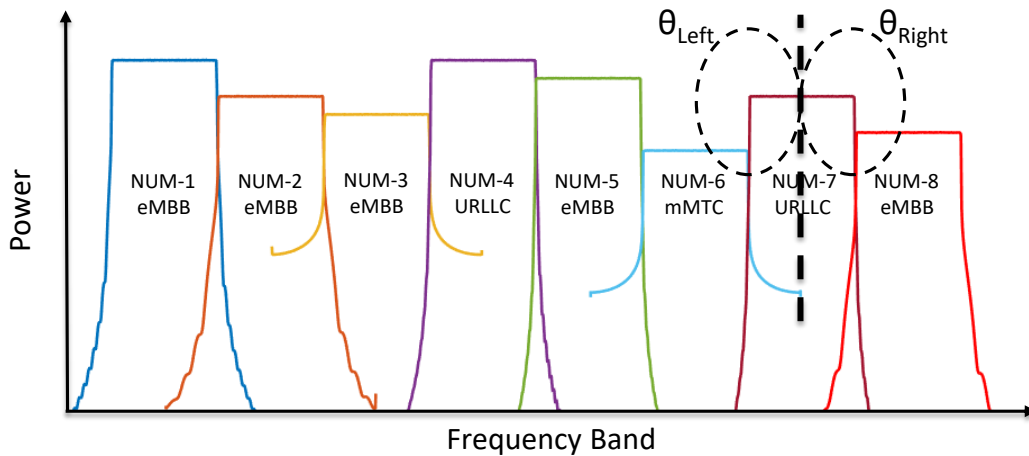
Figure 2.2: Guard band allocation between two numerologies considering the allowed interference level (θ) in the adjacent band.

Usually, the windowing operation is not enough to manage the inter-numerology interference (INI), and non-negligible guard bands are still required. However, the total amount of guard band (GB) or the length of guard duration (GD) which is needed for windowing operation depends on the subcarrier spacing of the interference source, the required signal to interference ratio (SIR) level of the numerology in its adjacent bands, and the power offset (PO) between them. The adaptive guard concept is represented with two numerologies in Fig. 2.2 and can be generalized to multiple numerologies by considering one pair at a time. The threshold for allowed interference level on the adjacent band is represented with θ , and it is expressed as follows:

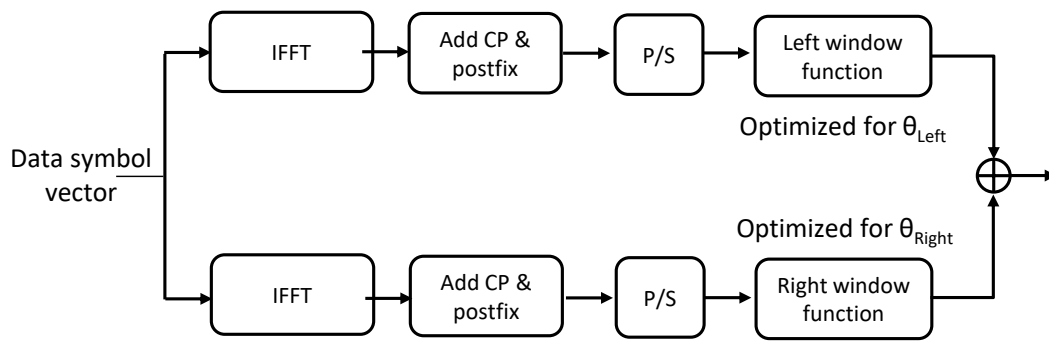
$$\theta_{\Delta f,i} = P_i - P_j + S_j, \quad (2.2)$$

where P_i represents the in-band power of the interference source, S_j denotes the required SIR in the adjacent band to achieve a given target bit error rate considering device complexity for processing, and Δf indicates the subcarrier spacing of the interference source. It should be noted that the different use case requirements and device capabilities are reflected in the required SIR parameter, power level, and subcarrier spacing. Also, $\theta_{\Delta f}$ implies an adaptive brick-wall type spectral mask for a simple evaluation in this study. However, it is possible to extend it to more complicated mask structures along with the adjacent channel leakage ratio (ACLR) threshold [90]. The guards in both time and frequency domains are utilized regarding $\theta_{\Delta f}$ to achieve the desired SIR level of the numerology on the adjacent band. Throughout the numerical evaluations in this study, GD (i.e., T_{CP-win}) and GB are adaptive, and these guards are optimized in Section 2.3. Also, a multi-window operation [91] [92] can be performed in case of an asymmetric interference scenario to manage each side of the spectrum independently considering θ_{Left} and θ_{Right} as shown in Fig. 2.3. The total CP length must be kept the same for synchronicity when a multi-window operation is performed, and the extra CP duration is reserved to solve possible time-domain issues. The remaining parameters of the windowed-OFDM (W-OFDM) system are listed in Table 2.1.

The potential of adaptive guards is increased further, along with the utilization of INI-based scheduling algorithm. Consider frequency domain multiplexed M asynchronous numerologies as shown in Fig. 2.4. Different channel conditions, use cases, and system scenarios result in a change in subcarrier spacing, power level, and SIR requirement of the numerologies as mentioned in Section 2.1. The optimal numerology assignment is beyond the scope of this study, and the reader is referred to [93] for more details on this topic. In this article, the spectral efficiency is optimized while ensuring the required SIR levels for a given numerology set. The power level and SIR requirement of each numerology are generated randomly in such a way that θ changes from 0 dB to 60 dB. Also, Δf gets discrete values of $\{15, 30\}$ kHz and $\{60, 120\}$ kHz with a uniform probability distribution in the frequency range-1 (FR1, a.k.a. sub-6 GHz bands) and frequency range-2 (FR2, a.k.a. millimeter-wave bands) [2], respectively. Assuming that the base station obtains all these



(a)



(b)

Figure 2.3: (a) Asymmetric interference scenario in a mixed numerology network; (b) Block diagram of the multi-window operation.

Table 2.1: Simulation parameters.

Parameter	Value			
Subcarrier Spacing (kHz)	15	30	60	120
T_{OFDM} (μs)	66.7	33.3	16.7	8.3
$T_{\text{CP-channel}}$ (μs)	4.68	2.34	1.17	0.59
FFT Size	2048			
Number of Active Subcarriers	1024			
$\text{CP}_{\text{channel}}$ Size	144			
# OFDM Symbols	300			
Window Type	Multi-window			
Window Function	Raised Cosine			

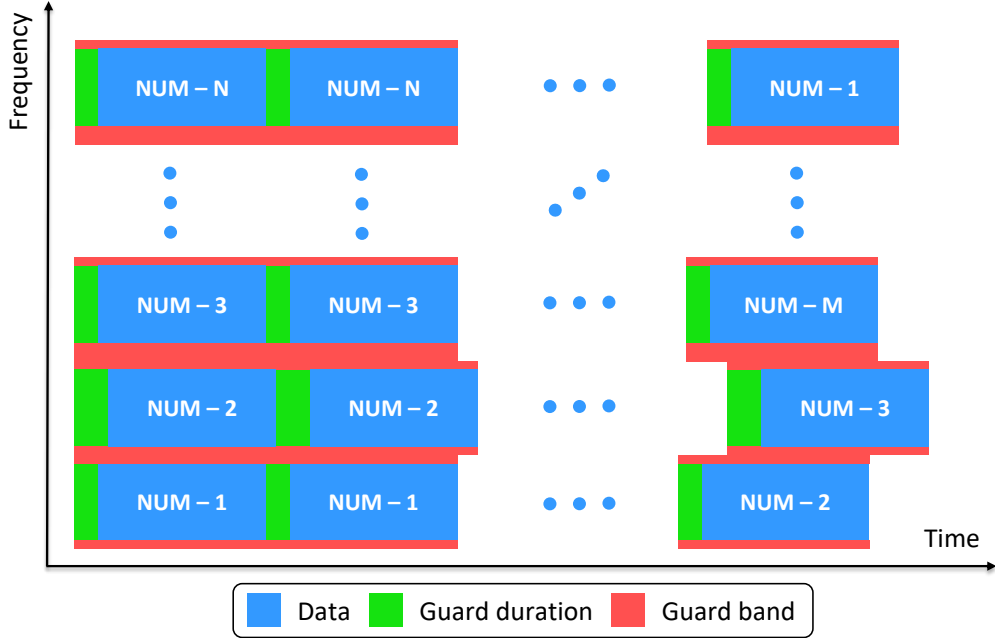


Figure 2.4: Frequency domain multiplexed numerologies.

necessary information perfectly and there are M available subbands, it allocates the numerologies to the available subbands out of $M!$ possible arrangements intelligently considering the INI.

2.3 Optimization of the Adaptive Guards

Assuming that the data at each subcarrier are statistically independent and mutually orthogonal, the power spectral density (PSD) of an OFDM signal is obtained by summing the power spectra of individual subcarriers, and it is expressed by the following equation [94–96]:

$$P_f(x) = \frac{\sigma_d^2}{T} \sum_k |G[(f - k\Delta f)T]|^2, \quad (2.3)$$

where σ_d^2 represents the variance of the data symbols, T denotes the symbol duration, k stands for the subcarrier index, Δf shows the subcarrier spacing, and G is the frequency domain representation of pulse shaping window. An OFDM signal is well localized in the time domain with a rectangular pulse shape, which is equivalent to a sinc shape in the frequency domain. The sidelobes of the sines result in a serious INI issue, and they should be reduced to prevent interference. Particularly, the

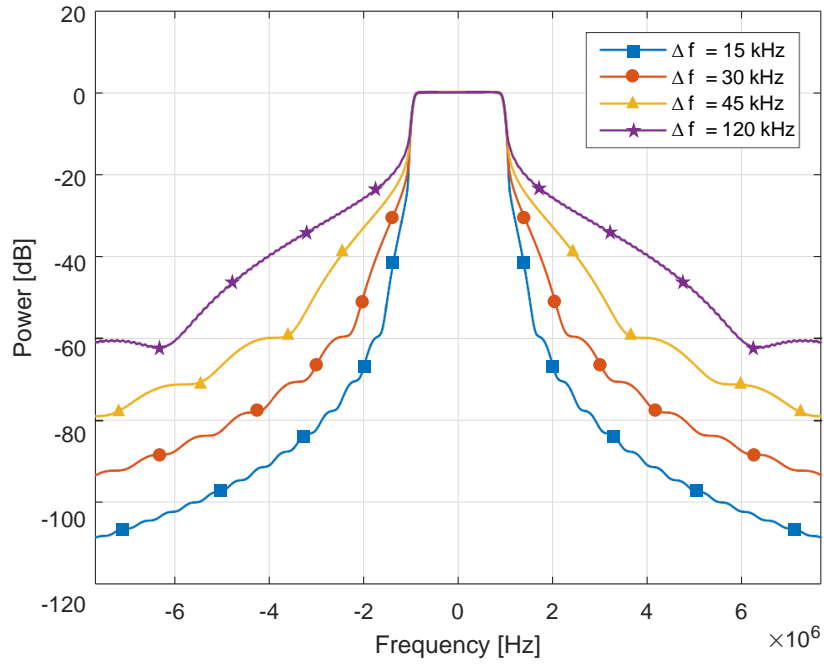
frequency domain localization is crucial for asynchronous transmissions across adjacent subbands and peaceful coexistence with other numerologies in the network. The sidelobes of RC function is controlled with the parameter α as shown in the following relationship [97]:

$$G = \frac{\sin(\pi f T)}{\pi f T} \frac{\cos(\pi \alpha f T)}{1 - (2\alpha f T)^2} \quad 0 \leq \alpha \leq 1. \quad (2.4)$$

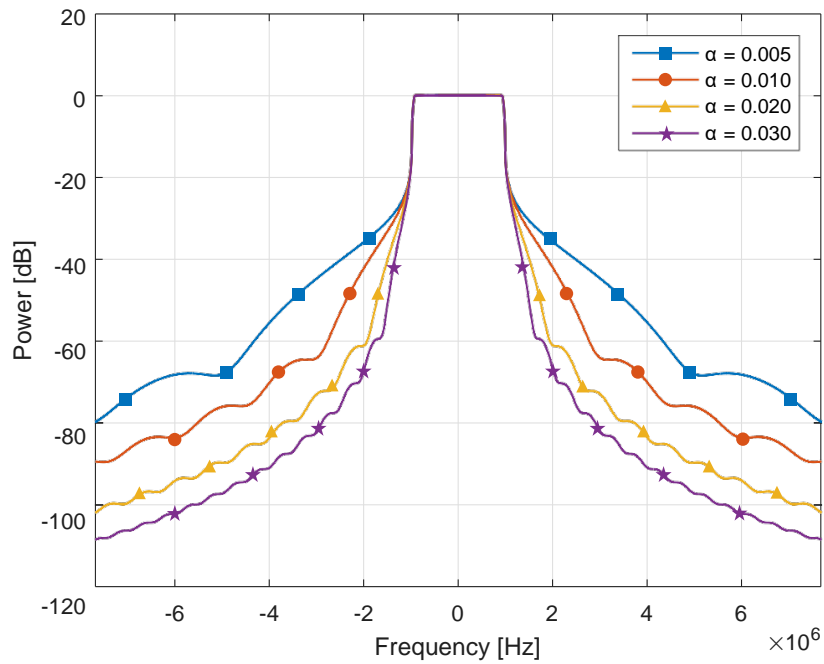
Equation 2.3 and equation 2.4 show that the parameters T (i.e., $\Delta f = 1/T$) and α have an important effect on the PSD of W-OFDM. Figure 2.5 illustrates the effect of these parameters on the PSD separately. It should be noted that a significant contribution to unwanted emissions in the passband comes from RF front-end impairments as well, including power amplifier nonlinearities. However, these impairments heavily depend on many implementation-dependent factors, such as the application type, operational frequency, bandwidth of the signal, and complexity of the device, and are not considered in this study.

In a mixed numerology network, the INI can be managed by windowing operation and allocating guard band between adjacent numerologies as described in Section 2.2. Since the windowing operation reduces the unwanted emissions with a cost of extra guard duration, the INI management procedure boil downs to the adaptive utilization of guard duration (GD) and guard band (GB) to achieve a desired interference threshold (θ). Figure 2.6 demonstrates the required GB and GD amounts for selected θ values considering a W-OFDM signal with $\Delta f = 15 \text{ kHz}$. Each α value in the figure represents a GD allocation to carry out windowing operation, and a GB allocation to handle the rest of interference for a given θ .

A tremendous time-frequency resource is required to deal with the INI issue only with GB or GD allocation. Hence, GB and GD have to be jointly optimized in order to improve the spectral efficiency, which is measured as the information rate that can be transmitted over a given bandwidth. This hyper-parameter optimization has been carried out by a grid search method through a manually designated subset of the hyper-parameter space [98]. The spectral efficiency (η) is proportional to the multiplication of efficiencies in the time and frequency domains, which are calculated as follows:



(a)



(b)

Figure 2.5: PSD of W-OFDM: (a) The effect of Δf (α is fixed to 0.03); (b) The effect of α (Δf is fixed to 15 kHz).

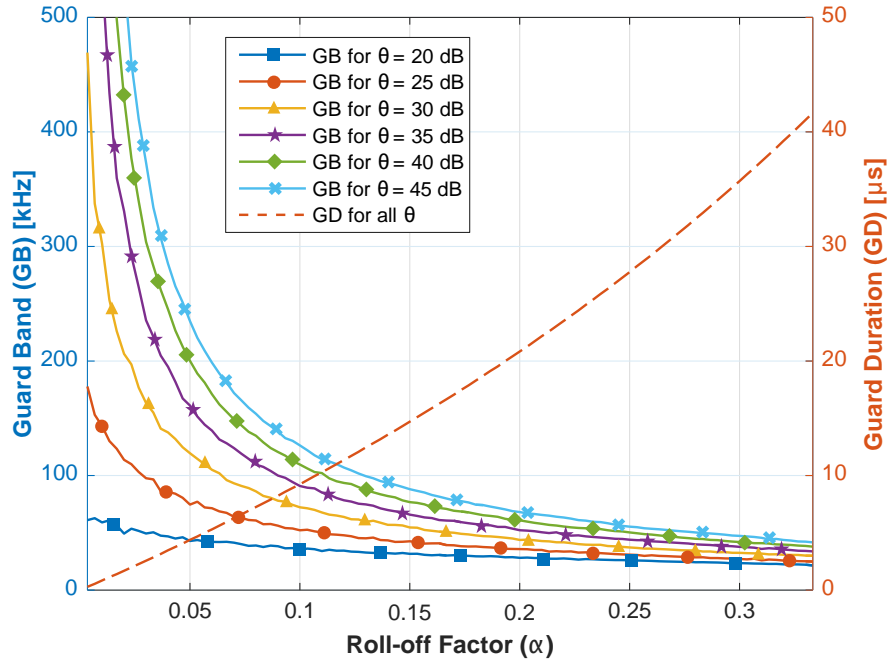


Figure 2.6: Required GB and GD pairs to achieve selected θ levels for a W-OFDM signal with $\Delta f = 15 \text{ kHz}$.

$$\eta_{time} = \frac{T_{OFDM}}{T_{OFDM} + T_{CP-Ch} + T_{CP-Win}}, \quad (2.5)$$

$$\eta_{freq} = \frac{OBW}{OBW + (GB \times 2)}. \quad (2.6)$$

Considering T_{OFDM} , T_{CP-Ch} , and occupied bandwidth (OBW) are fixed parameters for a given Δf , the degrees of freedom that can be selected independently becomes only GB and GD (i.e., T_{CP-Win}). The optimization problem that looks for the optimal GB and GD pair can be defined as follows:

$$(GB, GD) = \arg \max_{GB, GD} (\eta_{time} \times \eta_{freq}), \quad (2.7)$$

$$\text{subject to: } P_i - P_j + S_j \leq \theta_{\Delta f, i}. \quad (2.8)$$

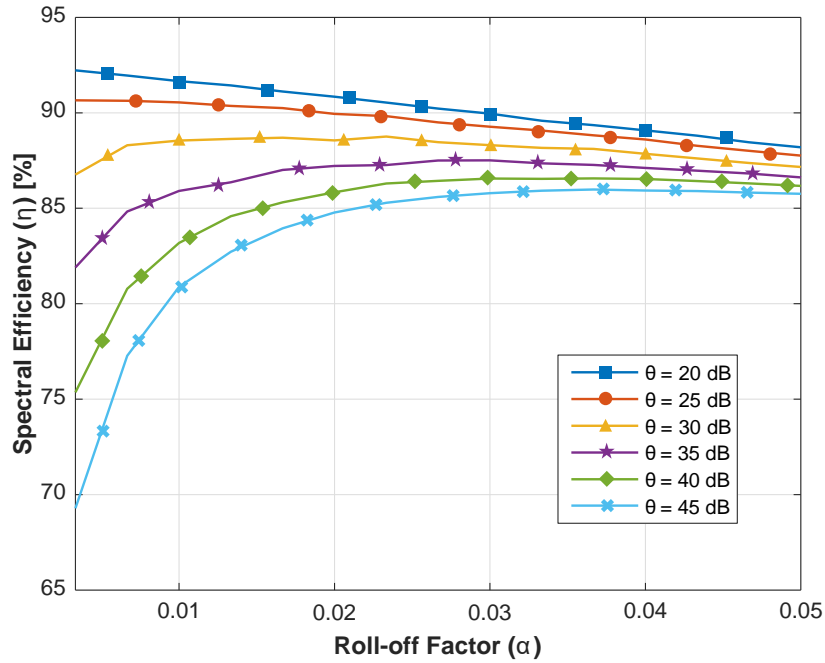


Figure 2.7: Spectral efficiency (η) of the GB and GD pairs that achieves selected $\theta_{\Delta f=15\text{kHz}}$ (Please note that each α corresponds to a GB-GD pair).

The spectral efficiencies for selected θ values are shown in Fig. 2.7. Each α value in the figure is equivalent to a GB-GD pair for a given θ , and the peak value of each curve determines the optimal pair. These optimal pairs are summarized in Table 2.2 along with the related parameters for various Δf . The results reveal that the need for windowing diminishes as θ decreases, and accordingly, the desired interference level can be accomplished only with a few guard subcarriers. Also, the spectral efficiency increases with the decrease in θ . The change in required guards clearly confirms that the adaptive guard design enhances the spectral efficiency significantly compared to designing the mixed numerology system considering the worst case scenario (e.g., $\eta_{\theta=45\text{dB}} = 85.98\%$ whereas $\eta_{\theta=20\text{dB}} = 92.53\%$). Despite the fact that the computational complexity increases compared to traditional OFDM-based systems, the computation of the optimal GB-GD pairs is an offline action that needs a one-time calculation. Therefore, a lookup table procedure can be used to decrease complexity.

Table 2.2: Optimal guard duration (GD) and guard band (GB) pairs for selected θ .

θ [dB]	$\Delta f = 15$ kHz				$\Delta f = 30$ kHz				$\Delta f = 60$ kHz				$\Delta f = 120$ kHz			
	α	GD [μ s]	GB [kHz]	η [%]	α	GD [μ s]	GB [kHz]	η [%]	α	GD [μ s]	GB [kHz]	η [%]	α	GD [μ s]	GB [kHz]	η [%]
20	0.0000	0.00	74.88	92.53	0.0000	0.00	154.44	92.50	0.0000	0.00	249.83	92.68	0.0000	0.00	557.22	92.59
25	0.0033	0.23	210.11	90.65	0.0033	0.11	390.13	90.83	0.0033	0.06	857.94	90.60	0.0033	0.03	1582.9	90.79
30	0.0233	1.69	217.33	88.75	0.0167	0.60	534.34	88.79	0.0167	0.30	1037.3	88.88	0.0167	0.15	2121.9	88.81
35	0.0300	2.21	272.87	87.51	0.0267	0.98	609.44	87.47	0.0300	0.55	1083.9	87.53	0.0267	0.24	2426.1	87.49
40	0.0367	2.70	306.71	86.57	0.0300	1.11	715.19	86.59	0.0333	0.62	1318.6	86.58	0.0367	0.34	2449.7	86.57
45	0.0367	2.70	360.58	85.98	0.0367	1.35	722.70	85.98	0.0367	0.68	1434.8	86.01	0.0367	0.34	2886.1	85.98

2.4 Inter-numerology Interference (INI)-based Scheduling

The total guard amount is reduced with the joint optimization of the guard band (GB) and guard duration (GD) for a given interference threshold ($\theta_{\Delta f}$) in Section 2.3. The optimization results show that the spectral efficiency (η) decreases as θ increases. Also, the numerologies with larger subcarrier spacing (Δf) require more guards, and they lead to lower η values in a mixed numerology network. Since θ depends on the numerologies operating in the adjacent bands, the potential of adaptive guards can be enhanced further along with the utilization of an interference-based scheduling algorithm.

The proposed scheduling algorithm groups the numerologies and allocates them to the available subbands considering the inter-numerology interference (INI). The numerologies with similar subcarrier spacing, power level, and SIR requirements are arranged together in order to decrease the mean θ in the network. Consequently, the need for guards reduces, and the spectral efficiency improves. The steps of the proposed INI-based scheduling algorithm are listed as follows:

1. Sort the numerologies regarding their Δf value in an ascending/descending order.
2. Calculate the similarity metric for all numerologies as $\beta_j = SIR_j - P_j$.
3. Sort β in an ascending/descending order for the numerologies with the same Δf .
4. If β value repeats, sort based on power in the adjacent band.

Table 2.3: Key parameters of randomly scheduled numerologies for adaptive guard allocation.

Band	1	2	3	4	5	6	7	8
Numerology ID	1	2	3	4	5	6	7	8
Δf [kHz]	30	15	15	30	15	15	30	15
Req. SIR [dB]	20	20	20	25	20	25	35	20
Rx Power [dBm]	0	-10	-15	0	-5	-25	-10	-20
Power Offset [dB]	10	-10, 5	-5, -15	15, 5	-5, 20	-20, -15	15, 10	-10
Intf. Thr. (θ_A, θ_B) [dB]	30	10, 25	15, 10	35, 25	20, 45	0, 20	40, 30	25

Table 2.4: Key parameters of INI-based scheduled numerologies for adaptive guard allocation.

Band	1	2	3	4	5	6	7	8
Numerology ID	7	4	1	5	2	3	8	6
Δf [kHz]	30	30	30	15	15	15	15	15
Req. SIR [dB]	35	25	20	20	20	20	20	25
Rx Power [dBm]	-10	0	0	-5	-10	-15	-20	-25
Power Offset [dB]	-10	10, 0	0, 5	-5, 5	-5, 5	-5, 5	-5, 5	-5
Intf. Thr. (θ_A, θ_B) [dB]	15	45, 20	25, 25	15, 25	15, 25	15, 25	15, 30	15

5. Check P on both sides of the available band. If P is the same with the numerology in its adjacent band, allocate the numerology with a higher SIR requirement to the edge.

The performance of the INI-based scheduling algorithm is evaluated numerically, and its performance is compared with the performance of a random scheduling strategy. The allocation probability to any given subband is $1/M$ for all numerologies (i.e., uniform probability distribution) in the random scheduling strategy. Eight numerologies (i.e., $M = 8$) are considered in Monte Carlo simulations, and a random parameter set is assigned to numerologies for each realization, as discussed in Section 2.2. The key parameters of an exemplary realization, such as subcarrier spacing, power level, and SIR requirement, are listed in Tables 2.3 and 2.4. The random scheduling strategy and the INI-based scheduling strategy are implemented for the same parameter set, as illustrated in Fig. 2.3 and Fig. 2.8, respectively. Although the guards in both time and frequency domains are jointly optimized in the PHY layer for both cases, they utilize different scheduling algorithms in the MAC layer. As a result, any performance difference can be attributed to the

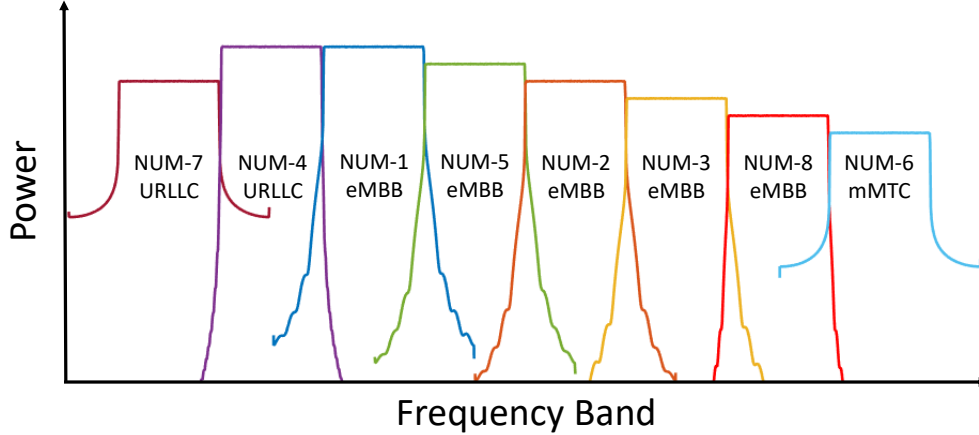


Figure 2.8: INI-based scheduled numerologies with various use cases.

proposed scheduling algorithm. Furthermore, a fixed guard allocation strategy is implemented with the random scheduling method to demonstrate the effectiveness of the proposed adaptive guard allocation. The guards are assigned considering the worst-case scenario (i.e., highest $\theta_{\Delta f}$) in the fixed guard allocation strategy.

The system performance is evaluated in terms of spectral efficiency (η) and the average evaluation results (out of 100 independent realizations) for various guard allocation and scheduling strategies, which are the fixed guard allocation with the random scheduling, the adaptive guard allocation with the random scheduling, and the adaptive guard allocation with the INI-based scheduling, are presented in Table 2.5. The results demonstrate that the GD and GB amounts are reduced by 43% and 34%, respectively when the fixed guards are replaced with the adaptive guards in the frequency range-1 (FR1) scenario. Also, the GD and GB amounts are reduced further by 10% and 27%, respectively, when the proposed INI-based scheduling strategy is implemented instead of the random scheduling strategy. It is worth to note that η is lower in the frequency range-2 (FR2) case since more guards are required for the numerologies with higher Δf values due to their higher unwanted emissions. Although it can be compensated with an increased number of subcarriers (FR2 is suitable for wider bands), it is kept as fixed to 256 for a fair comparison with the FR1 case in the numerical evaluations.

Table 2.5: Spectral efficiency comparison for various guard allocation and scheduling strategies.

Scenario	Total Guard Duration [μ s]		Total Guard Band [kHz]		Spectral Efficiency [%]	
	FR1	FR2	FR1	FR2	FR1	FR2
Fixed Guards & Random Scheduling	16.08	4.12	5018.4	1927.4	81.22	77.35
Adaptive Guards & Random Scheduling	9.09	2.24	3335.7	1310.2	85.32	82.19
Adaptive Guards & INI-based Scheduling	8.15	2.06	2428.8	971.9	87.10	84.65

The proposed INI-based scheduling strategy is particularly important when there is a severe power imbalance between the numerologies (i.e., a set of synchronous UEs). The current mobile networks adopted a power control mechanism in the uplink to manage interference between neighboring bands. However, this solution restricts the UEs with better channel conditions to deploy higher-order modulations and decreases the spectral efficiency. The proposed scheduling technique can relax the power control mechanism and improve throughput. Also, it should be noted that the channel-based scheduling can be performed to orthogonal/synchronous UEs within a given numerology, whereas the INI-based scheduling can be performed to non-orthogonal/asynchronous numerologies for reduced complexity.

2.5 Conclusions

A novel inter-numerology interference (INI) management technique with a cross-layer approach is proposed in this study. The adaptive guards in both time and frequency domains are utilized along with a multi-window operation in the PHY layer and jointly optimized considering the use case, subcarrier spacing, and power offset between the numerologies. Since the allowed interference level depends on the numerologies operating in the adjacent bands, the potential of adaptive guards is further increased and exploited with a MAC layer scheduling technique. The proposed INI-based scheduling algorithm decreases the need for guards by allocating the numerologies to the available bands, considering their subcarrier spacing, power level, and SIR

requirements. It is demonstrated that the optimized guard allocation and INI-based scheduling algorithm improves the spectral efficiency significantly while taking into account the different use case requirements and device capabilities.

The results show that the precise design that accommodates such flexibility reduces the guards and improves the performance of mixed numerology systems. The INI management technique is proposed on the transmitter side in the PHY layer along with a MAC layer scheduling technique in this study. The guards are designed in such a way that it guarantees the required SIR levels for each numerology in the network. Therefore, the theoretical upper bounds on the bit error rate can be obtained in a straightforward way using the channel capacity equation [99]. However, it will be extended to the receiver side as well for enhanced performance in the future. Also, a practical receiver structure enables performance evaluation under various channel conditions and impairments. Furthermore, the CP length for the multipath channel is assumed fixed and sufficient for the delay spread. Nevertheless, some ISI can be allowed in order to suppress INI further for a fixed guard duration, and the ISI vs. INI trade-off is worth investigating. Last but not least, the proposed INI management technique with a cross-layer approach can be applied to other spectrally enhanced OFDM systems [100–103] as well by optimizing the waveform parameters and guards along with a proper scheduling mechanism. For example, a recent publication [79] demonstrated the joint optimization of the filter parameters and guard band for filtered-OFDM (f-OFDM) only in the PHY layer.

The next-generation wireless communication technologies are evolving towards increased flexibility in various aspects. Enhanced flexibility is the key design consideration, especially to be able to serve diverse requirements. Hence, the adaptive guard utilization must be a part of the future communication systems.

Chapter 3: Anatomical Region-Specific *In Vivo* Channel Characterization

3.1 Introduction

Chronic diseases and conditions such as diabetes, obesity, heart disease, and stroke are the leading causes of death and disabilities in the United States³. Treating people with these illnesses accounts for 86%⁴ of the national health expenditure which is expected to be almost double in the next ten years⁵. However, these are the most preventable and manageable problems among all health issues by committing to a healthier lifestyle. Continuous health monitoring helps to achieve this goal by assisting people to engage in their healthcare and also allows physicians to perform more reliable analysis by providing the data collected over a large period of time. In addition, exploitation of this *big data* will replace the traditional “one-size-fits-all” model with more personalized healthcare in the near future. Furthermore, noninvasive surgery and remote treatment are expected to lower the risk of infection, reduce hospitalization time and accelerate recovery processes. All these demanding requirements for an effective service quality in healthcare awakened a general interest in wireless body area networks (WBANs) research [6,31,32,37,104–109]. One component of such advanced technologies is represented by wireless *in vivo* sensors and actuators, e.g., pacemakers, internal drug delivery devices, nerve stimulators, and wireless capsules as shown in Fig.3.1. *In vivo* medical devices offer a cost efficient and scalable solution along with the integration of wearable devices and help to achieve the vision of advanced pervasive healthcare, anytime and anywhere [6]. Besides healthcare, the use of *in vivo*-WBANs is also envisioned for many other applications such as military, athletic training, physical education, entertainment, safeguarding, and consumer electronics [5,110].

³This chapter was published in [8]. Permission is included in Appendix A.

⁴<http://www.cdc.gov/chronicdisease>

⁵<https://www.cms.gov>

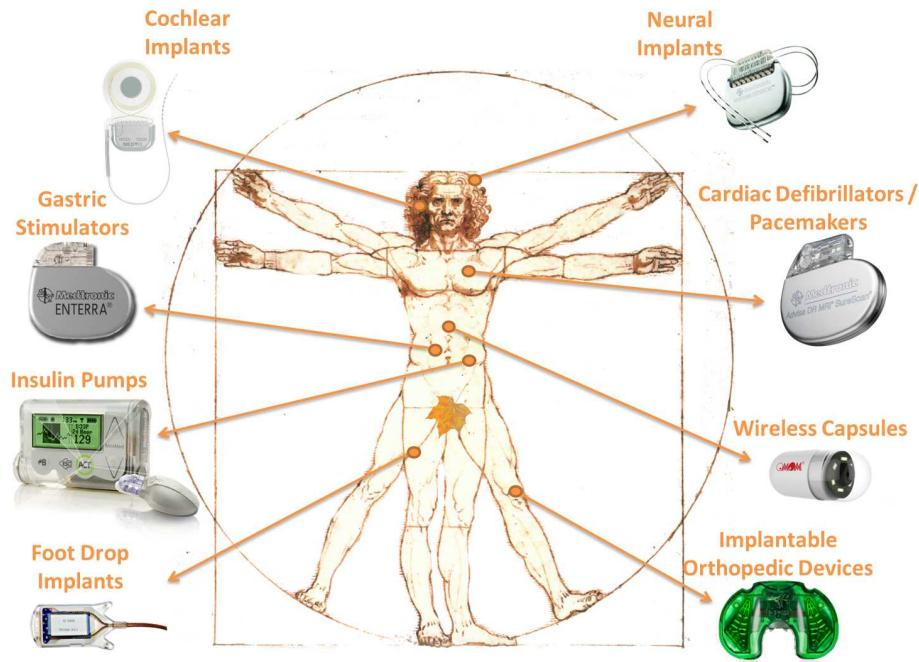


Figure 3.1: *In vivo*-WBAN devices for various applications.

In vivo-WBANs and their associated technologies will shape the future of healthcare considering all the potentials and the critical role of these applications. To fully exploit the use of them for practical applications, it is necessary to obtain accurate channel models that are mandatory to build reliable, efficient, and high-performance communication systems. These models are required not only to optimize the quality of service metrics such as high data rate, low bit-error rate, and latency but also to ensure the safety of biological tissues by careful link budget evaluations. Although, on-body wireless communication channel characteristics have been thoroughly investigated [104, 111], the studies on *in vivo* wireless communication channels (implant-to-implant and implant-to-external device links) are limited. The *in vivo* channel exhibits different characteristics than those of the more familiar wireless cellular and Wi-Fi environments since the electromagnetic (EM) wave propagates through a very lossy environment inside the body, and dominant scatterers are present in the near-field region of the antenna.

The IEEE 802.15.6 standard [112] was released in 2012 to regulate short-range wireless communications inside or in the vicinity of the human body. According to this standard, *in vivo*-WBAN devices operate in the medical device radio communications service (MedRadio)

which uses discrete bands within the 401–457 MHz spectrum including the previous specification called medical implant communication service (MICS) band. Despite the fact that MedRadio bands provide satisfying propagation characteristics inside the human body [42], they suffer from lower bandwidths and larger antenna size issues compared to the antennas designed to operate at higher frequencies. Therefore, other frequency bands, such as industrial, scientific, medical (ISM) and ultra-wide band (UWB) communications bands should also be considered in the upcoming standards for *in vivo* wireless communications. It is also known that EM wave propagation inside the human body is strongly related to the location of the antenna [37, 42] and hence, the *in vivo* channel should be investigated for a specific anatomical part. For example, the gastrointestinal tract has been studied for wireless capsule endoscopy applications [52], while the heart area has been investigated for implantable cardioverter defibrillators and pacemakers [113]. Although many *in vivo* path loss (PL) formulas were reported in the literature [33, 105–108, 113, 114], they do not provide location specific PL model parameters to carry out accurate link budget calculations. Moreover, detailed human body models are crucial in order to investigate the *in vivo* wireless communication channel. Various phantoms have been designed to simulate the dielectric properties of the tissues for numerical and experimental investigation. The validation of numerical studies with real experimental measurements is required, however performing experiments on a living human is strictly regulated. Therefore, physical phantoms [33, 37, 105] or anesthetized animals [106, 107] are often used for experimental investigations.

This chapter presents a numerical and experimental characterization of the *in vivo* wireless communication channel for male torso considering various anatomical regions. The location dependent characteristics of the *in vivo* channel are investigated by performing extensive simulations at 915 MHz and 2.4 GHz using HFSS[®]. A statistical PL formula is introduced, and anatomical region-specific parameters are provided. The multipath propagation characteristics of the *in vivo* channel are examined by investigating the polarization and analyzing the delay spread, which is of particular importance for broadband applications. In addition to the thorough simulation studies, experiments are conducted on a human cadaver, and the results are compared with the numerical

studies. The preliminary results were presented in [53] and [38]. To the best of authors' knowledge, this is the first study that investigates the *in vivo* wireless channel for various anatomical regions both numerically and experimentally on a human cadaver. The final research outcomes are published in [8].

The rest of the chapter is organized as follows. Section 3.2 describes the simulation/ experimental setup and explains the measurement methodology in detail. Section 3.3 presents the *in vivo* channel characterization based on the numerical and experimental investigation. A statistical PL formula is provided along with the anatomical region-specific parameters, and multipath propagation characteristics are examined thoroughly. Finally, Section 3.4 summarizes the contributions and concludes Chapter 3.

3.2 Simulation and Measurement Settings

3.2.1 Simulation Setup

Analytical methods are viewed as infeasible and require extreme simplifications [32, 34]. Therefore, numerical methods, which provide less complex and appropriate approximations to Maxwell's equations, are preferred for characterizing the *in vivo* wireless communication channel. In this study, we used ANSYS HFSS[®] 15.0 [115], which is a full-wave EM field simulator based on the Finite Element Method (FEM). ANSYS also provides a detailed male human body model, and it includes frequency dependent dielectric properties of over 300 parts (bones, tissues and organs) with 2 mm resolution. This extensive simulation work was beyond the capability of personal computers and advanced computing resources at the University of South Florida (USF) were used to solve such large EM problems. Research Computing at USF hosts a computer cluster which currently consists of approximately 500 nodes with nearly 7200 processors cores and 24TB of memory in total.

The simulations were designed considering an implant to an external device (in-body to on-body) communications scenario in the male torso with a similar measurement setup in [53]. Rather than using the whole body, the torso area was segmented into four sectors considering the

major internal organs: heart, stomach, kidneys, and intestine as shown in Fig. 3.2a. In each region, simulations were performed by rotating receiver (*ex vivo*) and transmitter (*in vivo*) antennas together around the body with 22.5° angle increments (Fig. 3.2b). The *ex vivo* antenna was placed 5 cm away from the body surface and the *in vivo* antenna was placed at ten different depths (from 10 mm to 100 mm) inside the body for each *ex vivo* antenna location. In addition, antennas were placed in the same orientation to avoid polarization losses.

The received power is expressed using the Friss equation (Eq. 3.1) for free space links [116]:

$$P_r = P_t G_t \left(1 - |S_{11}|^2\right) G_r \left(1 - |S_{22}|^2\right) \left(\frac{\lambda}{4\pi R}\right)^2 \quad (3.1)$$

where P_t/P_r represents transmitted/received powers, G_t/G_r denotes the gain of the transmitter/receiver antenna, λ stands for the free space wavelength, R is the distance between transmitter and receiver antennas and $|S_{11}|$, $|S_{22}|$ are the reflection coefficients of transmitter/receiver antennas. Unlike free-space communications, *in vivo* antennas are often considered to be an integral part of the channel [32] (i.e., the gain cannot be separated from the channel) and hence, they need to be designed carefully. However, omnidirectional dipole antennas at 915 MHz and 2.4 GHz were deployed in our simulations for simplicity. The dipole antenna length is proportional to the wavelength, which varies with respect to both frequency and permittivity. Higher frequencies compared to the MedRadio bands provide smaller antenna sizes, hence, they could be implanted conveniently. In addition, the antennas were optimized inside the body with respect to the average torso permittivity for each frequency towards obtaining maximum power delivery. Although the antennas presented a good return loss (i.e., less than -7dB), they were perfectly matched by compensating the $\left(1 - |S_{11}|^2\right)$ and $\left(1 - |S_{22}|^2\right)$ factors to yield a fair comparison for PL analysis. Also, the mesh size was set to be less than $\lambda/5$ in this study.

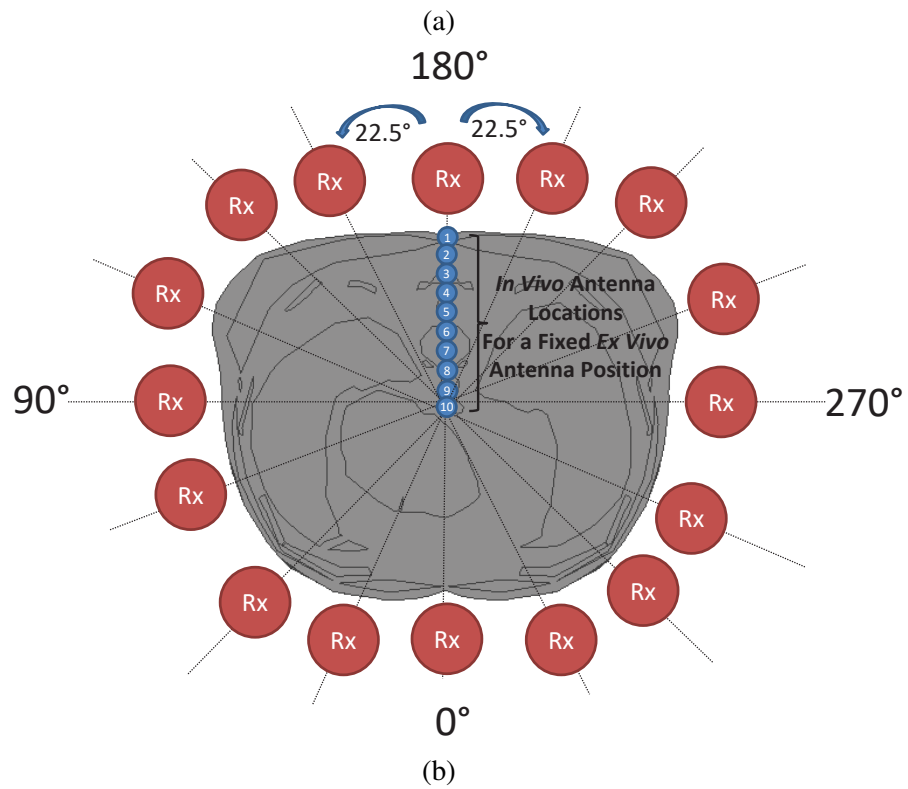
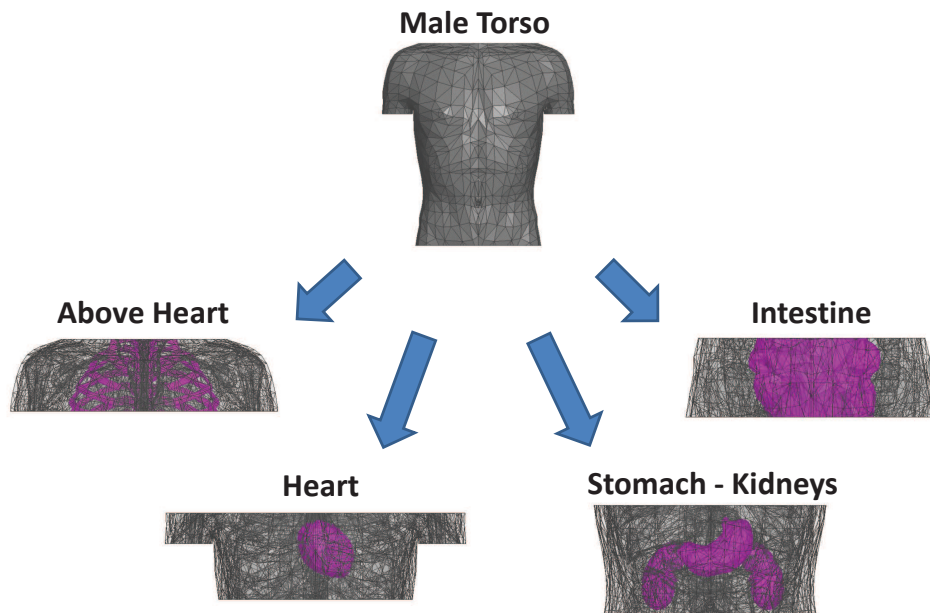


Figure 3.2: (a) Investigated anatomical regions; (b) *In vivo* and *ex vivo* antenna locations in simulations.

3.2.2 Experimental Setup

The numerical investigation was validated by conducting experiments on a human cadaver in a laboratory environment. Istanbul Medipol University provided the ethical approval and medical assistance in this study. The preliminary results were presented in [38]. Animal organs are used to represent human tissues as suggested in [33, 117, 118] and the decayed human internal organs in this experiment were replaced with internal organs of a sheep. The male torso area was investigated at 915 MHz by measuring the channel frequency response, i.e., $S_{21}(f)$, through a vector network analyzer (VNA). A tapered slot coplanar waveguide (CPW)-fed antenna [119] (*in vivo*) and a dipole antenna (*ex vivo*) were used in our experiments with two coaxial cables each having a length of 2 meters as illustrated in Fig. 3.3. The frequency response of cables was subtracted from the channel measurements by performing a calibration of the VNA. The antennas were wrapped with a biocompatible polyethylene protective layer and sealed tightly in order not to contact the biological tissues directly, which could lead to shortening the antennas. The antennas were tested before the experiment and provided sufficient return loss inside the body during the experiments (i.e., less than -7dB).

The *in vivo* antenna was placed at six different locations (Fig. 3.4) inside the body around the heart, stomach, and intestine by the help of a physician. *In vivo* depth measurements were performed using a digital caliper and the antennas were placed with the same orientation to avoid polarization losses, similar to the simulations. The channel data was captured between the frequencies 905 MHz to 925 MHz and post processed for further analysis in MATLAB[®]. Although the experimental setup did not allow capturing the effects of circulatory and respiratory systems, it provides a more realistic multipath propagation scenario than computer simulations or experiments which are conducted on physical phantoms and anesthetized animals by providing EM wave propagation in an actual human body.



Figure 3.3: Experiment setup for *the in vivo* channel: 1) Vector network analyzer (VNA), 2) human male cadaver, 3) coaxial cables, 4) a novel tapered slot CPW-fed antenna (*in vivo*), 5) insulated dipole antenna (*ex vivo*).

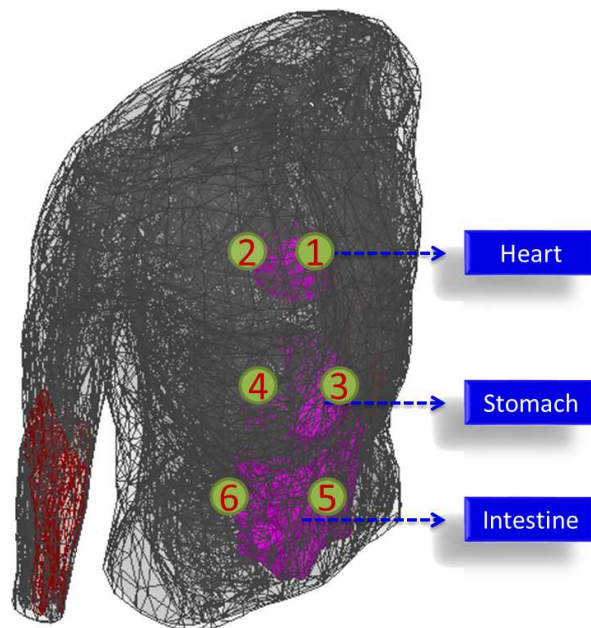


Figure 3.4: Measurement locations on the human cadaver, where odd and even numbers represent top and bottom of the corresponding organs respectively.

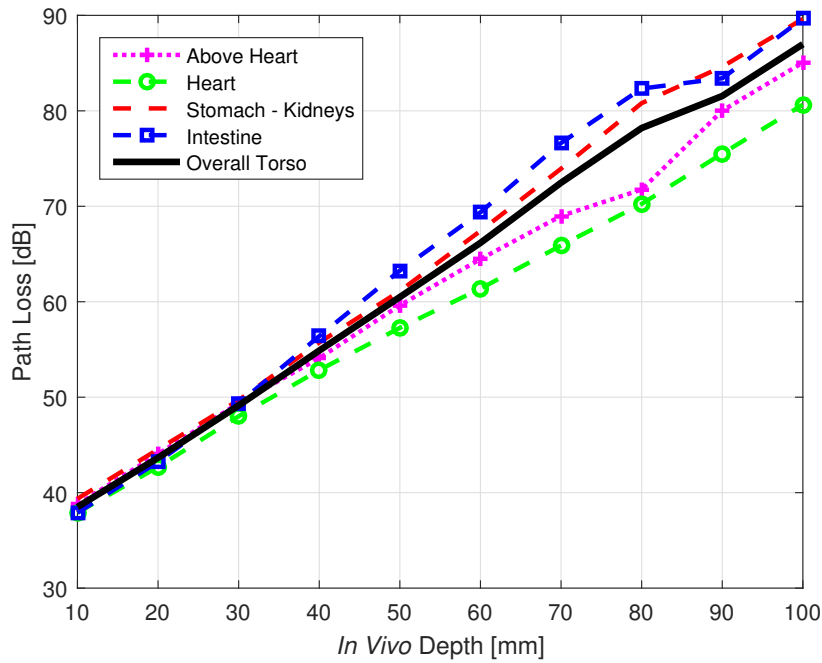


Figure 3.5: Average path loss for four anatomical regions in the simulation environment at 2.4 GHz.

3.3 In Vivo Channel Characterization

3.3.1 Path Loss and Shadowing

The *in vivo* path loss (PL) expresses a measure of the average signal power attenuation inside the body and is calculated as $PL = -\text{mean}\{|S_{21}|\}$ using the channel frequency response, i.e., S_{21} [105, 106]. The location dependent characteristic of the *in vivo* PL was investigated for two ISM bands, i.e., 915 MHz and 2.4 GHz. The EM wave propagates through various organs and tissues regarding different antenna locations, and the PL changes significantly even for equal *in vivo* depths. The location dependent characteristic of the channel is more dominant when the *in vivo* antenna is placed deeper inside the body. Fig. 3.5 presents the mean PL for the investigated four anatomical body regions in the simulation environment. Although the signal power attenuation is similar for near-surface locations, complex body areas such as intestine cause higher PL due to their dense structure beyond 30 mm *in vivo* depth.

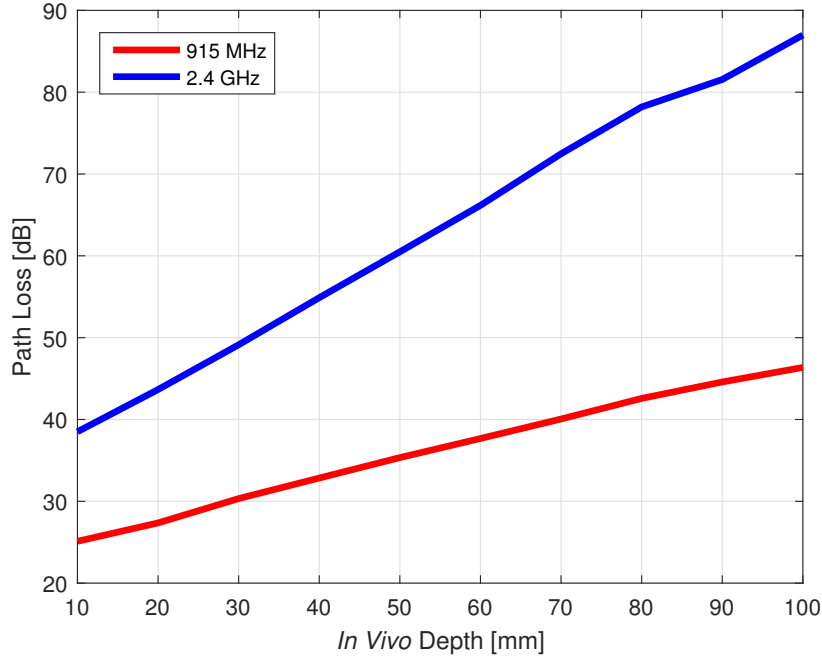


Figure 3.6: Average path loss on torso in the simulation environment at 915 MHz and 2.4 GHz.

Various analytical and statistical PL formulas have been proposed for the *in vivo* channel [6]. Despite the fact that analytical expressions provide intuition about each component of the propagation models, they are not practical for link budget design. According to the final report of the IEEE 802.15.6 standard’s channel modeling subgroup, Friis transmission equation (Eq. 3.1) can be used for *in vivo* scenarios by adding a random variation term [46, 120]. In this work, the *in vivo* PL is modeled statistically as a function of depth by the following equation expressed in dB scale:

$$PL(d) = PL_0 + m(d/d_0) + S \quad (d_0 \leq d) \quad (3.2)$$

where d represents the depth from the body surface in mm, d_0 stands for the reference depth with a value of 10 mm, PL_0 denotes the intercept term in dB, m is the decay rate of the received power and S denotes the random shadowing in dB, which presents a normal distribution for a fixed distance. The power decay rate (m) heavily depends on the environment and is obtained by performing extensive simulations and measurements. Also, the shadowing term (S) depends on the different

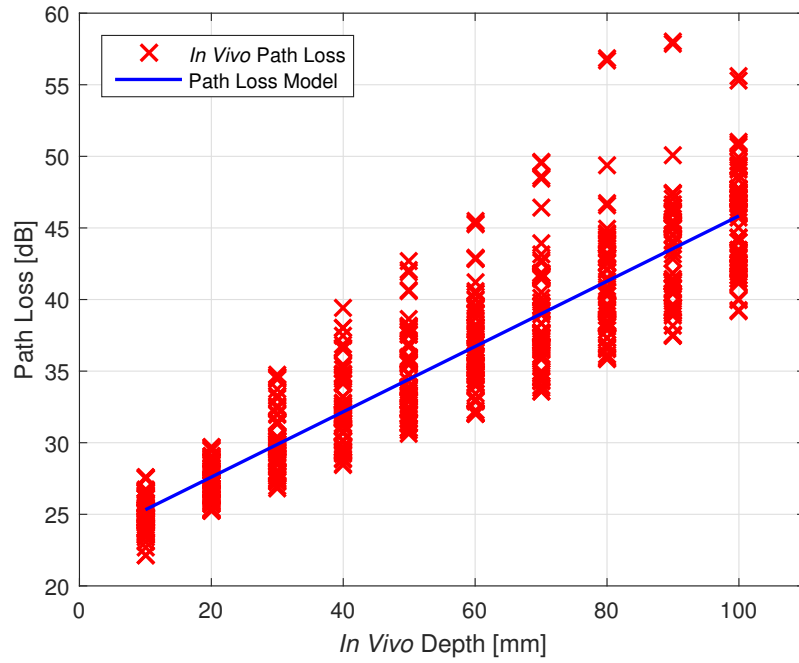
Table 3.1: Variance of shadowing term (S) in dB for each *in vivo* depth.

Depth Frequency	10 mm	20 mm	30 mm	40 mm	50 mm	60 mm	70 mm	80 mm	90 mm	100 mm
915 MHz	1.26	1.29	2.17	2.67	3.01	3.38	3.86	4.22	4.05	3.60
2.4 GHz	1.67	2.03	2.54	3.29	4.47	5.39	6.44	7.28	6.85	7.01

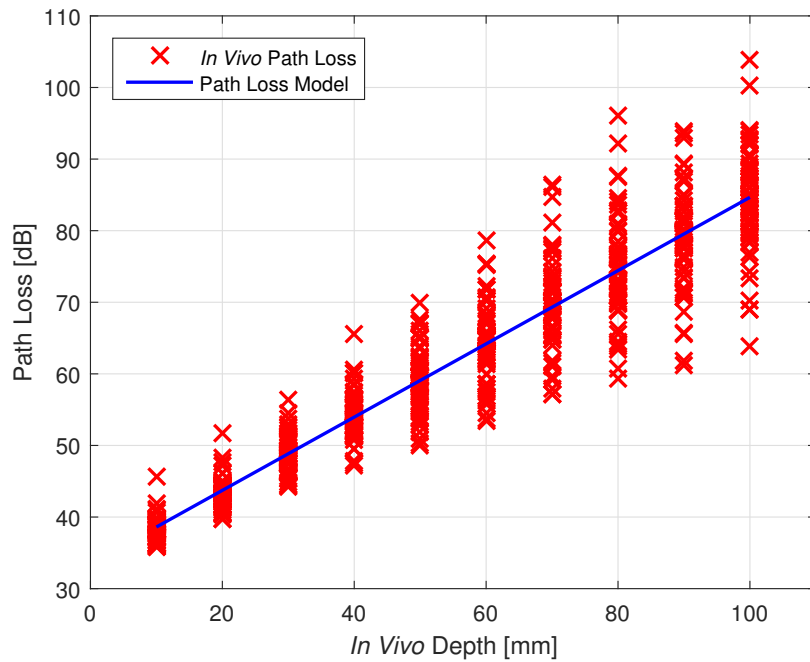
body materials (e.g., bone, muscle, fat, etc.) and the antenna gain in different directions [113]. The proposed *in vivo* PL model is valid for $10 \leq d \leq 100\text{mm}$ and the communication channel between an *in vivo* medical device, and a far external node could be considered as a combination of two concatenated channels: “in-body to on-body” and “classical indoor channel”, if there are no surrounding objects around the body [120]. It should be pointed out that the model is antenna dependent as the majority of other WBAN propagation models in the literature, and this phenomenon is needed to be taken into account for link budget calculations as well.

Figs. 3.7 shows the scatter plots of PL versus *in vivo* depth on torso in the simulation environment at 915 MHz and 2.4 GHz. The mean PL is obtained using a linear regression model. It is observed that the power decay rate (m) is approximately twice at 2.4 GHz due to the high absorption in tissues as compared to 915 MHz (Fig. 3.6). In addition, the variance of the shadowing term, σ , becomes notably larger as the *in vivo* antenna is placed deeper inside the body as shown in Table 3.1. This behavior can be interpreted using the fundamental statistics theorem which states that the variance of independent random variables’ sum equals to the sum of the variances of the random variables (scattering objects) involved in the sum. The *in vivo* channel exhibits a different characteristic than the classical channels, due to the main scatterers present in the vicinity of the antenna, and the variance of shadowing increases significantly compared to free space communications.

The statistical *in vivo* PL model parameters in Eq. 3.2 are provided for each anatomical regions in Tables 3.2 and 3.3, which were obtained by performing extensive simulations. By interpreting them, it could be concluded that PL increases when the *in vivo* antenna is placed in an anatomically complex region. For example, the intestine has a complex structure with repetitive,



(a)



(b)

Figure 3.7: Scatter plots of path loss vs *in vivo* depth in the simulation environment at: (a) 915 MHz; (b) 2.4 GHz.

Table 3.2: Statistical PL model parameters for anatomical regions.

Parameters Body Area	915 MHz			2.4 GHz		
	PL ₀ [dB]	m	σ	PL ₀ [dB]	m	σ
Above Heart	24.26	2.35	3.47	34.14	4.90	3.17
Heart	22.73	2.00	2.13	34.11	4.30	4.85
Stomach - Kidneys	21.90	2.51	1.68	33.03	5.54	4.08
Intestine	23.24	2.27	3.48	32.74	5.71	4.20
Overall Torso Area	23.04	2.28	3.10	33.49	5.12	5.09

Table 3.3: Statistical PL model parameters for anatomical directions.

Parameters Body Area	915 MHz			2.4 GHz		
	PL ₀ [dB]	m	σ	PL ₀ [dB]	m	σ
Anterior	23.47	2.41	3.12	33.83	5.24	5.06
Posterior	23.36	2.18	1.78	33.61	5.27	3.76
Left Lateral	22.64	2.32	3.44	33.42	5.00	5.61
Right Lateral	22.54	2.32	3.29	33.17	4.94	4.99
Overall Torso Area	23.04	2.28	3.10	33.49	5.12	5.09

curvy-shaped, dissimilar tissue layers, while the stomach exhibits a smoother structure. As a result, the PL is greater in the intestine than in the stomach even at equal *in vivo* antenna depths. Also, more radiation occurs in the posterior region than in the anterior region due to the human body structure. To sum up, the location dependency is very critical for link budget calculations and the target anatomical region should be taken into account to design a high-performance, energy-efficient communications system inside the body.

The numerical studies were validated with experiments on a human cadaver at 915 MHz. The *in vivo* antennas were placed at six different locations as shown in Fig. 3.4 and the *ex vivo* antenna was placed 2 cm away from the body surface. Table 3.4 presents the PL values for the selected *in vivo* locations and comparison of experimental results with numerical studies are

Table 3.4: Experimental PL values for selected *in vivo* locations.

Location	<i>In Vivo</i> Depth	Path Loss
01) Above Heart	3 cm	45.32 dB
02) Below Heart	8 cm	55.61 dB
03) Above Stomach	5 cm	48.19 dB
04) Inside Stomach	9 cm	50.80 dB
05) Above Intestine	2 cm	29.95 dB
06) Below Intestine	10 cm	50.47 dB

Table 3.5: Comparison of the statistical PL model parameters.

Environment	PL ₀ [dB]	m	σ
Simulation	23.04	2.28	3.10
Experimental	33.81	2.09	5.56

provided in Fig. 3.8. The discrepancies between the simulated and measured results exist due to the additional losses (e.g., antenna distortion), which were not considered in the simulations and the differences in experimental environment. The statistical *in vivo* PL model parameters are also provided for the experimental study and compared with the numerical study in Table 3.5.

3.3.2 Multipath Characteristics

In addition to the PL and shadowing, multipath propagation characteristics of the *in vivo* channel are also important and should be investigated to discuss proper waveform designs. Received signal strength was explored for various antenna polarizations towards understanding the existence of multipath reflections in the human body medium. As similar to the previous part, the dipole

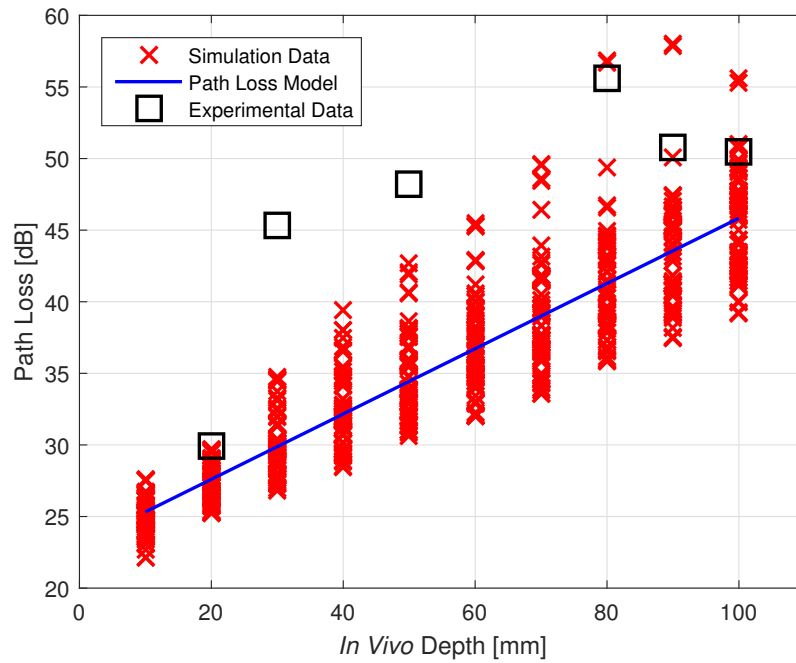


Figure 3.8: Path loss versus *in vivo* depth from the body surface at 915 MHz.

antennas at 915 MHz were deployed in the simulation environment, and they were perfectly matched as mentioned in Section 3.2. The *in vivo* antenna was placed at 5 cm depth on the chest, and the *ex vivo* antenna was placed 5 cm away from the body surface to investigate the “in-body to off-body” link. As a baseline to compare with the *in vivo* channel, the antennas were separated from each other by 10 cm in free space. The *ex vivo* antenna was rotated with 11.25° increments in the YZ-plane for both scenarios as shown in Fig. 3.9 and the maximum available power at the receiver for different polarization mismatch angles is presented in Fig. 3.10. In the free space link, the received power degrades dramatically as the polarization mismatch increases due to the absence of multipath components, i.e., only line-of-sight components are effective on the received signal strength. On the other hand, the received signal power does not change significantly with polarization mismatch for *in vivo* medium. Therefore, it can be concluded that biological tissues inside the human body do not absorb the EM waves completely at 915 MHz and allow reflections that lead to multipath propagation. These reflections will cause small-scale fading which is defined as variations over short distances due to constructive and destructive additions of the signals.

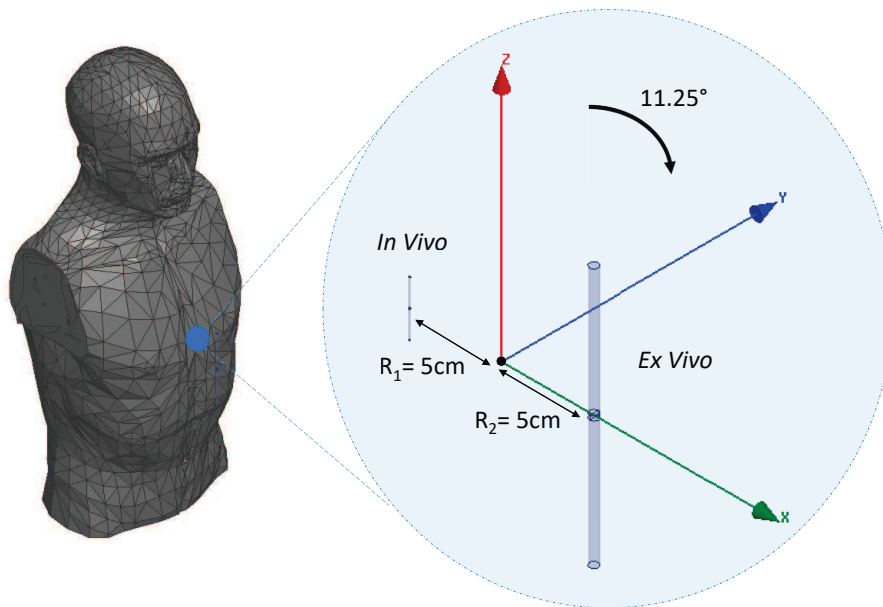


Figure 3.9: Simulation setup for the *in vivo* polarization investigation.

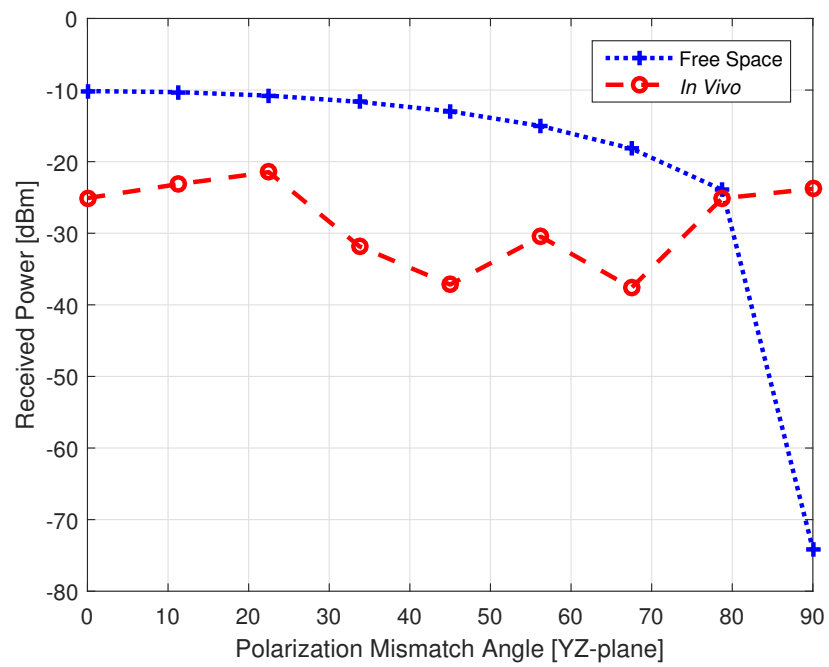


Figure 3.10: Received power for various polarization mismatch angles in the simulation environment at 915 MHz.

As a result of multipath propagation inside the human body, the amount of delay spread should be understood to design an efficient *in vivo* communications systems. Therefore, power delay profiles (PDPs) for various anatomical regions were extracted from the simulation results. The *in vivo* antennas were placed at 5 cm depth on the torso, and the *ex vivo* antennas were placed 5 cm away from the body surface as shown in Fig. 3.11 for four different directions at 915 MHz. The channel impulse response, $h(t)$, was obtained by taking the inverse discrete Fourier transform (IDFT) of the channel frequency response, S_{21} . The PDP was calculated as $PDP(t) = |h(t)|^2$ and the total power is normalized to 1 as presented in Fig. 3.12. Related multipath channel statistics, *mean excess delay* ($\bar{\tau}$), and *RMS delay spread* (σ_τ) are calculated to quantify the time dispersion effect of the *in vivo* channel as follows [121]:

$$\bar{\tau} = \frac{\sum_i \tau_i P(\tau_i)}{\sum_i P(\tau_i)} \quad (3.3)$$

$$\sigma_\tau = \sqrt{\tau^2 - (\bar{\tau})^2} = \sqrt{\frac{\sum_i \tau_i^2 P(\tau_i)}{\sum_i P(\tau_i)} - \left(\frac{\sum_i \tau_i P(\tau_i)}{\sum_i P(\tau_i)} \right)^2} \quad (3.4)$$

where $P(\cdot)$ represents the received power in linear scale and, τ_i denotes the arrival time of the i^{th} path. These parameters for various anatomical directions are listed in Table 3.6 and it is observed that the maximum difference in σ_τ is 0.3 ns. Therefore, it can be stated that there is almost no difference in delay spread for various locations when the antennas are implanted with 5 cm depth on the torso.

RMS delay spread determines the coherence bandwidth (B_c) of the channel. It is a statistical measure of the range of frequencies where the channel can be assumed as “flat” [116] and the 90% B_c is estimated as follows:

$$B_c \approx \frac{1}{50\sigma_\tau} \quad (3.5)$$

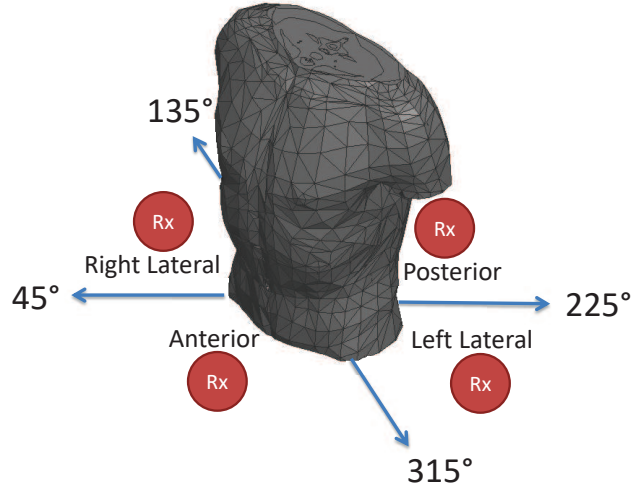


Figure 3.11: Simulation setup for the *in vivo* delay spread investigation.

Table 3.6: *In vivo* multipath propagation statistics at 915 MHz.

Parameters Body Area	Mean Excess Delay ($\bar{\tau}$) [ns]	RMS Delay Spread (σ_{τ}) [ns]
Anterior	2.34	2.59
Posterior	2.32	2.89
Laterals	2.27	2.79

The average σ_{τ} at 5 cm *in vivo* depth is measured as 2.76 ns on the torso and 7.25 MHz coherence bandwidth was predicted using Eq. 3.5. Theoretically, inter-symbol interference (ISI) is not a critical problem when the signal bandwidth (BW) is less than B_c . Hence, the measured delay spread should not cause serious ISI for narrow-band (NB) communications. However, this dispersion may lead to a significant interference for UWB communications, which occupies a BW of greater than 500 MHz.

In frequency-selective channels (i.e., the signal BW is greater than B_c) single-carrier waveforms might not exhibit a sufficient bit error rate (BER) performance without deploying complex equalizers to solve the ISI problem. Nevertheless, power limitation is a major constraint for *in vivo*-WBAN devices and hence, the complexity of signal processing operations must be low. Multi-carrier systems are offered to provide a trivial solution for the ISI problem. For example, orthogonal

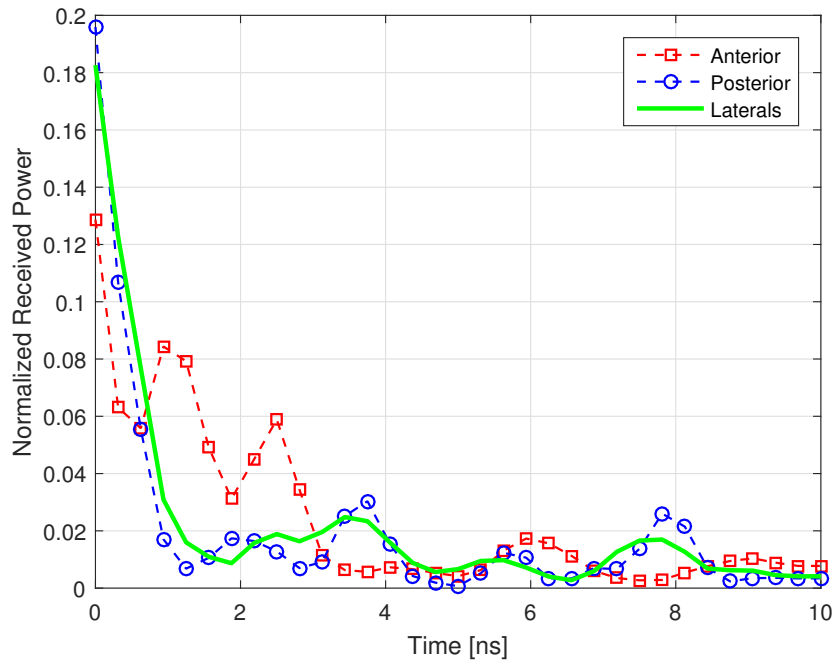


Figure 3.12: Power delay profiles for each anatomical direction in the simulation environment at 915 MHz.

frequency division multiplexing (OFDM) based waveforms can easily handle delay spread using a cyclic prefix. However, high peak-to-average-power ratio (PAPR) emerges as a common problem in multi-carrier waveforms, and it makes the signal vulnerable against the non-linear characteristics of the radio frequency (RF) front-end components. Since the *in vivo*-WBAN devices are restricted in size, the use of high-quality components with high dynamic ranges is impractical. Therefore, PAPR remains as an important issue and may still lead the designers to use single-carrier signaling techniques. To sum up, there are tradeoffs in waveform selection considering the dispersive nature of the *in vivo* channel and practical issues together. The system requirements in terms of throughput, power efficiency, and signal quality need to be clearly identified, and the most proper waveform technology should be selected accordingly.

3.4 Conclusions

This chapter presented the location dependent characteristics of the *in vivo* wireless communications channel for male torso at 915 MHz and 2.4 GHz. Extensive simulations were performed

using a detailed 3D human body model and measurements were conducted on a human cadaver. A statistical *in vivo* path loss model is introduced along with the anatomical region-specific parameters. It is observed that the path loss in dB scale follows a linear decaying profile instead of an exponential characteristic, and the power decay rate is approximately twice at 2.4 GHz as compared to 915 MHz. In addition, the variance of shadowing increases significantly as the *in vivo* antenna is placed deeper inside the body since the main scatterers are present in the vicinity of the antenna. Results show that the location dependency is very critical for link budget calculations, and the target anatomical region should be taken into account to design a high-performance *in vivo* communications system without harming the biological tissues. Multipath propagation characteristics are examined as well to facilitate proper waveforms inside the body by investigating various antenna polarizations and PDPs. A mean RMS delay spread of 2.76 ns is observed at 5 cm *in vivo* depth. Despite the fact that this dispersion may not cause significant ISI for NB communications, it could be a serious issue for UWB communications.

The interest in WBANs is rapidly growing and *in vivo* medical devices are shaping the future of healthcare. This study will contribute significantly to the upcoming WBAN standards and hence, will lead to the design of better *in vivo* transmitter/receiver algorithms.

Chapter 4: Bio-inspired Filter Banks for Frequency Recognition of SSVEP-based Brain-computer Interfaces

4.1 Introduction

Scientific advances in neuroscience and biomedical engineering enabled a direct communication channel between the human brain and a computer ⁶. The electrical activity in the brain that is produced by neuronal post-synaptic membrane polarity changes can be monitored to detect the user's intentions [57]. A brain-computer interface (BCI) [58] analyzes the brain signals and translates them into commands for external devices such as a speller device, wheelchair, robotic arm, or a drone. While there exist multiple approaches to measure brain activity, electroencephalography (EEG) is widely used in BCI applications because of its high temporal resolution, which is essential for BCIs to work as real-time systems [64]. In addition, EEG devices are inexpensive and portable.

A distinctive oscillation pattern in EEG is observed when a sensory stimulus such as visual or auditory is presented to a human. These oscillations are called as evoked potentials (EPs), and they disappear after a short period. If the stimulus is repeated at a regular rate, the EPs do not have time to decay, and it causes a periodic response which is called as steady-state evoked potentials [65]. More specifically, a periodic visual stimulus with a repetition rate higher than 6 Hz elicits steady-state visual evoked potentials (SSVEPs) which are more prominent in the occipital region of the brain [4,66]. The targets that evoke SSVEPs are encoded in various ways [60,67], and the users make a selection by shifting their attention to the desired target in SSVEP based BCIs. Among other BCI modalities which depend on other EEG signals (e.g., slow cortical potentials,

⁶This chapter was published in [10]. Permission is included in Appendix A.

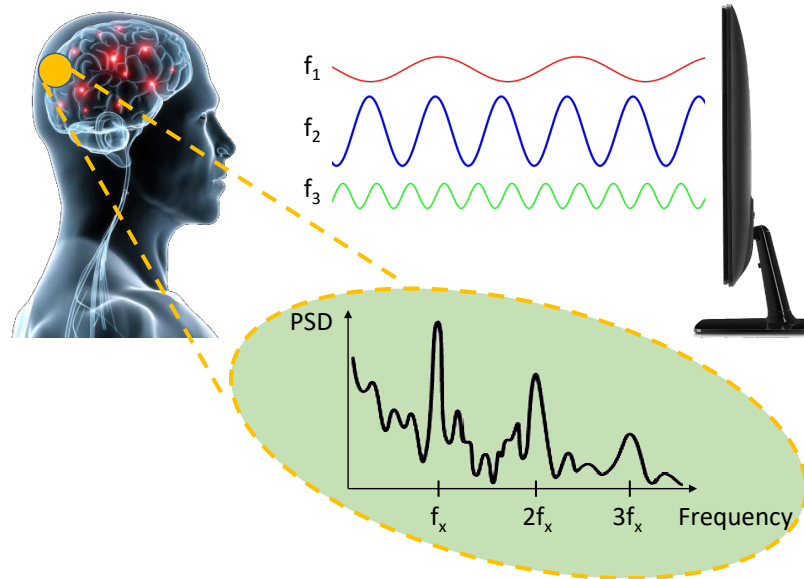


Figure 4.1: SSVEP response to frequency-coded stimuli at the occipital region of the brain.

sensorimotor rhythms, and event-related potentials), SSVEP based BCIs have the advantage of high information transfer rate (ITR) and short training duration to operate the device [68].

SSVEPs are sinusoidal-like waveforms, and they appear at the same fundamental frequency of the driving stimulus and its harmonics (Fig. 4.1) [66]. However, spontaneous oscillations (i.e., background activity), which are not related to the stimulation, exist in the EEG recordings as well and a robust recognition algorithm is required to build a reliable BCI system. Numerous methods have been proposed for SSVEP recognition in the last decade [68,70–75]. Power spectral density analysis (PSDA) is a typical approach since the distinctive features of SSVEPs are observed in the frequency domain [68]. However, PSDA is susceptible to noise, and long durations are needed to increase the signal to noise ratio (SNR). A multivariable statistical method, namely canonical correlation analysis (CCA) [70,72] exploits the multiple channel covariance information to enhance SNR and provide a better recognition accuracy compared to PSDA. Simple implementation, high robustness, and better ITR performance have made CCA attractive in SSVEP recognition research. On the other hand, CCA is not efficient to extract the discriminative information embedded in the harmonic components of SSVEPs, and filter-bank canonical correlation analysis (FBCCA) [73] is proposed to handle this issue. Although FBCCA captures the distinct spectral properties of multiple harmonic

frequencies successfully, it neglects any correlation information between SSVEP responses at different frequencies [74]. Furthermore, this approach disregards the frequency selective nature of SSVEPs due to the utilization of wide-band filters which cover the whole stimuli bandwidth.

To fully exploit and further increase the potential of SSVEP based BCIs, it is necessary to employ an accurate SSVEP model in the recognition algorithm. For example, the inclusion of SSVEP harmonics in a recognition algorithm improves the accuracy [122] since the spontaneous EEG oscillations typically do not present any harmonic components [123]. Also, the subject-specific nature of SSVEPs is handled by an individualized parameter optimization and calibration (e.g., time-window duration, number of harmonics considered, and electrode location) [68, 70]. Moreover, the SSVEP response is frequency selective, and its power gets weaker as the frequency of the stimuli increases [64, 66, 67, 71]. Although the power of EEG background activity decreases as well with the increase in frequency (approximately with a $1/f$ behavior [65]), the resultant SNR is still considerably low at high frequencies. Hence, a visual stimulus at a high frequency can almost be indistinguishable in the presence of noise as shown in Fig. 4.2. This inherent feature not only results in a lower recognition accuracy but also causes exclusion of the stimulus frequencies that evoke weak SSVEP response and decreases the total number of available commands in a BCI system.

This chapter introduces bio-inspired filter banks (BIFBs) for improved SSVEP frequency recognition. The BIFBs are designed considering the inherent biological characteristics of SSVEPs, namely frequency selectivity, subject specificity, and harmonic SSVEP responses. They are utilized in the feature extraction stage to increase the separability of classes. The proposed approach is tested on datasets available online, and its performance is compared with the performances of various SSVEP frequency recognition methods. The preliminary results without an elaborate classification algorithm or a cross-validation procedure were presented in [109]. Also, a fair performance comparison with the utilization of unit filters is provided to validate the effectiveness of the proposed filter bank design in this study. The results show a notable ITR improvement with the bio-inspired design and highlight the promising potential of BIFBs in the high-frequency band,

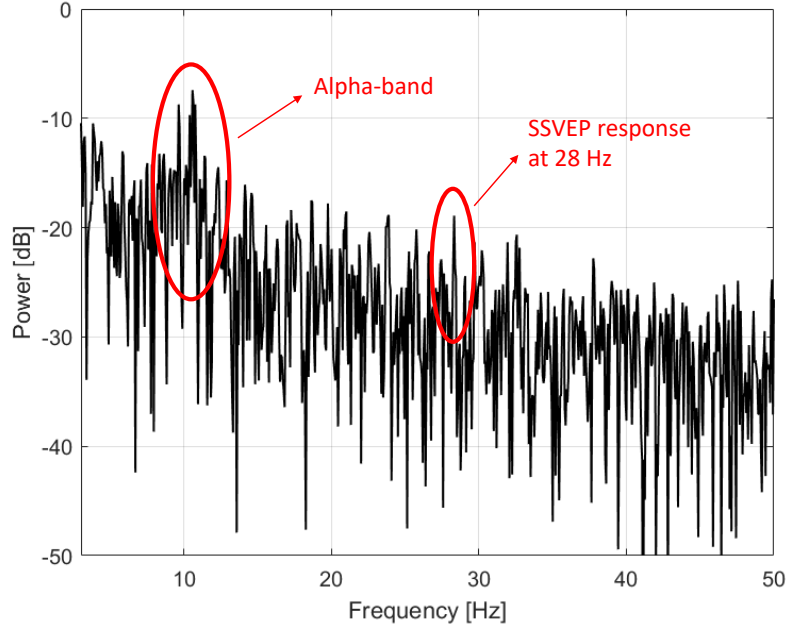


Figure 4.2: The PSD of EEG signal when a visual stimulus at 28 Hz is presented to a participant.

which causes less visual fatigue. Hence, the proposed method leads to more reliable, efficient, and user-friendly SSVEP-based BCI systems. The final research outcomes are published in [10].

This chapter is structured as follows. Section 4.2 describes the performance metrics, evaluation methodology, and datasets. The proposed method is explained in detail, along with the comparison methods. Section 4.3 presents the performance of the SSVEP recognition algorithms and provides a thorough analysis of the results. Finally, Section 4.4 summarizes the contributions and addresses future research directions.

4.2 Methods and Materials

4.2.1 Evaluation Metric

The most common measure to evaluate the performance of a BCI system is ITR [59], which can be expressed in bits/minutes as follows:

$$ITR = s \left[\log_2 \left(K + \delta \log_2 \delta + (1 - \delta) \log_2 \left(\frac{1 - \delta}{K - 1} \right) \right) \right] \quad (4.1)$$

where K stands for the number of equiprobable commands, s denotes the commands performed per minute, and δ represents the accuracy of target recognition. In general, the BCIs with high ITR have a large number of commands. However, K is fixed in these datasets, and the ITR can be boosted with the joint optimization of s and δ . Also, a threshold can be set either on s or δ based on user comfort.

4.2.2 Datasets and Pre-processing

Two publicly-available datasets are utilized in this study to test the proposed method. Dataset-A [71] consists of EEG recordings belong to four healthy subjects with normal or corrected to normal vision. Small reversing black and white checkerboards were presented to the participants sequentially (i.e., one stimulus at a time) at three different frequencies (8 Hz, 14 Hz, and 28 Hz) during the recordings. The brain signal acquisition was performed at a sampling rate of 256 Hz with 128 active electrodes using the ABC layout standard (<https://www.biosemi.com/headcap.htm>) for electrode placement. The EEG recordings were re-referenced using the central Cz electrode and band-pass filtered from 6 Hz to 35 Hz. The subjects experienced a visual stimulus for 15 seconds in each trial. Each unique visual stimulus was repeated for five times, which corresponds to 60 trials (4 subjects x 3 stimuli x 5 repetitions) in total. Dataset-B [124], which is provided by another research institute, consists of EEG recordings belong to four healthy subjects as well. A single flickering box that changes color rapidly from black to white at seven different frequencies (6 Hz, 6.5 Hz, 7 Hz, 7.5 Hz, 8.2 Hz, 9.3 Hz, and 10 Hz) was used as the visual stimulus. The brain signal acquisition was performed at a sampling rate of 512 Hz with three electrodes (Oz, Fpz, Pz) using the 10-20 layout standard for electrode placement. The EEG recordings were referenced using the electrode Fz, and an analog notch filter at 50 Hz was applied to suppress the power-line noise. The subjects experienced a visual stimulus for 30 seconds in each trial. Each unique visual stimulus was repeated at least three times with 92 trials in total.

An overview of these datasets is provided in Table 4.1, and the reader is referred to individual references for a more detailed description of the datasets. Dataset-A is selected to include a stimulus

Table 4.1: Overview of the SSVEP datasets.

Dataset	# of Subjects	# of Trials	Record Length	Sampling Rate	# of Channels	# of Stimulus Frequencies	Stimulus Frequencies
A	4	60	15 s	256	128	3	8 Hz, 14 Hz, 28 Hz
B	4	92	30 s	512	3	7	6 Hz, 6.5 Hz, 7 Hz, 7.5 Hz, 8.2 Hz, 9.3 Hz, 10 Hz

at the high-frequency band that evokes weak SSVEP response, whereas Dataset-B is selected to deal with the frequency selectivity even in a narrow band.

4.2.3 Proposed Method

The pre-processed EEG signal from the occipital channel Oz is segmented with an overlap, and each segment is windowed using a Hamming function [125]. Afterward, the power spectral density of the signal is estimated by the following equation:

$$S_{EEG}[f] = \frac{1}{N} \left| \sum_{n=0}^{N-1} EEG[n] w[n] e^{-j(\frac{2\pi fn}{N})} \right|^2 \quad (4.2)$$

where $EEG[n]$ and $w[n]$ represent the discrete EEG signal and Hamming window function, respectively. The features for SSVEP frequency recognition are extracted by multiplying S_{EEG} with the frequency response of BIFBs. The filter banks are designed in such a way that they capture the inherent biological characteristics of the SSVEPs. It is known that the SSVEPs are frequency-selective, and their power gets weaker as the frequency of the visual stimuli increases [64,66,67,71]. Figure 4.3 presents the average SSVEP response power to pattern reversal stimuli ranging from 5.1 Hz to 84 Hz [71]. Especially, the stimuli at the high-frequency bands elicit weak responses and make the recognition challenging. Consequently, the gain and bandwidth of the filters are designed considering the frequency-selective nature of SSVEPs. Assume that there are K target stimulus frequencies (\tilde{f}_k), where $k = \{1, \dots, K\}$, in a BCI system. The array of filters in BIFBs is expressed as follows:

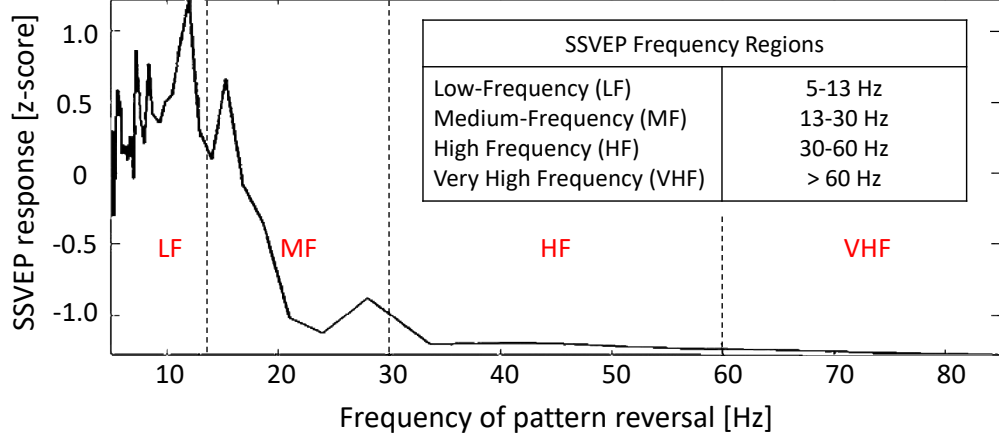


Figure 4.3: SSVEP response to pattern reversal stimuli ranging in frequency from 5.1 Hz to 84 Hz [71].

$$H_{BIFB}^k[f] : \begin{cases} \frac{f - (\tilde{f}_k - BW_k/2)}{BW_k} g_k, & (\tilde{f}_k - BW_k/2) \leq f \leq \tilde{f}_k \\ \frac{(\tilde{f}_k + BW_k/2) - f}{BW_k} g_k, & \tilde{f}_k \leq f \leq (\tilde{f}_k + BW_k/2) \\ 0, & otherwise \end{cases} \quad (4.3)$$

where BW_k and g_k represent the bandwidth and gain of the k^{th} filter, respectively. Initially, higher bandwidth and gain are set to frequencies with low SSVEP response power. Subsequently, these parameters are optimized for individual users in order to counter the subject-specific nature of SSVEP response [68, 70]. A grid search algorithm performed this hyper-parameter optimization through a manually specified subset of the hyper-parameter space [98]. It should be noted that the initial parameter guesses considering the average SSVEP response decrease the computational complexity. Also, SSVEPs occur at the fundamental frequency of the driving stimulus and its harmonics, whereas spontaneous EEG oscillations typically do not present any harmonic components [123]. Accordingly, filters at the SSVEP harmonic frequencies are included in the filter bank design (i.e., $H_{BIFB}^{K+1}[f]$ for $2\tilde{f}_1, \dots, H_{BIFB}^{K+K}[f]$ for $2\tilde{f}_k$) as well to improve the recognition accuracy as shown in Fig. 4.4. Finally, the features are extracted using the BIFBs as follows:

$$x_i = \sum_f S_{EEG}[f] H_{BIFB}^i[f] \quad i = 1, \dots, 2K \quad (4.4)$$

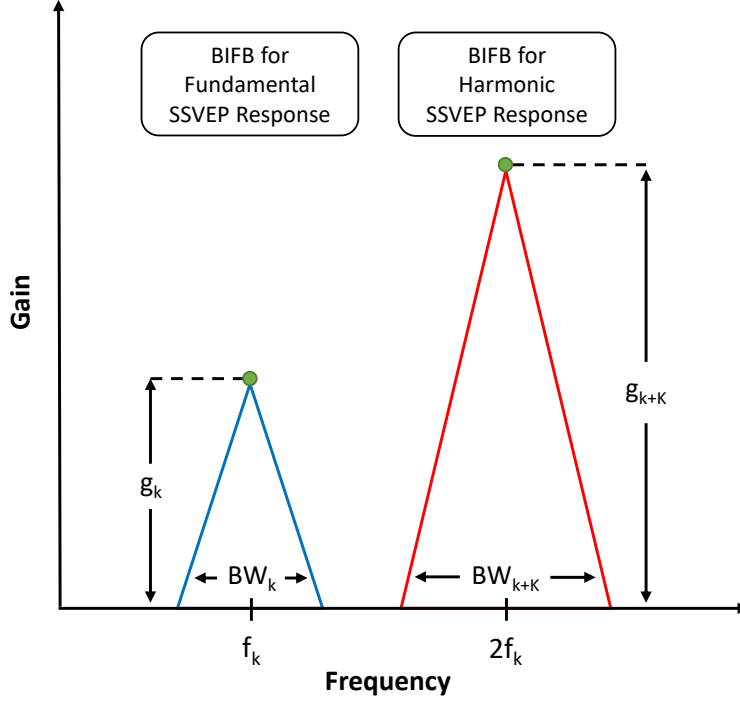


Figure 4.4: A bio-inspired filter design to capture SSVEP response at \tilde{f}_k .

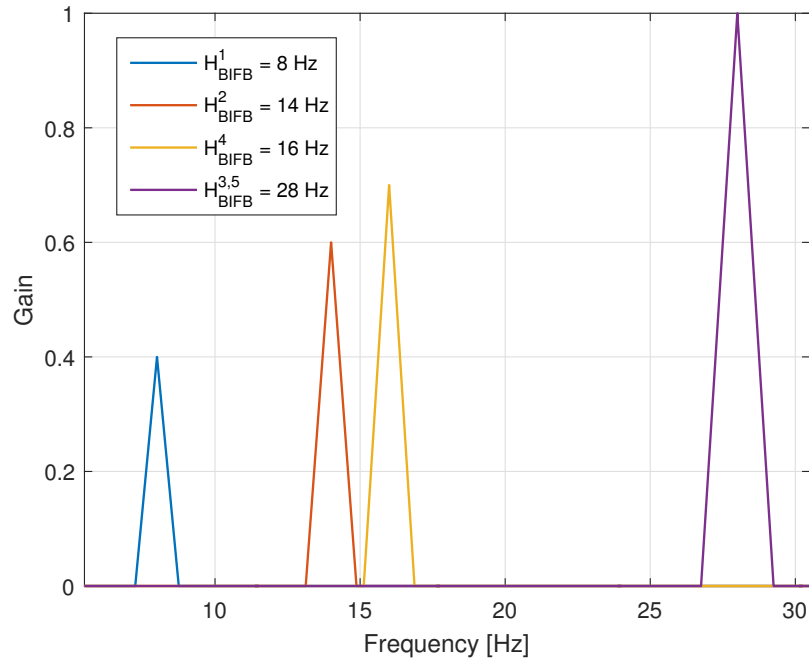
where x_i represents the elements of feature vector X .

The extracted features for SSVEP recognition are classified with a logistic regression model using the one-vs-all strategy. Assume K classes where each class represents a target stimulus frequency. The hypothesis function predicts whether a given input belongs to k^{th} class or not, and it is formulated by the following equation:

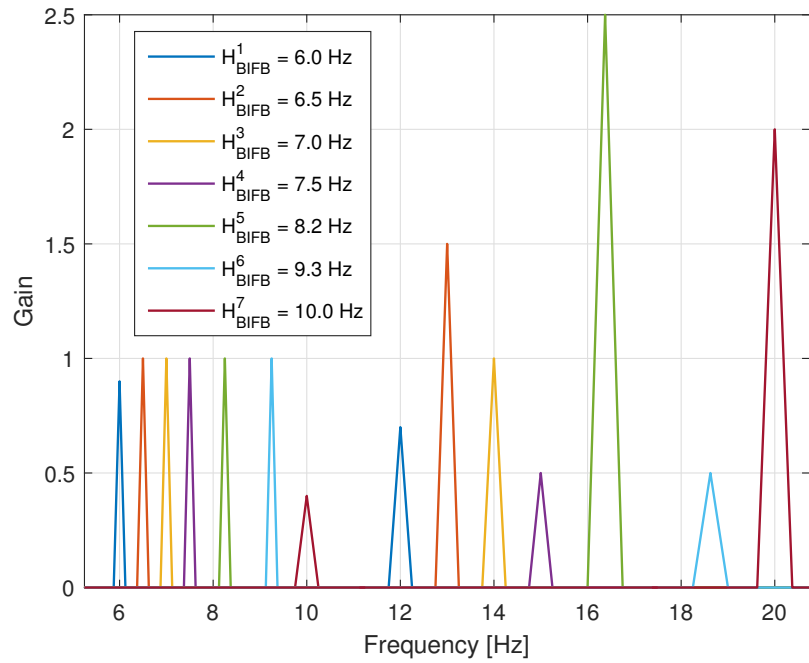
$$h_{\theta}^k(\tilde{X}) = g(\theta_k^T \tilde{X}) = \frac{1}{1 + e^{-\theta_k^T \tilde{X}}} \quad \forall k \quad (4.5)$$

where g represents the sigmoid function, \tilde{X} denotes the augmented feature vector (i.e., $[1, x_1, \dots, x_{2K}]$) with a size of $2K + 1$, and θ_k stands for the mapping weight vector of k^{th} class. θ_k is chosen in such a way that it minimizes the cost function $J(\theta_k)$, which is a distance metric between the prediction and the actual class label (y), by the following equation [126]:

$$J(\theta_k) = \frac{1}{M} \sum_{m=1}^M \left[-y^{(m)} \log \left((h_{\theta}(\tilde{X}^{(m)})) \right) - (1 - y^{(m)}) \right]$$



(a)



(b)

Figure 4.5: (a) A sample BIFB design that mainly deals with low SNR at the high-frequency band (Dataset-A); (b) A sample BIFB design that mainly deals with frequency selectivity (Dataset-B).

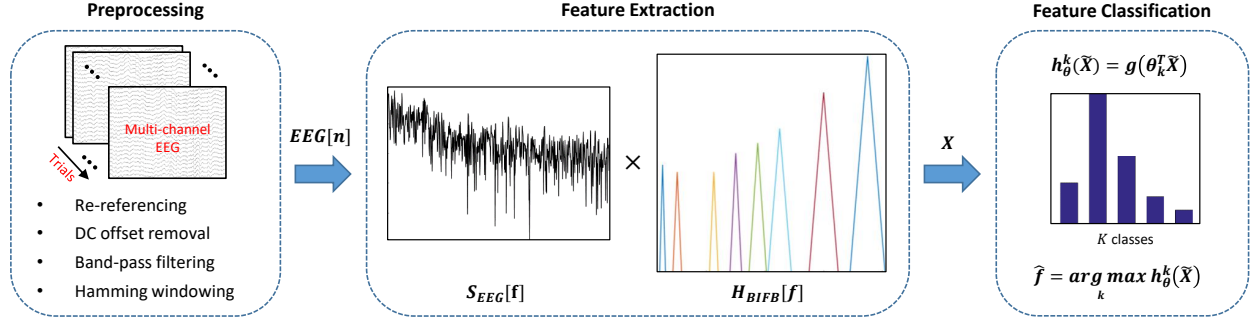


Figure 4.6: Flowchart of the signal processing stages of an SSVEP-based BCI using the proposed BIFBs.

$$\times \log \left(1 - h_{\theta}(\tilde{X}^{(m)}) \right) \Big] + \frac{\lambda}{2M} \sum_{j=1}^{2K} \theta_{k_j}^2 \quad \forall k \quad (4.6)$$

where $\left\{ \left(X^{(m)}, y^{(m)} \right); m = 1, \dots, M \right\}$ represents the training set with M training examples and $y \in \{0, 1\}$. The leave-one-out cross-validation is performed to resample the training data for true objectivity and its suitability for small datasets [127]. The last summative term in Eq. 4.6 prevents over-fitting the classifier and its precision is controlled by the regularization parameter λ . $J(\theta_k)$ is minimized with a gradient descent algorithm, and optimal θ_k is calculated for $\forall k$.

After the training stage, the probability that a given input belongs to each class is calculated using the hypothesis function in Eq. 4.5, and the class with the highest probability is labeled as a candidate frequency for recognition as follows:

$$f_c = \arg \max_k h_{\theta}^k(X) \quad \forall k \quad (4.7)$$

The candidate frequency is labeled as recognized (i.e., $f\hat{f} = f_c$) when the same f_c occurs at least t times in the last T iterations, where the typical values for these parameters are three and four, respectively. If the selection criteria are not satisfied during the given period, it is evaluated as an unsuccessful recognition. A flowchart of the proposed BIFB method for SSVEP frequency recognition is presented in Fig. 4.6.

4.2.4 Comparison Methods

The performance of the proposed algorithm is compared with the performances of various SSVEP frequency recognition algorithms. PSDA and CCA are selected as comparison methods since they are the most common techniques in the literature to compare a new algorithm [72–74]. However, there is no training in these traditional approaches, and a direct comparison may not be proper. Therefore, the BIFBs are replaced with unit filters (UFs), and a similar classical training process is performed for classification to examine the effectiveness of the proposed bio-inspired filter design fairly. Also, the parameters are optimized/calibrated to maximize the ITR performance in all SSVEP frequency recognition methods.

4.2.4.1 UF

It is an SSVEP frequency recognition method, which follows a similar procedure to the proposed scheme in Subsection 4.2.3 except for the utilization of BIFBs. Instead, the features are extracted with unit filters, and they are expressed as follows:

$$H_{UF}^k[f] : \begin{cases} 1 & (\tilde{f}_k - BW_D) \leq f \leq (\tilde{f}_k + BW_D) \\ 0 & otherwise \end{cases} \quad \forall k \quad (4.8)$$

where D is the index for dataset, and BW_D equals to 1 for Dataset-A whereas it is equal to 0.5 for Dataset-B. Since the only difference between BIFB and UF methods is the filter type utilized in the feature extraction stage (like a controlled experiment), any performance difference can be attributed to the filter bank design.

4.2.4.2 PSDA

The EEG signal from the occipital channel is pre-processed, and PSD is estimated similar to the proposed approach. Afterward, the peak of the spectrum is determined as the target frequency ($f\hat{f}$) in the traditional PSDA approach [68]. In this study, the harmonic responses are considered

in the PSDA algorithm as well for a fair comparison. Initially, the class values, where each class represents a target frequency, are calculated by summing the energy in the fundamental frequency and harmonic bands. Subsequently, the class that has the maximum value is recognized as SSVEP target frequency as follows:

$$c_k = \sum_f S_{EEG}[f] H_{UF}^k[f] + \sum_f S_{EEG}[f] H_{UF}^{K+k}[f] \quad (4.9)$$

$$\hat{f} = \max_k c_k \quad \forall k \quad (4.10)$$

4.2.4.3 CCA

The final comparison method, CCA, is a multivariable statistical method that aims to reveal the underlying correlation between two sets of data [128] and has been widely used for SSVEP frequency recognition [70]. If A is a multi-channel EEG signal, and B is the Fourier series of a square-wave stimulus signal, CCA searches for the linear combination vectors (γ_a, γ_b) that maximize the correlation between $\alpha = \gamma_a^T A$ and $\beta = \gamma_b^T B$ by optimizing the following equation:

$$\max_{\gamma_a \gamma_b} \rho(\alpha, \beta) = \frac{E[\gamma_a^T A B^T \gamma_b]}{\sqrt{E[\gamma_a^T A A^T \gamma_a] E[\gamma_b^T B B^T \gamma_b]}} \quad (4.11)$$

The optimization problem in Eq. 4.11 can be solved by a generalized eigenvalue decomposition [129], and the maximum correlation coefficient (ρ) is computed for each B_k . Finally, the SSVEP target frequency is recognized as follows:

$$\hat{f} = \max_k \rho_k \quad \forall k \quad (4.12)$$

A similar pre-processing procedure to PSDA is applied to the multi-channel EEG signal (i.e., A) in CCA as well.

4.3 Results and Discussion

The proposed BIFB method for SSVEP frequency recognition is tested on two datasets that include EEG recordings of eight subjects in 152 trials. The system performance is evaluated in terms of mean recognition time (MRT), recognition accuracy, and ITR by implementing a leave-one-out cross-validation methodology. It is worth to note that ITR changes logarithmically with the number of available commands in Eq. 4.1. The number of commands in each dataset is different, and hence ITRs need to be interpreted separately. The performance of the proposed algorithm is compared with three baseline methods, and the results are listed in Table 4.2 and Table 4.3. The statistical significance of these results is examined by paired t-tests [130], and corresponding p-values are presented in Table 4.4. No multiple comparison correction is considered since the

Table 4.2: Performance evaluation of SSVEP recognition algorithms on Dataset-A.

Dataset - A													
Number of Commands = 3 [8 Hz, 14 Hz, 28Hz], MRT= Mean Recognition Time													
Subject	# of Trials	PSDA			CCA			UF			BIFB		
		MRT (sec)	Acc. (%)	ITR (bits/min)	MRT (sec)	Acc. (%)	ITR (bits/min)	MRT (sec)	Acc. (%)	ITR (bits/min)	MRT (sec)	Acc. (%)	ITR (bits/min)
I	15	5.00	66.67	4.00	3.50	73.33	8.26	5.85	86.67	9.08	5.40	100	17.61
II	15	7.00	73.33	4.13	2.50	66.67	8.00	4.50	80.00	8.84	5.55	100	17.13
III	15	5.00	73.33	5.78	4.25	66.67	4.71	4.70	100	20.23	4.27	100	22.29
IV	15	9.00	53.33	0.81	3.00	66.67	6.67	7.75	66.67	2.58	6.05	93.33	11.55

Table 4.3: Performance evaluation of SSVEP recognition algorithms on Dataset-B.

Dataset - B													
Number of Commands = 7 [6Hz, 6.5Hz, 7Hz, 7.5Hz, 8.2Hz, 9.3Hz, 10Hz], MRT= Mean Recognition Time													
Subject	# of Trials	PSDA			CCA			UF			BIFB		
		MRT (sec)	Acc. (%)	ITR (bits/min)	MRT (sec)	Acc. (%)	ITR (bits/min)	MRT (sec)	Acc. (%)	ITR (bits/min)	MRT (sec)	Acc. (%)	ITR (bits/min)
I	24	7.25	87.50	16.06	5.25	87.50	22.18	4.55	88.42	26.23	4.47	88.38	26.67
II	26	3.75	80.77	25.66	3.50	80.77	27.50	3.43	88.73	35.15	3.03	88.31	39.36
III	21	3.75	80.95	25.80	3.50	85.71	31.65	3.80	80.95	25.48	5.19	100	32.45
IV	21	8.00	85.71	13.85	7.00	100	24.06	3.94	95.24	36.67	4.13	100	40.78

Table 4.4: Statistical analysis of ITR difference between BIFB and comparison methods by using paired t-test.

Compared Method	p-value	
	Dataset-A	Dataset-B
BIFB vs PSDA	$p = 0.0015$	$p = 0.0460$
BIFB vs CCA	$p = 0.0309$	$p = 0.0992$
BIFB vs UF	$p = 0.0239$	$p = 0.0607$

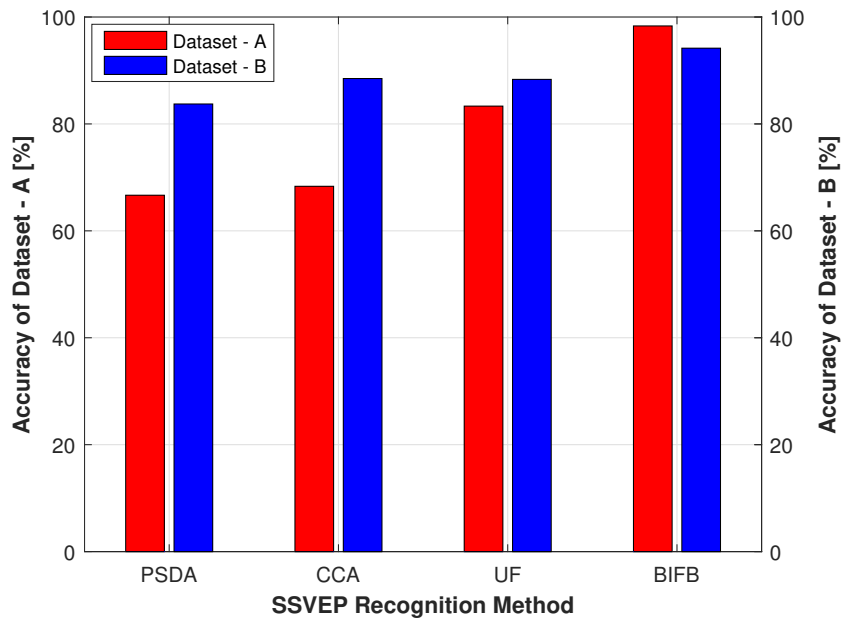
Table 4.5: SSVEP recognition accuracy performance for 28 Hz stimulus in Dataset-A.

Recognition Method	Recognition Accuracy
PSDA	15%
CCA	15%
UF	70%
BIFB	95%

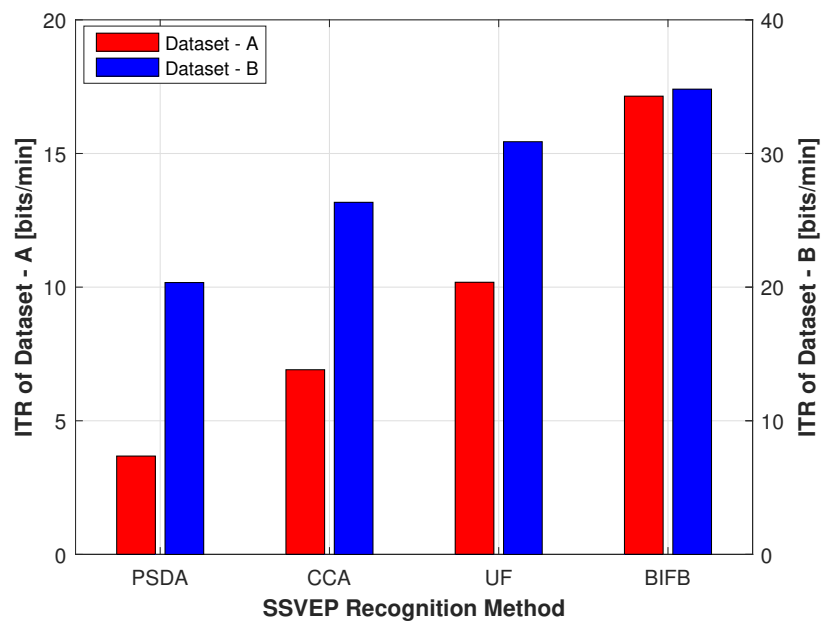
study is restricted to a small number of planned comparisons, and the results of individual tests are important [131].

The traditional PSDA approach requires longer time windows compared to the other three methods to provide sufficient accuracy, which leads to a longer MRT and a lower ITR. A shorter MRT not only improves the ITR but also diminishes the visual fatigue due to a reduced gazing duration. Also, PSDA, as well as CCA, is incapable of detecting stimuli in the high-frequency band. The low recognition accuracy of 28 Hz stimulus, which is presented in Table 4.5, explains the poor performance results of these algorithms in Dataset-A. On the other hand, there are no high-frequency stimuli in Dataset-B, but the frequency selectivity decreases the ITR performances of PSDA, CCA, and UF.

PSDA and CCA have the advantage of not requiring training, and just a straightforward calibration that includes the selection of electrode locations, number of harmonics, and time window duration is sufficient to perform the recognition. However, these algorithms disregard the



(a)



(b)

Figure 4.7: The mean recognition accuracy and ITR performance of the SSVEP recognition methods.

correlation information between the classes. A simple logistic regression model can capture the between-class information and enhance performance. Another classification model may achieve better performance. However, it is beyond the scope of this study, and [132–134] can be referred for more detailed information. The SSVEP response is subject-specific, but the inter-trial variance is low within a subject. Therefore, one-time individualized training is acceptable to acquire a higher ITR. Furthermore, BIFB and UF implement the same classifier. However, a feature extraction stage with BIFB, which captures the underlying biological features of SSVEPs, increases the separability and outperforms UF for SSVEP frequency recognition in both datasets.

User comfort is another important criterion in BCI design besides the ITR. It is reported that high-frequencies cause less visual fatigue induced by the flicker [68, 135]. The promising performance of BIFBs in the high-frequency band may let the designers include this low SNR band in their BCI system. As a result, the user discomfort caused by the flicker reduces, and also ITR increases due to the increase in number of available commands. Furthermore, the number of electrodes is critical for user comfort. Although it is preferable to have a dense sensor system while mapping the brain, it is not suitable for practical BCI applications. In this study, BIFB utilized the information from one electrode for the sake of simplicity. The results show that a single-channel algorithm can provide superior performance compared to a multi-channel algorithm (i.e., CCA), and enhance user comfort as well. However, the use of BIFBs is not restricted to single-channel utilization, and recognition accuracy might be further improved by taking advantage of multi-channel information in the feature extraction stage. For example, a simple way to utilize the BIFBs with multi-channel EEG would be to apply them on signals from the occipital channels and pass the weighted average of the extracted features to the feature classification stage.

4.4 Conclusions

A novel SSVEP recognition method that exploits the inherent biological characteristics of SSVEPs is introduced in this study. The BIFBs capture frequency selectivity, subject specificity, and harmonic SSVEP responses in the feature extraction stage and enhance the separability of classes.

The proposed method is tested on two benchmark datasets available online and outperforms several recognized recognition algorithms. The BIFBs are promising particularly in the high-frequency band where SNR is low. Hence, this method not only increases the ITR of an SSVEP based BCI but also might improve its user comfort due to less visual fatigue. The results show the potential of bio-inspired design, and the findings will be extended to include further SSVEP characteristics. First, the best pulse shape to utilize in the filter banks remains unknown. The triangular filters in this study might need to be replaced with another shape such as Gaussian or raised-cosine to improve the performance further. Second, the BIFBs should incorporate the time-characteristics of SSVEPs. The onset-delay of the response is frequency selective [71] and including this distinct feature might increase the recognition accuracy as well. Last, the SSVEP response also strongly depends on the stimuli type [67, 136], and the BIFB adaptation considering the visual stimuli requires further investigation.

Chapter 5: Concluding Remarks

The performance improvement techniques for next-generation multi-service communication and medical cyber-physical systems are presented in this dissertation with interdisciplinary research efforts. Considering both fields are global research priorities in the commercial and military domains, the research outcomes will significantly accelerate the development, utilization, and standardization of next-generation high-performance systems.

The wireless communication technologies are evolving towards increased flexibility in various aspects. Enhanced flexibility is the key design consideration, especially to be able to serve diverse requirements. Hence, the adaptive guard utilization must be a part of the future communication systems. The research outcomes of Chapter 2 is well-suited to contribute to the ongoing 5G mobile network development, and hopefully, it will provide a strong base for the 6G discussions as well. Also, the interest in WBANs is rapidly growing, and *in vivo* medical devices are already becoming an integral part of healthcare technologies. The research outcomes of Chapter 3 will contribute significantly to the upcoming WBAN standards and hence, will lead to the design of better *in vivo* transmitter/receiver algorithms. Furthermore, BCIs and their associated technologies will shape the future of communication, control, and security as a part of WBAN. Bio-inspired designs such as the proposed techniques in Chapter 4 have the potential to be the key in enabling the development of reliable, efficient, and high-performance BCI systems.

References

- [1] E. Dahlman, S. Parkvall, and J. Skold, *4G, LTE-advanced Pro and the Road to 5G*. Academic Press, 2016.
- [2] Y. Kim, Y. Kim, J. Oh, H. Ji, J. Yeo, S. Choi, H. Ryu, H. Noh, T. Kim, F. Sun, Y. Wang, Y. Qi, and J. Lee, “New radio (NR) and its evolution toward 5G-advanced,” *IEEE Wireless Communications*, vol. 26, no. 3, pp. 2–7, June 2019.
- [3] A. F. Demir, B. Peköz, S. Köse, and H. Arslan, “Innovative telecommunications training through flexible radio platforms,” *IEEE Communications Magazine*, vol. 57, no. 11, pp. 27–33, 2019.
- [4] J. Wolpaw and E. W. Wolpaw, *Brain-Computer Interfaces: Principles and Practice*. Oxford University Press, USA, Jan. 2012.
- [5] S. Movassaghi, M. Abolhasan, J. Lipman, D. Smith, and A. Jamalipour, “Wireless Body Area Networks: A Survey,” *IEEE Communications Surveys Tutorials*, vol. 16, no. 3, pp. 1658–1686, 2014.
- [6] A. F. Demir, Z. E. Ankarali, Q. H. Abbasi, Y. Liu, K. Qaraqe, E. Serpedin, H. Arslan, and R. D. Gitlin, “In Vivo Communications: Steps Toward the Next Generation of Implantable Devices,” *IEEE Vehicular Technology Magazine*, vol. 11, no. 2, pp. 32–42, Jun. 2016.
- [7] H. Sun, Z. Zhang, R. Q. Hu, and Y. Qian, “Wearable communications in 5G: Challenges and enabling technologies,” *IEEE Vehicular Technology Magazine*, vol. 13, no. 3, pp. 100–109, 2018.

- [8] A. F. Demir, Q. H. Abbasi, Z. E. Ankarali, A. Alomainy, K. Qaraqe, E. Serpedin, and H. Arslan, "Anatomical Region-Specific In Vivo Wireless Communication Channel Characterization," *IEEE Journal of Biomedical and Health Informatics*, vol. 21, no. 5, pp. 1254–1262, Sept 2017.
- [9] A. F. Demir, M. Elkourdi, M. Ibrahim, and H. Arslan, "Waveform Design for 5G and Beyond," in *5G Networks: Fundamental Requirements, Enabling Technologies, and Operations Management*. John Wiley & Sons, Ltd, 2018, ch. 2, pp. 51–76.
- [10] A. F. Demir, H. Arslan, and I. Uysal, "Bio-inspired filter banks for frequency recognition of SSVEP-based brain-computer interfaces," *IEEE Access*, vol. 7, pp. 160 295–160 303, 2019.
- [11] A. F. Demir and H. Arslan, "Inter-numerology interference management with adaptive guards: A cross-layer approach," *IEEE Access*, vol. 8, pp. 30 378–30 386, 2020.
- [12] X. Lin, J. Li, R. Baldemair, J. T. Cheng, S. Parkvall, D. C. Larsson, H. Koorapaty, M. Frenne, S. Falahati, A. Grovlen, and K. Werner, "5G new radio: Unveiling the essentials of the next generation wireless access technology," *IEEE Communications Standards Magazine*, vol. 3, no. 3, pp. 30–37, Sep. 2019.
- [13] ITU-R, "IMT Vision - Framework and Overall Objectives of the Future Development of IMT for 2020 and Beyond," Tech. Rep., Sept. 2015.
- [14] C. Urmson and W. Whittaker, "Self-Driving Cars and the Urban Challenge," *IEEE Intelligent Systems*, vol. 23, no. 2, pp. 66–68, Mar. 2008.
- [15] A. Sahin, I. Guvenc, and H. Arslan, "A Survey on Multicarrier Communications: Prototype Filters, Lattice Structures, and Implementation Aspects," *IEEE Commun. Surveys Tuts.*, vol. 16, no. 3, pp. 1312–1338, Third 2014.

- [16] T. Hwang, C. Yang, G. Wu, S. Li, and G. Y. Li, "OFDM and Its Wireless Applications: A Survey," *IEEE Transactions on Vehicular Technology*, vol. 58, no. 4, pp. 1673–1694, May 2009.
- [17] Y. Rahmatallah and S. Mohan, "Peak-To-Average Power Ratio Reduction in OFDM Systems: A Survey And Taxonomy," *IEEE Communications Surveys Tutorials*, vol. 15, no. 4, pp. 1567–1592, 2013.
- [18] X. Zhang, L. Chen, J. Qiu, and J. Abdoli, "On the Waveform for 5G," *IEEE Communications Magazine*, vol. 54, no. 11, pp. 74–80, Nov. 2016.
- [19] Qualcomm Inc., "Waveform Candidates," 3GPP Standard Contribution (R1-162199), Busan, Korea, Apr. 11-15 2016.
- [20] A. Sahin, R. Yang, E. Bala, M. C. Beluri, and R. L. Olesen, "Flexible DFT-S-OFDM: Solutions and Challenges," *IEEE Communications Magazine*, vol. 54, no. 11, pp. 106–112, Nov. 2016.
- [21] G. Berardinelli, K. I. Pedersen, T. B. Sorensen, and P. Mogensen, "Generalized DFT-Spread-OFDM as 5G Waveform," *IEEE Communications Magazine*, vol. 54, no. 11, pp. 99–105, Nov. 2016.
- [22] M. Ibrahim, A. F. Demir, and H. Arslan, "Time-Frequency Warped Waveforms," *IEEE Communications Letters*, vol. 23, no. 1, pp. 36–39, Jan 2019.
- [23] Huawei, HiSilicon, "5G Waveform: Requirements and Design Principles," 3GPP Standard Contribution (R1-162151), Busan, Korea, Apr. 11-15 2016.
- [24] S. Parkvall, E. Dahlman, A. Furuskar, and M. Frenne, "NR: The New 5G Radio Access Technology," *IEEE Commun. Standards Mag.*, vol. 1, no. 4, pp. 24–30, Dec. 2017.

- [25] S. Lien, S. Shieh, Y. Huang, B. Su, Y. Hsu, and H. Wei, "5G new radio: Waveform, frame structure, multiple access, and initial access," *IEEE Communications Magazine*, vol. 55, no. 6, pp. 64–71, June 2017.
- [26] Z. E. Ankarali, B. Peköz, and H. Arslan, "Flexible Radio Access Beyond 5G: A Future Projection on Waveform, Numerology, and Frame Design Principles," *IEEE Access*, vol. 5, pp. 18 295–18 309, 2017.
- [27] A. A. Zaidi, R. Baldemair, H. Tullberg, H. Bjorkegren, L. Sundstrom, J. Medbo, C. Kilinc, and I. D. Silva, "Waveform and Numerology to Support 5G Services and Requirements," *IEEE Communications Magazine*, vol. 54, no. 11, pp. 90–98, November 2016.
- [28] A. B. Kihero, M. S. J. Solaija, and H. Arslan, "Inter-numerology interference for beyond 5G," *IEEE Access*, vol. 7, pp. 146 512–146 523, 2019.
- [29] *IEEE standard for local and metropolitan area networks: Part 15.6: Wireless body area networks,* *IEEE submission, Feb. 2012.*, IEEE Std.
- [30] A. Kiourti, K. A. Psathas, and K. S. Nikita, "Implantable and ingestible medical devices with wireless telemetry functionalities: A review of current status and challenges," *Bioelectromagnetics*, vol. 15, pp. 1–15, August 2013.
- [31] A. F. Demir, Z. E. Ankarali, Y. Liu, Q. H. Abbasi, K. Qaraq, E. Serpedin, H. Arslan, and R. D. Gitlin, "In Vivo Wireless Channel Modeling," in *Advances in Body-Centric Wireless Communication: Applications and state-of-the-art*. Institution of Engineering and Technology, Jun. 2016, pp. 187–211.
- [32] P. S. Hall and Y. Hao, *Antennas and Propagation for Body-Centric Wireless Communications, Second Edition*. Artech House, 2012.

- [33] A. Alomainy and Y. Hao, "Modeling and Characterization of Biotelemetric Radio Channel From Ingested Implants Considering Organ Contents," *IEEE Transactions on Antennas and Propagation*, vol. 57, no. 4, pp. 999–1005, Apr. 2009.
- [34] A. Pellegrini, A. Brizzi, L. Zhang, K. Ali, Y. Hao, X. Wu, C. Constantinou, Y. Nechayev, P. Hall, N. Chahat *et al.*, "Antennas and propagation for body-centric wireless communications at millimeter-wave frequencies: A review [wireless corner]," *Antennas and Propagation Magazine, IEEE*, vol. 55, no. 4, pp. 262–287, 2013.
- [35] S. H. Lee, J. Lee, Y. J. Yoon, S. Park, C. Cheon, K. Kim, and S. Nam, "A wideband spiral antenna for ingestible capsule endoscope systems: experimental results in a human phantom and a pig," *IEEE Transactions on Biomedical Engineering*, vol. 58, pp. 1734–41, Jun. 2011.
- [36] R. Chavez-Santiago, I. Balasingham, J. Bergsland, W. Zahid, K. Takizawa, R. Miura, and H.-B. Li, "Experimental implant communication of high data rate video using an ultra wideband radio link," in *Engineering in Medicine and Biology Society (EMBC), 2013 35th Annual International Conference of the IEEE*. IEEE, 2013, pp. 5175–5178.
- [37] H. Y. Lin, M. Takahashi, K. Saito, and K. Ito, "Characteristics of Electric Field and Radiation Pattern on Different Locations of the Human Body for In-Body Wireless Communication," *IEEE Transactions on Antennas and Propagation*, vol. 61, no. 10, pp. 5350–5354, Oct. 2013.
- [38] A. F. Demir, Q. H. Abbasi, Z. E. Ankarali, M. Qaraqe, E. Serpedin, and H. Arslan, "Experimental Characterization of In Vivo Wireless Communication Channels," in *Vehicular Technology Conference (VTC Fall), 2015 IEEE 82nd*, Sep. 2015, pp. 1–2.
- [39] K. Y. Yazdandoost, *Wireless Mobile Communication and Healthcare*. Springer Berlin Heidelberg, 2012, ch. A Radio Channel Model for In-body Wireless Communications, pp. 88–95.

- [40] T. P. Ketterl, G. E. Arrobo, and R. D. Gitlin, "SAR and BER evaluation using a simulation test bench for in vivo communication at 2.4 GHz," in *Wireless and Microwave Technology Conference (Wamicon), IEEE*, 2013.
- [41] W. Scanlon, "Analysis of tissue-coupled antennas for UHF intra-body communications," 2003.
- [42] A. Sani, A. Alomainy, and Y. Hao, "Numerical Characterization and Link Budget Evaluation of Wireless Implants Considering Different Digital Human Phantoms," *IEEE Transactions on Microwave Theory and Techniques*, vol. 57, no. 10, pp. 2605–2613, Oct. 2009.
- [43] K. Sayrafian-Pour, W.-B. Yang, J. Hagedorn, J. Terrill, K. Yekeh Yazdandoost, and K. Hamaguchi, "Channel models for medical implant communication," *International Journal of Wireless Information Networks*, vol. 17, no. 3, pp. 105–112, Dec 2010. [Online]. Available: <https://doi.org/10.1007/s10776-010-0124-y>
- [44] H. Bahrami, B. Gosselin, and L. A. Rusch, "Realistic modeling of the biological channel for the design of implantable wireless UWB communication systems," in *Engineering in Medicine and Biology Society (EMBC) Annual International Conference, IEEE*, 2012.
- [45] M. S. Wegmueller, A. Kuhn, J. Froehlich, M. Oberle, N. Felber, N. Kuster, and W. Fichtner, "An attempt to model the human body as a communication channel," *Biomedical Engineering, IEEE Transactions on*, vol. 54, no. 10, pp. 1851–1857, 2007.
- [46] R. Chavez-Santiago, K. Sayrafian-Pour, A. Khaleghi, K. Takizawa, J. Wang, I. Balasingham, and H.-B. Li, "Propagation models for IEEE 802.15. 6 standardization of implant communication in body area networks," *Communications Magazine, IEEE*, vol. 51, no. 8, 2013.
- [47] J. Kim and Y. Rahmat-Samii, "Implanted antennas inside a human body: Simulations, designs, and characterizations," *Microwave Theory and Techniques, IEEE Transactions on*, vol. 52, no. 8, pp. 1934–1943, 2004.

- [48] J. Gemio, J. Parron, and J. Soler, "Human body effects on implantable antennas for ISM bands applications: Models comparison and propagation losses study," *Progress in Electromagnetics Research*, vol. 110, pp. 437–452, Oct. 2010.
- [49] T. Karacolak, A. Hood, and E. Topsakal, "Design of a dual-band implantable antenna and development of skin mimicking gels for continuous glucose monitoring," *Microwave Theory and Techniques, IEEE Transactions on*, vol. 56, pp. 1001–1008, April 2008.
- [50] A. Laskovski and M. Yuce, "A MICS telemetry implant powered by a 27MHz ISM inductive link," in *Engineering in Medicine and Biology Society, EMBC, 2011 Annual International Conference of the IEEE*, 2011.
- [51] M. L. Scarpello, D. Kurup, H. Rogier, D. Vande Ginste, F. Axisa, J. Vanfleteren, W. Joseph, L. Martens, and G. Vermeeren, "Design of an implantable slot dipole conformal flexible antenna for biomedical applications," *Antennas and Propagation, IEEE Transactions on*, vol. 59, no. 10, pp. 3556–3564, 2011.
- [52] M. R. Basar, M. F. B. A. Malek, K. M. Juni, M. I. M. Saleh, M. S. Idris, L. Mohamed, N. Saudin, N. A. Mohd Affendi, and A. Ali, "The Use Of a Human Body Model To Determine The Variation Of Path Losses In The Human Body Channel In Wireless Capsule Endoscopy," *Progress In Electromagnetics Research*, vol. 133, pp. 495–513, 2013.
- [53] A. F. Demir, Q. H. Abbasi, Z. E. Ankarali, E. Serpedin, and H. Arslan, "Numerical characterization of in vivo wireless communication channels," in *2014 IEEE MTT-S International Microwave Workshop Series on RF and Wireless Technologies for Biomedical and Healthcare Applications (IMWS-Bio)*, Dec. 2014, pp. 1–3.
- [54] Z. N. Chen, G. C. Liu, and T. S. See, "Transmission of RF signals between MICS loop antennas in free space and implanted in the human head," *Antennas and Propagation, IEEE Transactions on*, vol. 57.6, pp. 1850–1854, 2009.

- [55] S. K. S. Gupta, S. Lalwani, Y. Prakash, E. Elsharawy, and L. Schwiebert, "Towards a propagation model for wireless biomedical applications," in *IEEE Int. Conference on Communications (ICC)*, 2003.
- [56] S. Stoa, C. S. Raul, and I. Balasingham, "An ultra wideband communication channel model for the human abdominal region," in *GLOBECOM Workshops (GC Workshops)*, IEEE, 2010.
- [57] J. J. Shih, D. J. Krusienski, and J. R. Wolpaw, "Brain-Computer Interfaces in Medicine," *Mayo Clinic Proceedings*, vol. 87, no. 3, pp. 268–279, Mar. 2012.
- [58] J. J. Vidal, "Toward Direct Brain-Computer Communication," *Annual Review of Biophysics and Bioengineering*, vol. 2, no. 1, pp. 157–180, 1973.
- [59] J. R. Wolpaw, N. Birbaumer, D. J. McFarland, G. Pfurtscheller, and T. M. Vaughan, "Brain-computer Interfaces for Communication and Control," *Clinical Neurophysiology*, vol. 113, no. 6, pp. 767–791, Jun. 2002.
- [60] S. Gao, Y. Wang, X. Gao, and B. Hong, "Visual and Auditory Brain Computer Interfaces," vol. 61, no. 5, pp. 1436–1447, May 2014.
- [61] J. F. Valenzuela-Valdes, M. A. Lopez, P. Padilla, J. L. Padilla, and J. Minguillon, "Human Neuro-Activity for Securing Body Area Networks: Application of Brain-Computer Interfaces to People-Centric Internet of Things," vol. 55, no. 2, pp. 62–67, Feb. 2017.
- [62] G. Schirner, D. Erdogmus, K. Chowdhury, and T. Padir, "The Future of Human-in-the-Loop Cyber-Physical Systems," *Computer*, vol. 46, no. 1, pp. 36–45, Jan. 2013.
- [63] M. Wang, R. Li, R. Zhang, G. Li, and D. Zhang, "A wearable SSVEP-based BCI system for quadcopter control using head-mounted device," *IEEE Access*, vol. 6, pp. 26 789–26 798, 2018.

- [64] F.-B. Vialatte, M. Maurice, J. Dauwels, and A. Cichocki, “Steady-state visually evoked potentials: Focus on essential paradigms and future perspectives,” *Progress in Neurobiology*, vol. 90, no. 4, pp. 418–438, Apr. 2010.
- [65] A. Paris, G. K. Atia, A. Vosoughi, and S. A. Berman, “A New Statistical Model of Electroencephalogram Noise Spectra for Real-Time Brain Computer Interfaces,” vol. 64, no. 8, pp. 1688–1700, Aug. 2017.
- [66] C. S. Herrmann, “Human EEG responses to 1–100 Hz flicker: resonance phenomena in visual cortex and their potential correlation to cognitive phenomena,” *Experimental Brain Research*, vol. 137, no. 3-4, pp. 346–353, Apr. 2001.
- [67] D. Zhu, J. Bieger, G. Garcia Molina, and R. M. Aarts, “A Survey of Stimulation Methods Used in SSVEP-Based BCIs,” *Comput. Intell. Neurosci.*, 2010.
- [68] Y. Wang, R. Wang, X. Gao, B. Hong, and S. Gao, “A Practical VEP-based Brain-computer Interface,” vol. 14, no. 2, pp. 234–240, Jun. 2006.
- [69] S. Amiri, A. Rabbi, L. Azinfar, and R. Fazel-Rezai, “A review of P300, SSVEP, and hybrid P300/SSVEP brain-computer interface systems,” in *Brain-Computer Interface Systems - Recent Progress and Future Prospects*. InTech, 2013.
- [70] Z. Lin, C. Zhang, W. Wu, and X. Gao, “Frequency recognition based on canonical correlation analysis for SSVEP-based BCIs,” vol. 54, no. 6, pp. 1172–1176, Jun. 2007.
- [71] H. Bakardjian, T. Tanaka, and A. Cichocki, “Optimization of SSVEP brain responses with application to eight-command Brain-Computer Interface,” *Neuroscience Letters*, vol. 469, no. 1, pp. 34–38, Jan. 2010.
- [72] Y. Zhang, G. Zhou, J. Jin, M. Wang, X. Wang, and A. Cichocki, “L1-Regularized Multiway Canonical Correlation Analysis for SSVEP-Based BCI,” vol. 21, no. 6, pp. 887–896, Nov. 2013.

- [73] X. Chen, Y. Wang, S. Gao, T.-P. Jung, and X. Gao, "Filter bank canonical correlation analysis for implementing a high-speed SSVEP-based brain-computer interface," *Journal of Neural Engineering*, vol. 12, no. 4, p. 046008, Aug. 2015.
- [74] H. Wang, Y. Zhang, N. R. Waytowich, D. J. Krusienski, G. Zhou, J. Jin, X. Wang, and A. Cichocki, "Discriminative Feature Extraction via Multivariate Linear Regression for SSVEP-Based BCI," vol. 24, no. 5, pp. 532–541, May 2016.
- [75] M. Bittencourt-Villalpando and N. M. Maurits, "Stimuli and feature extraction algorithms for brain-computer interfaces: A systematic comparison," *IEEE Transactions on Neural Systems and Rehabilitation Engineering*, vol. 26, no. 9, pp. 1669–1679, Sep. 2018.
- [76] Huawei, HiSilicon, "Scenario and design criteria on flexible numerologies," 3GPP Standard Contribution (R1-162156), Busan, Korea, Apr. 11-15 2016.
- [77] X. Zhang, L. Zhang, P. Xiao, D. Ma, J. Wei, and Y. Xin, "Mixed numerologies interference analysis and inter-numerology interference cancellation for windowed OFDM systems," *IEEE Transactions on Vehicular Technology*, vol. 67, no. 8, pp. 7047–7061, Aug 2018.
- [78] B. Pekoz, Z. E. Ankarali, S. Kose, and H. Arslan, "Non-redundant OFDM receiver windowing for 5G frames beyond," *IEEE Transactions on Vehicular Technology*, pp. 1–1, 2019.
- [79] M. Yang, Y. Chen, and L. Du, "Interference analysis and filter parameters optimization for uplink asynchronous f-OFDM systems," *IEEE Access*, vol. 7, pp. 48 356–48 370, 2019.
- [80] T. Levanen, J. Pirskanen, K. Pajukoski, M. Renfors, and M. Valkama, "Transparent Tx and Rx waveform processing for 5G new radio mobile communications," *IEEE Wireless Communications*, vol. 26, no. 1, pp. 128–136, February 2019.
- [81] J. Yli-Kaakinen, T. Levanen, S. Valkonen, K. Pajukoski, J. Pirskanen, M. Renfors, and M. Valkama, "Efficient fast-convolution-based waveform processing for 5G physical layer,"

- IEEE Journal on Selected Areas in Communications*, vol. 35, no. 6, pp. 1309–1326, June 2017.
- [82] L. Zhang, A. Ijaz, P. Xiao, A. Quddus, and R. Tafazolli, “Subband filtered multi-carrier systems for multi-service wireless communications,” *IEEE Transactions on Wireless Communications*, vol. 16, no. 3, pp. 1893–1907, March 2017.
- [83] Y. Lim, T. Jung, K. S. Kim, C. Chae, and R. A. Valenzuela, “Waveform multiplexing for new radio: Numerology management and 3D evaluation,” *IEEE Wireless Communications*, vol. 25, no. 5, pp. 86–94, October 2018.
- [84] Y. Huang and B. Su, “Circularly pulse-shaped precoding for OFDM: A new waveform and its optimization design for 5G new radio,” *IEEE Access*, vol. 6, pp. 44 129–44 146, 2018.
- [85] A. F. Demir and H. Arslan, “The Impact of Adaptive Guards for 5G and Beyond,” in *2017 IEEE 28th Annual Int. Symp. on Personal, Indoor, and Mobile Radio Commun. (PIMRC)*, Oct 2017, pp. 1–5.
- [86] —, “System and Method for Adaptive OFDM Guards,” U.S. Patent 10,411,819, Sept. 2019.
- [87] B. Farhang-Boroujeny, “OFDM Versus Filter Bank Multicarrier,” *IEEE Signal Processing Mag.*, vol. 28, no. 3, pp. 92–112, May 2011.
- [88] T. Weiss, J. Hillenbrand, A. Krohn, and F. K. Jondral, “Mutual Interference in OFDM-based Spectrum Pooling Systems,” in *2004 IEEE 59th Veh. Technol. Conf.*, vol. 4, May 2004, pp. 1873–1877 Vol.4.
- [89] E. Bala, J. Li, and R. Yang, “Shaping Spectral Leakage: A Novel Low-Complexity Transceiver Architecture for Cognitive Radio,” *IEEE Veh. Tech. Mag.*, vol. 8, no. 3, pp. 38–46, Sep. 2013.

- [90] 3GPP TS 38.104 V15.4.0, “New Radio (NR); Base Station (BS) radio transmission and reception,” Tech. Spec. Group Radio Access Network, Rel. 15, Dec. 2018.
- [91] A. Sahin and H. Arslan, “Edge Windowing for OFDM Based Systems,” *IEEE Communications Letters*, vol. 15, no. 11, pp. 1208–1211, Nov. 2011.
- [92] Samsung, “Discussion on Multi-window OFDM for NR Waveform,” 3GPP Standard Contribution (R1-166746), Gothenburg, Sweden, Aug. 22-26 2016.
- [93] A. Yazar and H. Arslan, “A flexibility metric and optimization methods for mixed numerologies in 5G and beyond,” *IEEE Access*, vol. 6, pp. 3755–3764, 2018.
- [94] T. van Waterschoot, V. L. Nir, J. Duplicy, and M. Moonen, “Analytical Expressions for the Power Spectral Density of CP-OFDM and ZP-OFDM Signals,” *IEEE Signal Processing Letters*, vol. 17, no. 4, pp. 371–374, April 2010.
- [95] S. L. Talbot and B. Farhang-Boroujeny, “Spectral Method of Blind Carrier Tracking for OFDM,” *IEEE Transactions on Signal Processing*, vol. 56, no. 7, pp. 2706–2717, July 2008.
- [96] C. Liu and F. Li, “Spectrum Modelling of OFDM Signals for WLAN,” *Electronics Letters*, vol. 40, no. 22, pp. 1431–1432, Oct 2004.
- [97] L. Montreuil, R. Prodan, and T. Kolze, “OFDM TX Symbol Shaping,” Broadcom Inc., Tech. Rep., 2013.
- [98] J. S. Bergstra, R. Bardenet, Y. Bengio, and B. Kégl, “Algorithms for hyper-parameter optimization,” in *Adv. Neural Inf. Process Syst.*, 2011, pp. 2546–2554.
- [99] J. G. Proakis, *Digital Communications*. McGraw-Hill, New York, 2001.
- [100] X. Zhang, M. Jia, L. Chen, J. Ma, and J. Qiu, “Filtered-OFDM - Enabler for Flexible Waveform in the 5th Generation Cellular Networks,” in *IEEE Global Commun. Conf.*, Dec. 2015, pp. 1–6.

- [101] V. Vakilian, T. Wild, F. Schaich, S. ten Brink, and J. Frigon, "Universal-filtered Multi-carrier Technique for Wireless Systems Beyond LTE," in *2013 IEEE Globecom Workshops*, Dec 2013, pp. 223–228.
- [102] G. Fettweis, M. Krondorf, and S. Bittner, "GFDM - Generalized Frequency Division Multiplexing," in *IEEE 69th Veh. Technol. Conf.*, April 2009, pp. 1–4.
- [103] B. Farhang-Boroujeny and H. Moradi, "OFDM Inspired Waveforms for 5G," *IEEE Commun. Surveys Tuts.*, vol. 18, no. 4, pp. 2474–2492, Fourthquarter 2016.
- [104] Q. H. Abbasi, A. Sani, A. Alomainy, and Y. Hao, "On-Body Radio Channel Characterization and System-Level Modeling for Multiband OFDM Ultra-Wideband Body-Centric Wireless Network," *IEEE Transactions on Microwave Theory and Techniques*, vol. 58, no. 12, pp. 3485–3492, Dec. 2010.
- [105] R. Chávez-Santiago, C. Garcia-Pardo, A. Fornes-Leal, A. Vallés-Lluch, G. Vermeeren, W. Joseph, I. Balasingham, and N. Cardona, "Experimental Path Loss Models for In-Body Communications Within 2.36-2.5 GHz," *IEEE Journal of Biomedical and Health Informatics*, vol. 19, no. 3, pp. 930–937, May 2015.
- [106] P. A. Floor, R. Chávez-Santiago, S. Brovoll, Ø. Aardal, J. Bergsland, O. J. H. N. Grymyr, P. S. Halvorsen, R. Palomar, D. Plettemeier, S. E. Hamran, T. A. Ramstad, and I. Balasingham, "In-Body to On-Body Ultrawideband Propagation Model Derived From Measurements in Living Animals," *IEEE Journal of Biomedical and Health Informatics*, vol. 19, no. 3, pp. 938–948, May 2015.
- [107] D. Anzai, K. Katsu, R. Chavez-Santiago, Q. Wang, D. Plettemeier, J. Wang, and I. Balasingham, "Experimental Evaluation of Implant UWB-IR Transmission With Living Animal for Body Area Networks," *IEEE Transactions on Microwave Theory and Techniques*, vol. 62, no. 1, pp. 183–192, Jan. 2014.

- [108] D. Kurup, W. Joseph, G. Vermeeren, and L. Martens, "In-body Path Loss Model for Homogeneous Human Tissues," *IEEE Transactions on Electromagnetic Compatibility*, vol. 54, no. 3, pp. 556–564, Jun. 2012.
- [109] A. F. Demir, H. Arslan, and I. Uysal, "Bio-inspired filter banks for SSVEP-based brain-computer interfaces," in *2016 IEEE-EMBS International Conference on Biomedical and Health Informatics (BHI)*, Feb. 2016, pp. 144–147.
- [110] H. Cao, V. Leung, C. Chow, and H. Chan, "Enabling technologies for wireless body area networks: A survey and outlook," *IEEE Communications Magazine*, vol. 47, no. 12, pp. 84–93, Dec. 2009.
- [111] D. B. Smith, D. Miniutti, T. A. Lamahewa, and L. W. Hanlen, "Propagation Models for Body-Area Networks: A Survey and New Outlook," *IEEE Antennas and Propagation Magazine*, vol. 55, no. 5, pp. 97–117, Oct. 2013.
- [112] "IEEE Standard for Local and metropolitan area networks - Part 15.6: Wireless Body Area Networks," *IEEE Std 802.15.6-2012*, pp. 1–271, Feb. 2012.
- [113] K. Sayrafian-Pour, W.-B. Yang, J. Hagedorn, J. Terrill, K. Y. Yazdandoost, and K. Hamaguchi, "Channel Models for Medical Implant Communication," *International Journal of Wireless Information Networks*, vol. 17, no. 3-4, pp. 105–112, Dec. 2010.
- [114] A. Khaleghi, R. Chavez-Santiago, and I. Balasingham, "Ultra-wideband statistical propagation channel model for implant sensors in the human chest," *Antennas Propagation IET Microwaves*, vol. 5, no. 15, pp. 1805–1812, Dec. 2011.
- [115] "ANSYS HFSS - High Frequency Electromagnetic Field Simulation." [Online]. Available: <http://www.ansys.com/Products/Electronics/ANSYS-HFSS>
- [116] T. S. Rappaport, *Wireless communications: principles and practice*. Prentice Hall PTR New Jersey, 1996, vol. 2.

- [117] M. A. Stuchly, A. Kraszewski, S. S. Stuchly, and A. M. Smith, “Dielectric properties of animal tissues in vivo at radio and microwave frequencies: comparison between species,” *Physics in Medicine and Biology*, vol. 27, no. 7, p. 927, 1982.
- [118] S. Gabriel, R. W. Lau, and C. Gabriel, “The dielectric properties of biological tissues: II. Measurements in the frequency range 10 Hz to 20 GHz,” *Physics in Medicine and Biology*, vol. 41, no. 11, p. 2251, 1996.
- [119] A. Rahman and Y. Hao, “A novel tapered slot CPW-fed antenna for ultra-wideband applications and its on/off-body performance,” in *2007 International workshop on Antenna Technology: Small and Smart Antennas Metamaterials and Applications*, Mar. 2007, pp. 503–506.
- [120] K. Y. Yazdandoost and K. Sayrafian-Pour, “Channel model for body area network (BAN),” Tech. Rep. IEEE P802, vol. 15, 2009.
- [121] W. C. Y. Lee, *Mobile Cellular Telecommunications Systems*, 1st ed. New York: McGraw-Hill Inc., US, Nov. 1988.
- [122] G. R. Müller-Putz, R. Scherer, C. Brauneis, and G. Pfurtscheller, “Steady-state visual evoked potential (SSVEP)-based communication: impact of harmonic frequency components,” *Journal of Neural Engineering*, vol. 2, no. 4, p. 123, 2005.
- [123] A. Birca, L. Carmant, A. Lortie, and M. Lassonde, “Interaction between the flash evoked SSVEPs and the spontaneous EEG activity in children and adults,” *Clinical Neurophysiology*, vol. 117, no. 2, pp. 279–288, Feb. 2006.
- [124] “AVI SSVEP Dataset.” [Online]. Available: www.setzner.com
- [125] A. V. Oppenheim and R. W. Schaffer, *Discrete-Time Signal Processing*, 3rd ed. Upper Saddle River: Pearson, Aug. 2009.


- [126] A. Ng, “CS229: Machine Learning Lecture Notes.” [Online]. Available: <http://cs229.stanford.edu/>
- [127] O. Irsoy, O. T. Yildiz, and E. Alpaydin, “Design and analysis of classifier learning experiments in bioinformatics: Survey and case studies,” vol. 9, no. 6, pp. 1663–1675, Nov 2012.
- [128] H. Hotelling, “Relations Between Two Sets of Variates,” *Biometrika*, vol. 28, no. 3/4, pp. 321–377, 1936.
- [129] O. Friman, J. Cedefamn, P. Lundberg, M. Borga, and H. Knutsson, “Detection of neural activity in functional MRI using canonical correlation analysis,” *Magnetic Resonance in Medicine*, vol. 45, no. 2, pp. 323–330, Feb. 2001.
- [130] M. H. DeGroot and M. J. Schervish, *Probability and Statistics*, 4th ed. Pearson Education, Jan. 2012.
- [131] R. A. Armstrong, “When to use the bonferroni correction,” *Ophthalmic and Physiological Optics*, vol. 34, no. 5, pp. 502–508, 2014.
- [132] F. Lotte, M. Congedo, A. Lécuyer, F. Lamarche, and B. Arnaldi, “A review of classification algorithms for EEG-based brain–computer interfaces,” *Journal of Neural Engineering*, vol. 4, no. 2, p. R1, 2007.
- [133] S. N. Carvalho, T. B. S. Costa, L. F. S. Uribe, D. C. Soriano, G. F. G. Yared, L. C. Coradine, and R. Attux, “Comparative analysis of strategies for feature extraction and classification in SSVEP BCIs,” *Biomedical Signal Processing and Control*, vol. 21, no. Supplement C, pp. 34–42, Aug. 2015.
- [134] V. P. Oikonomou, G. Liaros, K. Georgiadis, E. Chatzilari, K. Adam, S. Nikolopoulos, and I. Kompatsiaris, “Comparative evaluation of state-of-the-art algorithms for SSVEP-based BCIs,” *arXiv:1602.00904 [cs, stat]*, Feb. 2016.

- [135] P. F. Diez, V. A. Mut, E. M. Avila Perona, and E. Lacia Leber, "Asynchronous BCI control using high-frequency SSVEP," *Journal of NeuroEngineering and Rehabilitation*, vol. 8, p. 39, Jul. 2011.
- [136] F. Teng, "An SSSVEP Brain-computer Interface: A Machine Learning Approach," Ph.D. dissertation, University of Mississippi, University, MS, USA, 2012.

Appendix A: Copyright Permissions

3/6/2020 Rightslink® by Copyright Clearance Center

Copyright Clearance Center RightsLink® Home ? Email Support Sign in Create Account



In Vivo Communications: Steps Toward the Next Generation of Implantable Devices
Author: Ali Fatih Demir
Publication: IEEE Vehicular Technology Magazine
Publisher: IEEE
Date: June 2016
Copyright © 2016, IEEE

Thesis / Dissertation Reuse

The IEEE does not require individuals working on a thesis to obtain a formal reuse license, however, you may print out this statement to be used as a permission grant:

Requirements to be followed when using any portion (e.g., figure, graph, table, or textual material) of an IEEE copyrighted paper in a thesis:

- 1) In the case of textual material (e.g., using short quotes or referring to the work within these papers) users must give full credit to the original source (author, paper, publication) followed by the IEEE copyright line © 2011 IEEE.
- 2) In the case of illustrations or tabular material, we require that the copyright line © [Year of original publication] IEEE appear prominently with each reprinted figure and/or table.
- 3) If a substantial portion of the original paper is to be used, and if you are not the senior author, also obtain the senior author's approval.

Requirements to be followed when using an entire IEEE copyrighted paper in a thesis:

- 1) The following IEEE copyright/ credit notice should be placed prominently in the references: © [year of original publication] IEEE. Reprinted, with permission, from [author names, paper title, IEEE publication title, and month/year of publication]
- 2) Only the accepted version of an IEEE copyrighted paper can be used when posting the paper or your thesis online.
- 3) In placing the thesis on the author's university website, please display the following message in a prominent place on the website: In reference to IEEE copyrighted material which is used with permission in this thesis, the IEEE does not endorse any of [university/educational entity's name goes here]'s products or services. Internal or personal use of this material is permitted. If interested in reprinting/republishing IEEE copyrighted material for advertising or promotional purposes or for creating new collective works for resale or redistribution, please go to http://www.ieee.org/publications_standards/publications/rights/rights_link.html to learn how to obtain a License from RightsLink.

If applicable, University Microfilms and/or ProQuest Library, or the Archives of Canada may supply single copies of the dissertation.

BACK CLOSE

© 2020 Copyright - All Rights Reserved | Copyright Clearance Center, Inc. | Privacy statement | Terms and Conditions
Comments? We would like to hear from you. E-mail us at customer-care@copyright.com

<https://s100.copyright.com/AppDispatchServlet#formTop> 1/1

The permission above is for the use of materials in Chapter 1.

JOHN WILEY AND SONS LICENSE
TERMS AND CONDITIONS

Apr 01, 2020

This Agreement between Mr. Ali Demir ("You") and John Wiley and Sons ("John Wiley and Sons") consists of your license details and the terms and conditions provided by John Wiley and Sons and Copyright Clearance Center.

License Number 4800550265265

License date Apr 01, 2020

Licensed
Content
Publisher John Wiley and SonsLicensed
Content
Publication Wiley BooksLicensed
Content Title Waveform Design for 5G and BeyondLicensed
Content Author Huseyin Arslan, Mostafa Ibrahim, Mohamed Elkourdi, et alLicensed
Content Date Sep 14, 2018Licensed
Content Pages 26

Type of use Dissertation/Thesis

Requestor type University/Academic

The permission above is for the use of materials in Chapter 1.

Creative Commons Attribution License (CCBY)

Inter-numerology Interference Management with Adaptive Guards: A Cross-layer Approach
Demir, Ali Fatih; ARSLAN, HUSEYIN
IEEE Access

By clicking the checkbox at the bottom of this page you, as the author or representative of the author, confirm that your work is licensed to IEEE under the Creative Commons Attribution 4.0(CC BY 4.0). As explained by the Creative Commons web site, this license states that IEEE is free to share, copy, distribute and transmit your work under the following conditions:

- Attribution - Users must attribute the work in the manner specified by the author or licensor (but not in any way that suggests that they endorse the users or their use of the work).
- Noncommercial - Users may not use this work for commercial purposes.
- No Derivative Works - Users may not alter, transform, or build upon this work.

With the understanding that:

- **Waiver** - Any of the above conditions can be waived if users get permission from the copyright holder.
- **Public Domain** - Where the work or any of its elements is in the public domain under applicable law, that status is in no way affected by the license.
- **Other Rights** - In no way are any of the following rights affected by the license:
 - A user's fair dealing or fair use rights, or other applicable copyright exceptions and limitations;
 - The author's moral rights;
 - Rights other persons may have either in the work itself or in how the work is used, such as publicity or privacy rights.

For any reuse or distribution, users must make clear to others the license terms of this work.

Upon clicking on the checkbox below, you will not only confirm that your submission is under the CCBY license but you will also be taken to IEEE's Terms of Use, which will require your signature.

I confirm the submitted work is licensed to IEEE under the Creative Commons Attribution 4.0 United States (CC BY 4.0)

TERMS AND CONDITIONS OF AN AUTHOR'S USE OF THE CREATIVE COMMONS ATTRIBUTION LICENSE (CCBY)

1. Creative Commons Licensing

To grow the commons of free knowledge and free culture, all users are required to grant broad permissions to the general public to re-distribute and re-use their contributions freely. Therefore, for any text, figures, or other work in any medium you hold the copyright to, by submitting it, you agree to license it under the Creative Commons Attribution 4.0 Unported License.

2. Attribution

As an author, you agree to be attributed in any of the following fashions: a) through a hyperlink (where possible) or URL to the article or articles you contributed to, b) through a hyperlink (where possible) or URL to an alternative, stable online copy which is freely accessible, which conforms with the license, and which provides credit to the authors in a manner equivalent to the credit given on this website, or c) through a list of all authors.

3. Terms of Publication

The permission above is for the use of materials in Chapter 1 and Chapter 2.



RightsLink®



Home



Help



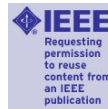
Email Support



Sign in



Create Account



Anatomical Region-Specific In Vivo Wireless Communication Channel Characterization

Author: Ali Fatih Demir

Publication: Biomedical and Health Informatics, IEEE Journal of

Publisher: IEEE

Date: Sept. 2017

Copyright © 2017, IEEE

Thesis / Dissertation Reuse

The IEEE does not require individuals working on a thesis to obtain a formal reuse license, however, you may print out this statement to be used as a permission grant:

Requirements to be followed when using any portion (e.g., figure, graph, table, or textual material) of an IEEE copyrighted paper in a thesis:

- 1) In the case of textual material (e.g., using short quotes or referring to the work within these papers) users must give full credit to the original source (author, paper, publication) followed by the IEEE copyright line © 2011 IEEE.
- 2) In the case of illustrations or tabular material, we require that the copyright line © [Year of original publication] IEEE appear prominently with each reprinted figure and/or table.
- 3) If a substantial portion of the original paper is to be used, and if you are not the senior author, also obtain the senior author's approval.

Requirements to be followed when using an entire IEEE copyrighted paper in a thesis:

- 1) The following IEEE copyright/ credit notice should be placed prominently in the references: © [year of original publication] IEEE. Reprinted, with permission, from [author names, paper title, IEEE publication title, and month/year of publication]
- 2) Only the accepted version of an IEEE copyrighted paper can be used when posting the paper or your thesis on-line.
- 3) In placing the thesis on the author's university website, please display the following message in a prominent place on the website: In reference to IEEE copyrighted material which is used with permission in this thesis, the IEEE does not endorse any of [university/educational entity's name goes here]'s products or services. Internal or personal use of this material is permitted. If interested in reprinting/republishing IEEE copyrighted material for advertising or promotional purposes or for creating new collective works for resale or redistribution, please go to http://www.ieee.org/publications_standards/publications/rights/rights_link.html to learn how to obtain a License from RightsLink.

If applicable, University Microfilms and/or ProQuest Library, or the Archives of Canada may supply single copies of the dissertation.

BACK

CLOSE

The permission above is for the use of materials in Chapter 1 and Chapter 3.

Creative Commons Attribution License (CCBY)

Bio-inspired Filter Banks for Frequency Recognition of SSVEP-based Brain-computer Interfaces
Demir, Ali Fatih; ARSLAN, HUSEYIN; Uysal, Ismail
IEEE Access

By clicking the checkbox at the bottom of this page you, as the author or representative of the author, confirm that your work is licensed to IEEE under the Creative Commons Attribution 4.0(CC BY 4.0). As explained by the Creative Commons web site, this license states that IEEE is free to share, copy, distribute and transmit your work under the following conditions:

- Attribution - Users must attribute the work in the manner specified by the author or licensor (but not in any way that suggests that they endorse the users or their use of the work).
- Noncommercial - Users may not use this work for commercial purposes.
- No Derivative Works - Users may not alter, transform, or build upon this work.

With the understanding that:

- **Waiver** - Any of the above conditions can be waived if users get permission from the copyright holder.
- **Public Domain** - Where the work or any of its elements is in the public domain under applicable law, that status is in no way affected by the license.
- **Other Rights** - In no way are any of the following rights affected by the license:
 - A user's fair dealing or fair use rights, or other applicable copyright exceptions and limitations;
 - The author's moral rights;
 - Rights other persons may have either in the work itself or in how the work is used, such as publicity or privacy rights.

For any reuse or distribution, users must make clear to others the license terms of this work.

Upon clicking on the checkbox below, you will not only confirm that your submission is under the CCBY license but you will also be taken to IEEE's Terms of Use, which will require your signature.

I confirm the submitted work is licensed to IEEE under the Creative Commons Attribution 4.0 United States (CC BY 4.0)

TERMS AND CONDITIONS OF AN AUTHOR'S USE OF THE CREATIVE COMMONS ATTRIBUTION LICENSE (CCBY)

1. Creative Commons Licensing

To grow the commons of free knowledge and free culture, all users are required to grant broad permissions to the general public to re-distribute and re-use their contributions freely. Therefore, for any text, figures, or other work in any medium you hold the copyright to, by submitting it, you agree to license it under the Creative Commons Attribution 4.0 Unported License.

2. Attribution

As an author, you agree to be attributed in any of the following fashions: a) through a hyperlink (where possible) or URL to the article or articles you contributed to, b) through a hyperlink (where possible) or URL to an alternative, stable online copy which is freely accessible, which conforms with the license, and which provides credit to the authors in a manner equivalent to the credit given on this website, or c) through a list of all authors.

3. Terms of Publication

The permission above is for the use of materials in Chapter 1 and Chapter 4.

About the Author

Ali Fatih Demir received the B.S. degree in electrical engineering from Yıldız Technical University, Istanbul, Turkey, in 2011 and the M.S. degrees in electrical engineering and applied statistics from Syracuse University, Syracuse, NY, USA in 2013. He is currently pursuing the Ph.D. degree as a member of the Wireless Communication and Signal Processing (WCSP) Group in the Department of Electrical Engineering, University of South Florida, Tampa, FL, USA. His current research interests include PHY and MAC aspects of wireless communication systems, wireless body area networks (WBANs), and signal processing/machine learning algorithms for brain-computer interfaces (BCIs). He is a member of IEEE and National Academy of Inventors.